

Ilkka Pohjalainen

**Experimental gas jet studies for the IGISOL LIST
method and simulation modeling**

Master's Thesis
in Physical Sciences (Experimental
Nuclear Physics)
December 17, 2010



UNIVERSITY OF JYVÄSKYLÄ
DEPARTMENT OF PHYSICS

Jyväskylä

Author: Ilkka Pohjalainen

Contact information: Ilkka.Pohjalainen@jyu.fi

Title: Experimental gas jet studies for the IGISOL LIST method and simulation modeling

Työn nimi: Kokeellisia kaasusuihkututkimuksia IGISOL LIST menetelmää koskien ja sen tietokonemallinnus

Project: Master's Thesis in Physical Sciences (Experimental Nuclear Physics)

Page count: 107

Abstract: The IGISOL Laser Ion Source Trap (LIST) is a method in which a supersonic gas jet is used to transport thermalized nuclear reaction products from a gas cell into a sextupole radio frequency ion guide (SPIG) while removing any non-neutral part of the jet by a positively biased repeller electrode. Specific atom species are resonantly re-ionized with laser radiation in the SPIG which enables the study of exotic nuclei without isobaric contamination. In the first part of this work the repelling effect is studied through a series of ion optical Monte-Carlo simulations. The simulations were able to support the hypothesis that the constant collisions between the fast moving buffer gas atoms and the ions provides additional momentum to overcome potential barriers of several tens of volts, explaining the need for high repelling electrode potentials in practice. The simulations were also used to investigate the differences between helium and argon buffer gases and different repelling geometries. The experimental behaviour of the repelling efficiency as a function of repelling potential was qualitatively reproduced. The second part of this work concentrated on the supersonic gas jet formation and the parameters that affect the gas jet properties, in particular the width. For an efficient transportation of atoms from the gas cell to the SPIG the gas jet needs to be well collimated. The gas jet behaviour was investigated with two nozzle shapes and diameters in varying pressure environments by photographing plasma afterglow in the gas expanding from an arc discharge ion guide. It was found that the jet width is strongly dependent on background pressure and independent of the nozzle shape and gas cell pressure. Because the gas jet exhibited a collimated behaviour only with increasing background pressure, a new de Laval type of nozzle was introduced. This nozzle produced a narrow collimated jet structure at background pressures as low as 0.33 mbar.

Suomenkielinen tiivistelmä: IGISOL laserionilähdeloukku (LIST) on menetelmä, jossa supersoonisen kaasusuihkun avulla termalisoidut ydinreaktiotuotteet siirretään radiotaajuiseen sekstupoli-ioniohjaimeen (SPIG), kun samanaikaisesti kaasusuihkun neutralisoitumaton osuus poistetaan positiivisesti biasoidulla suodatuselektrodilla. Vain tietty atomilaji ionisoidaan resonantisti uudelleen lasereilla SPIG:in sisällä. Tämä mahdollistaa eksoottisten ytimien tutkimuksen ilman isobaarista kontaminaatiota. Ensimmäisessä osassa tätä työtä tutkitaan suodatuselektrodin toimintaa ionioptisilla Monte-Carlo-tietokonesimulaatiolla. Simulaatiot antoivat tukea hypoteesille, jonka mukaan jatkuvat törmäykset taustakaasun atomien ja ionien välillä antavat ioneille energiaa ylittää kymmenienkin volttien suodatuselektrodin jännitteet, mikä selittää tarvetta korkeille suodatuselektrodijännitteille käytännössä. Simulaatioilla tutkittiin myös helium- ja argontaustakaasujen eroja ja erilaisia suodatusgeometrioita. Simulaatioilla pystyttiin kvalitatiivisesti jäljittelemään kokeellisesti havaittua suodatustehokkuutta suodatusjännitteen funktiona. Toisessa osassa tätä työtä keskityttiin kaasusuihkun muodostukseen ja muuttujiin, jotka vaikuttavat kaasusuihkun ominaisuuksiin, erityisesti leveyteen. Kaasusuihkun leveys vaikuttaa atomien tehokkuuteen siirtyä SPIG:in sisälle. Kahta suutinmuotoa ja kokoa tutkittiin erilaisissa paineympäristöissä kuvaamalla kipinälähteen jälkihohdetta kaasussa. Analyysissä havaittiin, että kaasusuihkun leveys riippuu vahvasti taustakaasun paineesta ja on riippumaton suuttimen muodosta sekä tulopaineesta. Koska kaasusuihkun havaittiin kapenevan vain taustapainetta nostettaessa, uusi de Laval -tyyppinen suutin esiteltiin lopuksi. Tällä suuttimella muodostettu kaasusuihku osoitti kapeaa ja kollimoitunutta käyttäytymistä niinkin alhaisilla taustakaasun paineen arvoilla kuin 0,33 mbar.

Acknowledgements

This work was carried out at the University of Jyväskylä, Department of Physics (JYFL) during the years 2009-2010. I would like to express my deepest gratitude to my supervisor Iain Moore whose encouragement, patience, advice and critique have been indispensable and without whom this work would not have been possible. I would like to also thank all co-workers and those who have made possible for me to work within IGISOL group. Lastly, I want to say warm thanks to my friends, family, and loved ones who have been supporting me during this work.

Jyväskylä, December 2010

Ilkka Pohjalainen

Contents

List of Figures	iii
Nomenclature	vi
Abbrev.	vii
1 Introduction	1
1.1 IGISOL facility	1
1.1.1 IGISOL technique	1
1.1.2 IGISOL laser ion source	2
1.2 JYFL LIST technique	5
1.2.1 Bismuth off-line test	8
1.3 Sextupole radio frequency ion guide	10
2 Simulation studies of the repeller electrode	12
2.1 Simion simulation environment and simulation models.	12
2.1.1 Simion simulation software and the simulated repeller electrode system	12
2.1.2 Gas models	14
2.2 Simulation results	16
2.2.1 Simulation of the repeller electrode	16
2.2.2 Influence of the simulation environment	19
2.2.3 Transverse ion collector	20

CONTENTS

3	Studies for optimization of the LIST method	24
3.1	Motivation	24
3.2	Supersonic gas flow	25
3.2.1	Area-velocity and Area-Mach number relations	25
3.2.2	The Gas flow regimes for a converging-diverging nozzle	28
3.2.3	The formation of an underexpanded free jet	31
3.2.4	Mach disc position	32
3.3	Experiments for gas jet studies	33
3.3.1	Exit nozzle shapes	33
3.3.2	Experimental setup for gas jet photography	34
3.3.3	Gas cell and background pressures	35
3.3.4	Gas jet fluorescence	37
3.3.5	Gas jet analysis procedure	37
3.4	Discussion	42
3.4.1	Gas jet characteristics	42
3.4.2	The FWHM vs. the background pressure	45
3.4.3	De Laval nozzle	48
3.5	The Background pressure determination by the Mach disc position	51
3.5.1	The background pressure determined by the Mach disc location	51
4	Concluding remarks and outlook	54
	References	56
	Appendices	

List of Figures

1.1	An experimental setup of the IGISOL method using the ion guide for fission products.	2
1.2	Schematic of the FURIOS laser ion source.	4
1.3	The experimental setup of the LIST method.	5
1.4	A photograph of the SPIG with the repelling electrode.	7
1.5	The number of ions transmitted into the SPIG as a function of the repelling voltage.	8
1.6	The number of bismuth photo-ions created inside the gas cell vs. the SPIG as a function of resonance step wavelength.	9
2.1	The simulated repeller electrode system.	13
2.2	The electric field lines of the repelling electrode system with distances of 1cm and 1mm between the ion source and repelling electrode. . .	14
2.3	The pressure trend at the exit hole and SPIG region.	15
2.4	Simulation vs. experimental data of the ion count rate as a function of the repelling voltage with a 1 cm gap (a) and 1 mm gap (b) between the ion source and the repeller electrode.	17
2.5	Comparison of simulation conditions.	20
2.6	A cross sectional 3D model of the simulated repeller electrode system with deflection plates.	21
2.7	Electric field lines of the ion collector at the front of the repelling electrode.	21
2.8	Simulation results of the transverse ion collector.	22

LIST OF FIGURES

3.1	Schematics of the flow regimes of the converging-diverging nozzle, and related (x,P) plot.	28
3.2	The structure of an underexpanded free jet at two pressure ratios. . .	31
3.3	Schematic drawings of the exit hole and converging-diverging nozzle	33
3.4	Schematic illustration of the experimental setup for gas jet photography.	34
3.5	An example of a photograph of a jet formed with the converging-diverging nozzle.	36
3.6	A gray-scale gas jet photograph with the slice position	38
3.7	Gas jet intensities in exponential and linear formats for the 1.45 mm exit hole in 56 mbar and 25 mbar, as well as for the 0.7 mm exit hole in 56 mbar of gas cell pressure. The background pressure of each curve is labelled in the boxes.	40
3.8	Gas jet intensities in exponential and linear formats for the 0.7 mm exit hole in 27 mbar, as well as the for the 1.45 mm converging-diverging nozzle in 56 mbar and 24 mbar of gas cell pressure. The background pressure of each curve is labelled in the boxes.	41
3.9	False colour photographs of the jets with the 1.45 mm exit hole and 1.45 mm converging-diverging nozzle with 56 mbar of inlet pressure	44
3.10	The number of Gaussian and Lorentzian-like intensity profiles as a function of background pressure.	45
3.11	Gas jet FWHM as a function of extraction chamber background pressure for different gas cell pressures and nozzles.	46
3.12	Gas jet intensity as a function of extraction chamber background pressure for different gas cell pressures and nozzles.	46
3.13	Contour maps of gas jet photographs taken at two background pressures, 0.2 mbar and 5.6mbar.	48
3.14	The de Laval nozzle design.	49

LIST OF FIGURES

3.15 The gas jet formed by the de Laval nozzle.	49
3.16 Intensity curves and FWHM of the jet as a function of distance for the de Laval nozzle	50
3.17 A photograph of the fluorescence of a strongly underexpanded argon jet	51
3.18 A photograph of an underexpanded argon jet when the inlet pressure was 50mbar	51
3.19 Comparison of the directly measured extraction chamber background pressure and the background pressure deduced from the Mach disc position as a function of gas cell pressure.	52

Nomenclature

γ	The ratio of specific heats
ρ	The gas density
A	The area of a duct
a	Speed of sound
A_{min}	The area of the narrowest part of a duct
d	The throat diameter of a nozzle
h	Enthalpy
M	The Mach number: u/a
m	Mass
P	Pressure
P_{ex}	The pressure at the nozzle exit
P_{in}	The pressure of the reservoir, the inlet pressure
$P_{Machdisc}$	The background pressure measured by Mach disc location
P_{pg}	The background pressure of an expansion chamber
u	The gas velocity
x_M	The location of a Mach disc

Abbrv.

FURIOS Fast Universal Resonance laser Ion Source

FWHM Full Width at Half Maximum

IGISOL Ion Guide Isotope Separator On-Line

JYFL Jyväskylän Yliopiston Fysiikan Laitos

LISOL Leuven Isotope Separator On-Line

LIST Laser Ion Source Trap

Nd:YAG Neodymium-doped Yttrium Aluminium Garnet

SPIG Sextupole Ion Guide

RF Radio Frequency

1 Introduction

1.1 IGISOL facility

1.1.1 IGISOL technique

Almost three decades ago an ion transportation technique was developed at the IGISOL (Ion Guide Isotope Separator On-Line) radioactive ion beam facility in JYFL. The so-called ion guide technique uses an inert buffer gas as a mean of transportation and as a stopper medium for high energy nuclear reaction products. The IGISOL facility has been used to study short-lived exotic isotopes far from the line of beta-stability. Refractory elements are of particular interest for this method due to the chemical non-selectivity of the ion guide. In addition a fast extraction time allows the study of isotopes with half-lives under 1ms. The technique has led to new discoveries of neutron-rich isotopes and their properties, and it has been applied to decay spectroscopy of both proton-rich and neutron-rich nuclei [1,2].

In the ion guide method a projectile beam from an accelerator hits a thin target in a gas cell. In the target nuclear reactions create isotopes that recoil out in highly charged states into the chamber filled with buffer gas, which is usually helium at pressures of a few hundred mbar. The buffer gas is used to slow down and thermalize the reaction products and the fast flow of the gas extracts them out of the cell through a nozzle into the next chamber. Most of the produced ions end up in a 1^+ charge state via a series of charge exchange processes with the buffer gas atoms and impurities in the gas [3].

As the ions exit the gas cell they are separated from the neutral buffer gas and are

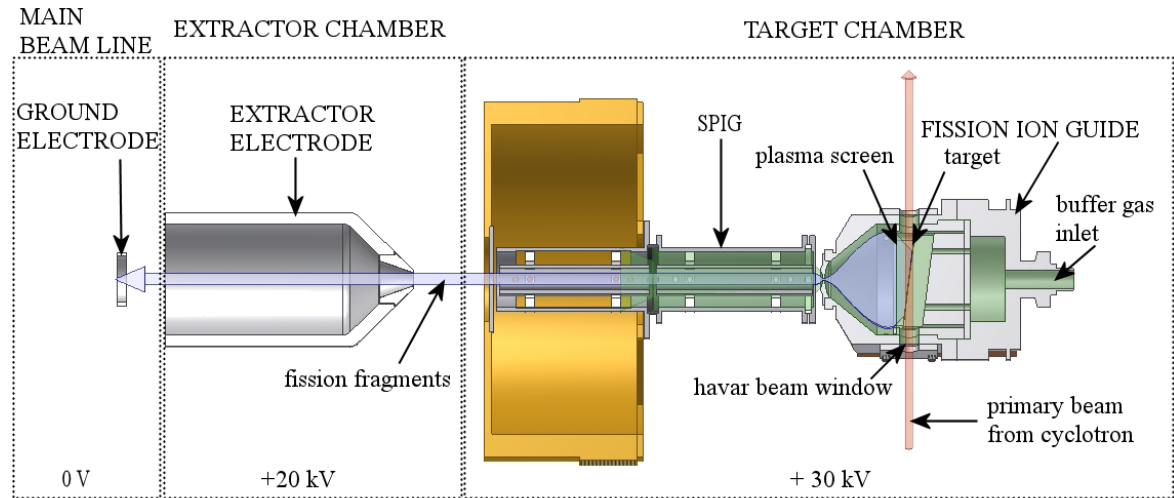


Figure 1.1: An experimental setup of the IGISOL method using the ion guide for fission products.

further accelerated towards a mass separator while differential pumping is used to pump away the neutral fraction. Figure 1.1 shows an example of the ion guide that is used for fission product transportation and the surrounding experimental setup.

When the gas exits the nozzle of the gas cell the pressure drops dramatically by about two orders of magnitude and the gas starts to expand strongly. At the same time the gas flow becomes supersonic. As a result a gas jet is formed, which in the present day system is directed to a sextupole radio-frequency ion guide (SPiG), that was preceded by the traditional skimmer system. The SPiG uses high frequency rf-voltage applied to six encircling rods to form an ion transporting pseudopotential [1].

1.1.2 IGISOL laser ion source

The two main deficiencies of the IGISOL technique lie in its low efficiency for certain reactions and high isobaric impurities, which are particularly problematic when isotopes far away from the beta stability line are of interest, as the mass-separated

beam can contain other, more stable elements with considerably higher fluxes. The efficiency of the extraction is impaired by the ionization of the buffer gas that introduces plasma effects which lead to neutralization of the ions. In addition, distortions of the electric field in the extractor region or other losses during the transportation of the ions can adversely affect the efficiency [1].

Resonant ionization laser ion sources are a reliable and efficient on-line ion source for radioactive ion beams, because of their high versatility for production of different elements and high selectivity and purity of the ion beam generated by resonant laser radiation. Laser ion sources can enable experiments on the most exotic isotopes that would otherwise be impossible due to the overwhelming isobaric contamination. The development of new powerful tunable laser systems, e.g. titanium:sapphire lasers, has initiated a significant evolution within the field of laser ion sources [4].

To overcome the aforementioned deficiencies in the IGISOL technique, the laser ion source FURIOS (Fast Universal Resonance laser Ion Source) [5] has been developed along similar lines to that of the LISOL group at the University of Leuven [6] and to TRILIS in TRIUMF [7], both using laser resonance ionization. The selectivity of the ion guide technique is improved by the Z-selective laser ionization process in which a neutral atom is ionized by step-wise excitation. To produce the excitations the neutral atoms are exposed simultaneously to two or more high intensity laser pulses. The first pulses saturate the transitions below the ionization potential and the final laser pulse is used to ionize the atom either by a non-resonant transition using a high power pump laser or by exciting the atom into an auto-ionizing state.

The FURIOS facility consists of a twin laser setup using high-resolution titanium:sapphire lasers and dye lasers with Nd:YAG and copper vapour pumping lasers, respectively. The use of both laser systems coupled with second, third, and fourth harmonic generation make it possible to produce laser radiation at wave-

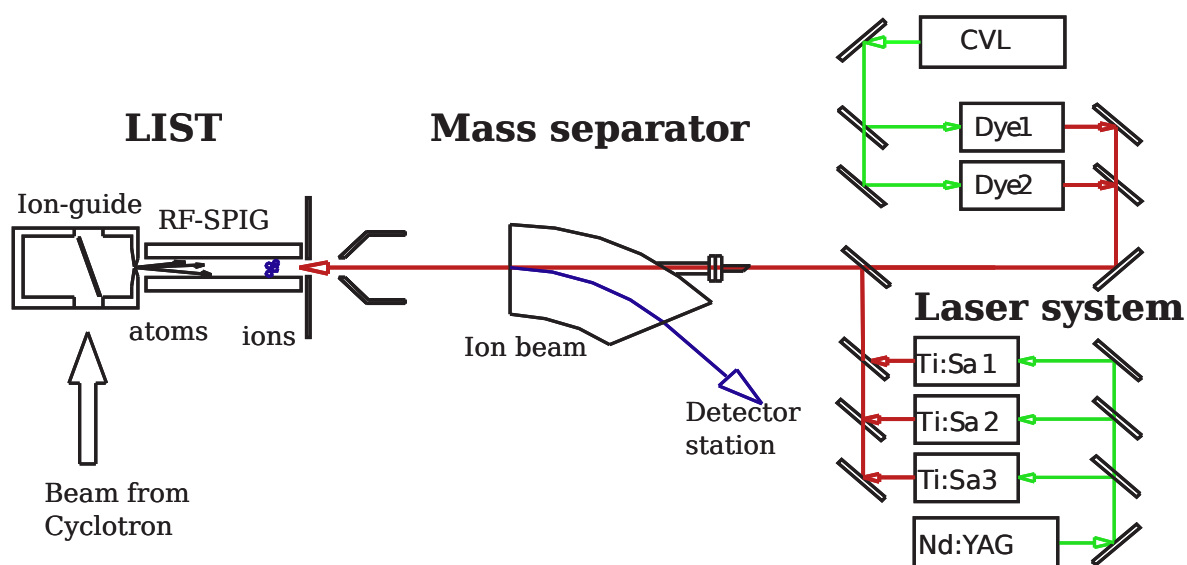


Figure 1.2: Schematic of the FURIOS laser ion source.

lengths ranging from infrared to ultraviolet thus providing a universal coverage of ionization schemes throughout the periodic table. The laser system can also provide high enough powers to sufficiently saturate atomic transitions in large volumes of atom loaded buffer gas. The high laser powers became possible with the development of double-sided pumping of the titanium:sapphire lasers [8]. The laser system is operated at a high repetition rate of about 10 kHz. Such a rate is needed so that each atom is at least once exposed to the laser pulses when flowing with the fast buffer gas. A schematic view of the FURIOS laser ion source operating with the fission ion guide is shown in Figure 1.2 [5].

There are two different types of laser ionization geometries at the IGISOL. In the first method, which is similar to the LISOL facility in Louvain la Neuve [9], laser radiation is delivered to the gas cell through a window in the rear or side of the cell, and the laser ionization is performed inside the gas cell. Created photo ions are exposed to the plasma effects inside the gas cell affecting the efficiency of the ion guide.

In the second method, any non-neutral part of the gas jet entering the SPIG is

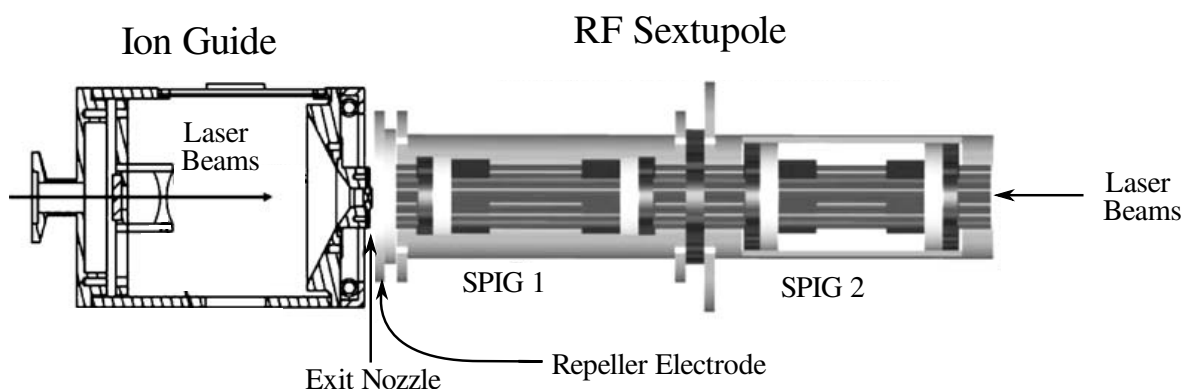


Figure 1.3: The experimental setup of the LIST method.

repelled with a repeller electrode. The lasers are used to re-ionize atoms within the sextupole guide in a counter-propagating geometry. This is the so-called Laser Ion Source Trap (LIST) method [10,11], which is described in more detail in the next section. In this work LIST conditions are studied by investigating the gas jet behaviour with different nozzle types and pressure conditions, as well as via simulation studies of the repelling behaviour of the repeller electrode.

1.2 JYFL LIST technique

The LIST method was originally proposed to suppress surface ion contamination from a hot cavity laser ion source [10], and was eventually coupled to a gas catcher system at the Leuven Isotope Separator On-Line (LISOL) [12]. The JYFL LIST [13] method is done similarly by stopping and thermalizing the reaction products in the ion guide gas cell. A repeller electrode is used to let only the neutral atoms into the SPIG wherein the reaction products of interest are captured by the rf potential after being selectively re-ionized with counter-propagating laser pulses. This ensures high beam purity because any ion transported for subsequent experiments is guaranteed to be photo-ion ionized resonantly by the lasers.

Figure 1.3 shows the experimental setup of the LIST method. Ions and atoms are transported by a buffer gas out of the ion guide through a nozzle towards the SPIG. The buffer gas is usually either helium or argon. Argon has favourable characteristics for the LIST method including a lower ionization potential leading to more effective neutralization of the reaction products than helium. A gap of about 0.5 cm is usually kept between the ion guide and the SPIG repeller electrode. The gap size is adjustable. The lasers can be directed into the ion guide-SPIG system via two routes, either through the ion guide or through the mass separator dipole magnet. This enables the ionization of the atoms both inside the gas cell and the SPIG.

The repeller electrode used in the SPIG is a simple 3 mm thick plate with a 6 mm circular aperture, located in front of the SPIG rods. The repeller electrode is isolated from the rest of the SPIG system by an isolating ring seal. This allows a positive DC voltage to be applied to the repeller electrode with respect to the gas cell. Figure 1.4 is a photograph showing the repelling electrode and the ring seal next to the SPIG.

The applied repelling voltage will create a potential barrier for the ions coming out from the ion guide which has to be overcome if they are to enter the SPIG. As the ions are transported by the buffer gas flow alone, the kinetic energy they have relates to the gas velocity. With helium gas velocities of about 1000 m/s the ions have less than 1 eV of kinetic energy translating to 1 V of repelling voltage, but, in practice, the repeller electrode needs several tens of volts in order to repel all of the non-neutral fraction. The high voltages needed for successful repelling is thought to be a consequence of continuous collisions of ions with the buffer gas atoms. The collisions between the gas jet atoms and the ions provide sufficient energy to overcome even large potential barriers.

There has, however, been a report of successful repelling with a remarkably low voltage of about +1 V [14]. This was observed with ^{58}Cu ions produced in a fusion-evaporation reaction. The repelling of ^{58}Cu ions (detected by positrons from β de-

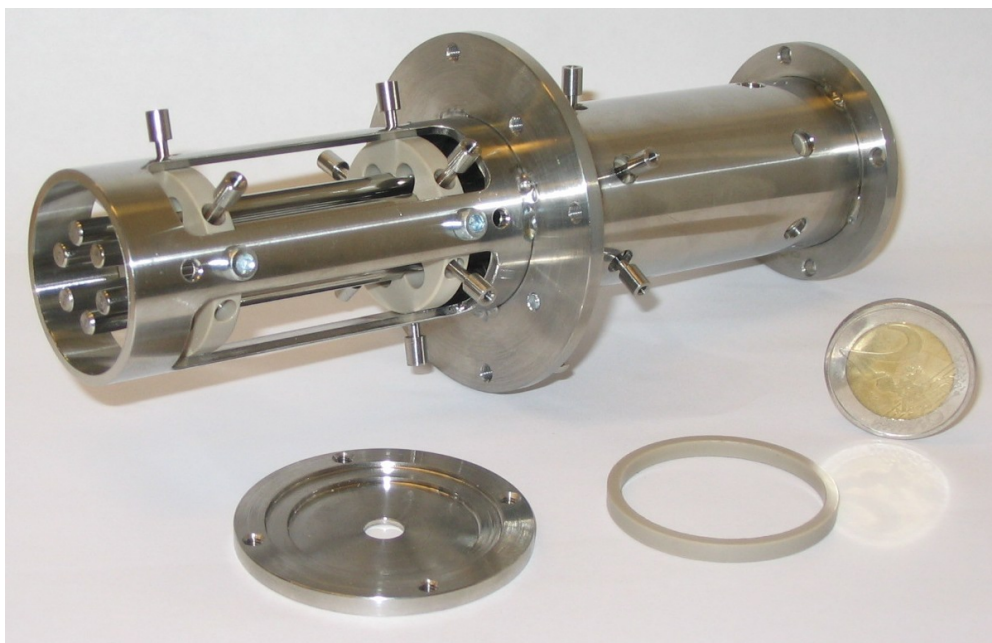


Figure 1.4: A photograph of the SPIG with the repelling electrode plate dismounted. A two euro coin is on the right for scale.

ca) is shown in Figure 1.5 as a blue dashed line, as a function of repelling voltage. The signal shows a sudden and complete suppression of the ions with only slightly positive potential.

Figure 1.5 also shows the more usual repelling behaviour which needs over +100 V for complete suppression of the ions. In this case Ni^+ ions were repelled from a gas cell filled with 50 mbar helium at 1mm distance from the repeller electrode. It should be noted however that these two repelling potential behaviours are not directly comparable because of differences in the experimental setup.

The next chapter discusses simulations which were done to study the repelling phenomenon in more detail.

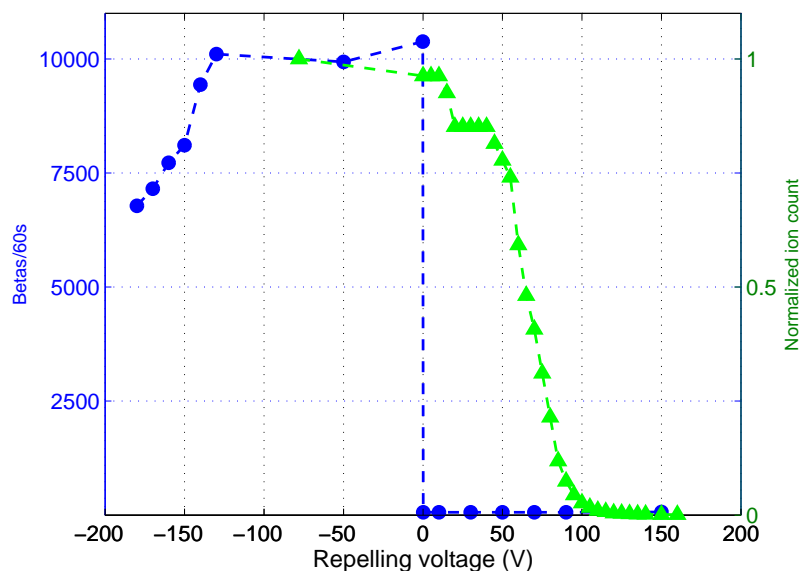


Figure 1.5: The number of ions transmitted into the SPIG as a function of the repelling voltage. The blue line shows a more unusual +1V repelling effect and the green line shows the normally witnessed repelling behavior.

1.2.1 Bismuth off-line test

The first successful off-line test of the LIST method was done with stable ^{209}Bi . The bismuth atoms were produced from a resistively heated filament within a gas cell. The atoms were ionized in a two-step scheme, one resonant step and a final non-resonant step. By adding timing gates to the ion signal, the ions produced inside the SPIG could be counted separately from the ions produced inside the gas cell [15].

In Figure 1.6 four plots are shown, each of which contain spectra of ^{209}Bi ions created inside the SPIG, inside the gas cell and summed to create a total ion spectrum. The ion counts are given as a function of the resonant step laser wavelength with different repelling voltages. In plots A-C the spectra show two peaks produced by the hyperfine states of ^{209}Bi . Also in these spectra the gap between the gas cell and repeller is sealed in order to improve gas transmission to the SPIG.

Plot A shows the spectrum measured with a repelling voltage of -10 V. In this case

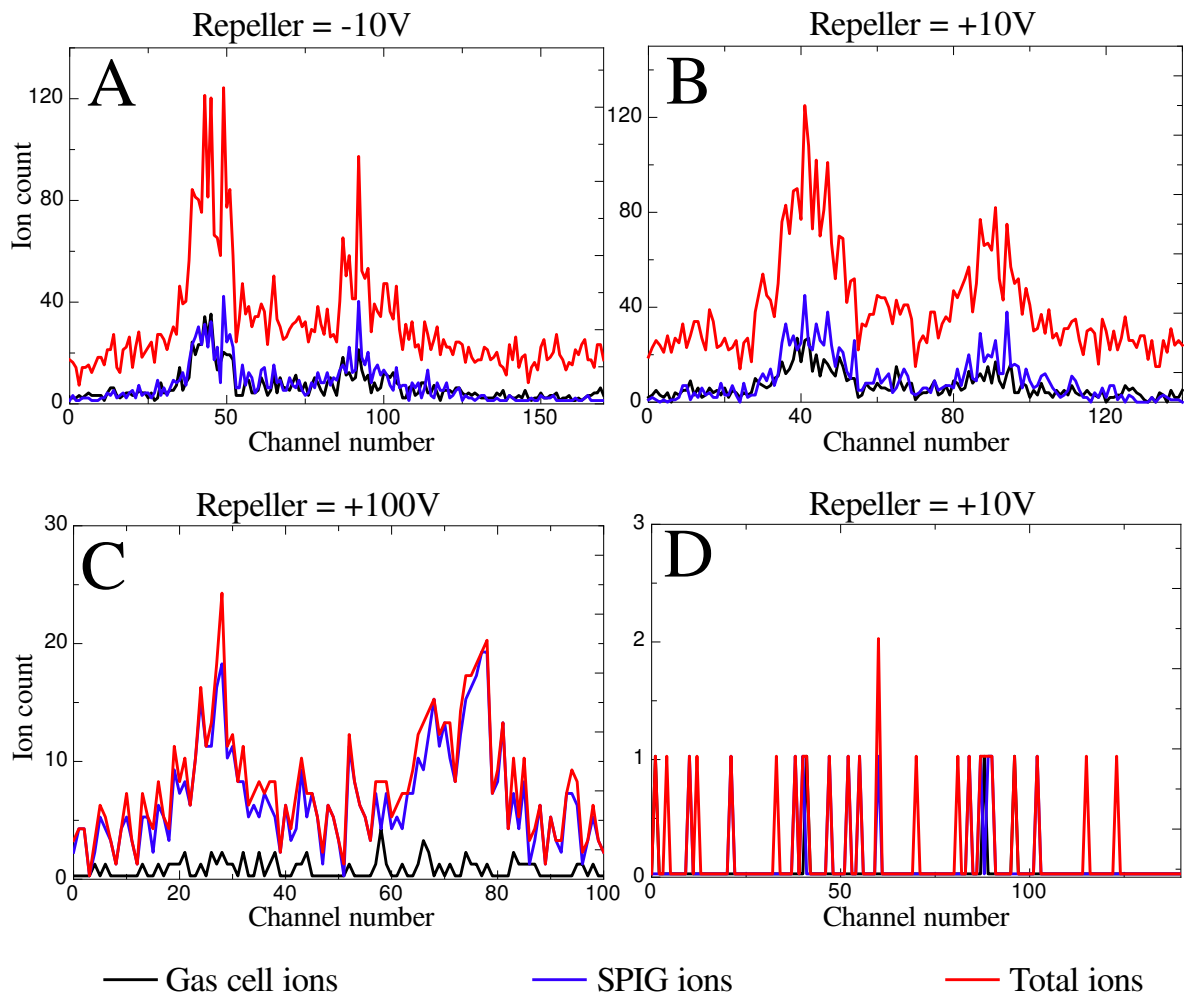


Figure 1.6: The number of bismuth photo-ions created inside the gas cell vs. the SPIG as a function of resonance step wavelength. With a closed gap between the SPIG and gas cell a repelling voltage of +100V shows suppression of the gas cell ions in spectrum C. Spectrum D shows suppression of gas cell ions with +10V with an open gap.

ions are detected coming from the SPIG and from the gas cell without any expected repelling effect. Increasing the repelling potential to +10 V shows little effect on the repelling, which is evident from plot B. With a repelling voltage of +100 V, on the other hand, an almost complete suppression of the gas cell ions is seen and only the ions that are created in the SPIG are detected demonstrating a working LIST method.

Plot D shows the effect of the pressure environment on the repelling behaviour. The spectra in plot D is measured without the sealing between the gas cell and repeller and shows only a background signal. This happens because without the sealing the gas is pumped away much more effectively and only a small neutral fraction of bismuth actually enters the SPIG. On the other hand, repulsion of the ions coming from the gas cell is now possible already at +10V because the momentum transfer from a low pressure gas flow to the ions is considerably smaller. Therefore, only background ions are detected.

1.3 Sextupole radio frequency ion guide

The LIST project was the motivation behind for the installation of a sextupole radio-frequency ion guide (SPIG) which replaced the traditional skimmer-based ion transportation system at IGISOL. A radio-frequency sextupole was first used for radioactive ion beam transport by Xu *et al.* [16], and has been used as a ion guide in a laser ion source by Van den Bergh *et al.* [17].

Using a SPIG is attractive for non-LIST use because of its capability to transport higher current beams with minimal space charge effects. A SPIG also creates a smaller energy spread than the skimmer-based system and improves the mass resolving power of the mass separator. Before the current SPIG installment, the first test of a SPIG structure, motivated by the energy spread improvement, was done at

IGISOL with a SPIG smaller in dimensions [2].

The current sextupole ion guide at IGISOL has a double SPIG structure, with two separate SPIG elements in series. The first SPIG after the repeller electrode is enclosed in order to produce a suitable pressure to ensure a collimated gas jet over the entire length of the SPIG. The gas inside the SPIG also cools and focuses the captured ions through collisions between ions and gas atoms. The second SPIG structure is open in order to pump the residual buffer gas away before the ions are accelerated further. An iris between the two SPIG structures provides an additional control over the pressure environment in the first SPIG. Figure 1.4 shows a photograph of the SPIG. A schematic representation of the experimental setup using the SPIG can be seen in Figure 1.1.

The total length of the SPIG system is about 170 mm. Right after the repeller electrode the six 4 mm diameter sextupole rods are arranged in a circle having an inner diameter of 10 mm, which is large enough for the 6 mm diameter laser beam to enter the SPIG. With a laser repetition rate of 10 kHz and gas jet velocity of 1000 m/s, the length of the SPIG allows each atom travelling inside to be exposed at least once to a laser pulse.

Inside the SPIG rod structure the rf-field forms a steep-walled pseudopotential in which the ions are trapped. The 3 to 4 MHz sinusoidal rf signal is applied to each rod so that adjacent rods are in the opposite phase to each other. The rf-amplitude is 0-600 V_{pp} to which an additional DC potential can be applied in order to create a potential gradient for ion transportation [13,18].

2 Simulation studies of the repeller electrode

Simulations were performed to investigate the repelling effect of the SPIG used in the LIST mode with Simion 8.0 simulation software. The simulations were used to study the effect of the repelling behaviour as a function of repelling voltage when the carrier gas type and distance between repelling electrode and ion guide were varied. These simulation studies were compared to experimental results. The repelling efficiency, defined as the percentage of ions repelled by a certain voltage is of interest, because if too high voltages are used in the repelling process, unwanted sparking may occur in the repeller electrode region.

The simulations were based on previous work performed for the IGISOL off line test rig, which included models for high pressure gas jets. These simulations are also similar to those done for the SPIG in reference [18]. In this section the simulation environment and the gas jet models are described only briefly. For more information the laboratory work report is included in the appendix of this thesis.

2.1 Simion simulation environment and simulation models.

2.1.1 Simion simulation software and the simulated repeller electrode system

Simion 8.0 is an ion optics simulation software tool [19] that can be used to solve the Laplace equation of an ion-optical system, and use the solved potential to transport ions through the system while studying the behaviour of the ion trajectories. The ion-optical system is given as differently shaped electrodes, each having their own adjustable potential [20].

A figure of the simulated repeller electrode system as it is drawn in Simion software is shown in Figure 2.1. The red disk with an aperture in the center, shown in the figure, is the ion source and models the standard exit hole nozzle. In the simulations the ions are produced inside the aperture from which they are accelerated and transported by the gas flow toward the repelling electrode (yellow), which is separated by 1 cm from the ion source. In addition to a 1 cm gap, a 1 mm gap was also simulated.

The sextupole rods, which are depicted in green, are also visible in the figure. A DC potential of -160 V was applied to the sextupole rods during the simulations. Simultaneously a sinusoidal rf-potential of 3 MHz and V_{pp} of 600 V could be applied to the sextupole rods so that adjacent rods have opposite phases. However, the rf-potential has little effect on the field lines at the repeller electrode aperture location where the electric field averages to the DC potential.

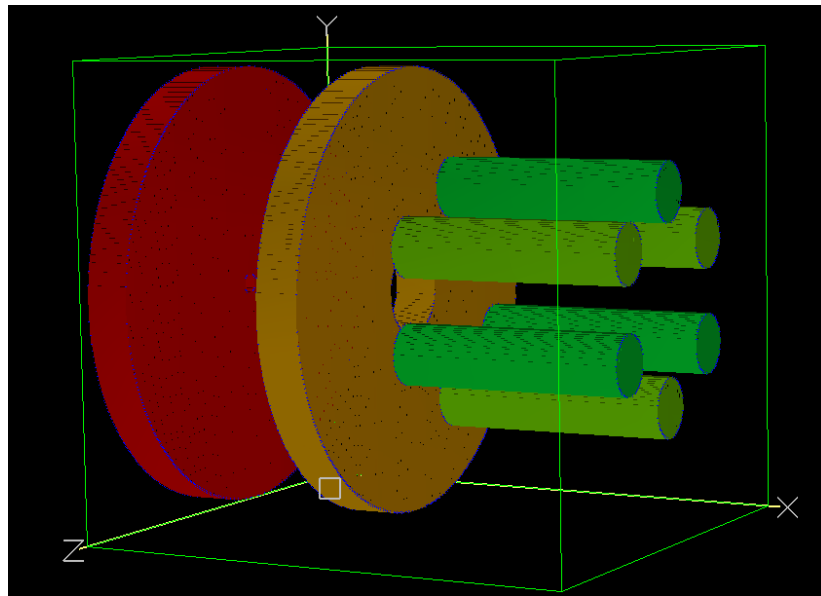


Figure 2.1: The simulated repeller electrode system showing the ion source (red), repeller electrode (yellow) and the SPIG sextupole rods (green). An AC potential can be applied to the SPIG rods.

The electric fields between the ion source and the repeller electrode are shown in Figure 2.2 with typical operating voltages. Each red line represents a 5 V change in the potential. The blue line marks the 0 V isoline. The figure includes the two repelling geometries, one with a 1 cm gap and one with a 1 mm gap between the ion source and repeller electrode. The difference of the field lines between the two geometries is visible in the figure and the effect of the potential of the sextupole rods can be seen as a protruding field into the repelling area.

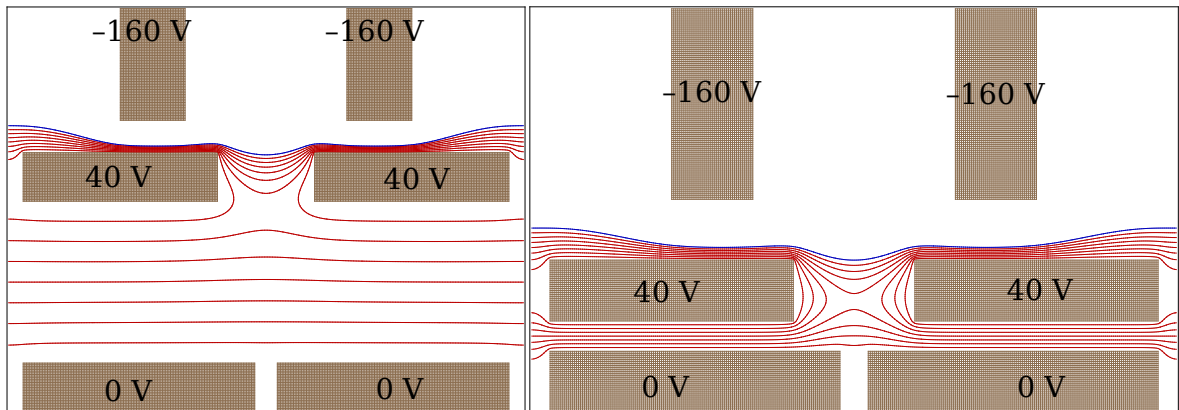


Figure 2.2: The electric field lines of the repelling electrode system with gap distances of 1 cm and 1 mm between the ion source and repeller electrode. The red lines represents a 5 V change in the potential and the blue line 0 V.

2.1.2 Gas models

Simion assumes a perfect vacuum which means that the ions are thought to have an infinitely long mean free path. This assumption does not hold in high pressure gas jet environments and thus two additional models were used for gas jet behaviour that could be programmed into the simulations via Simion's user programs. The user programs are used to call separate parts of the simulations such as ion movement or potential adjustment procedures and add or modify the behaviour of the simulation.

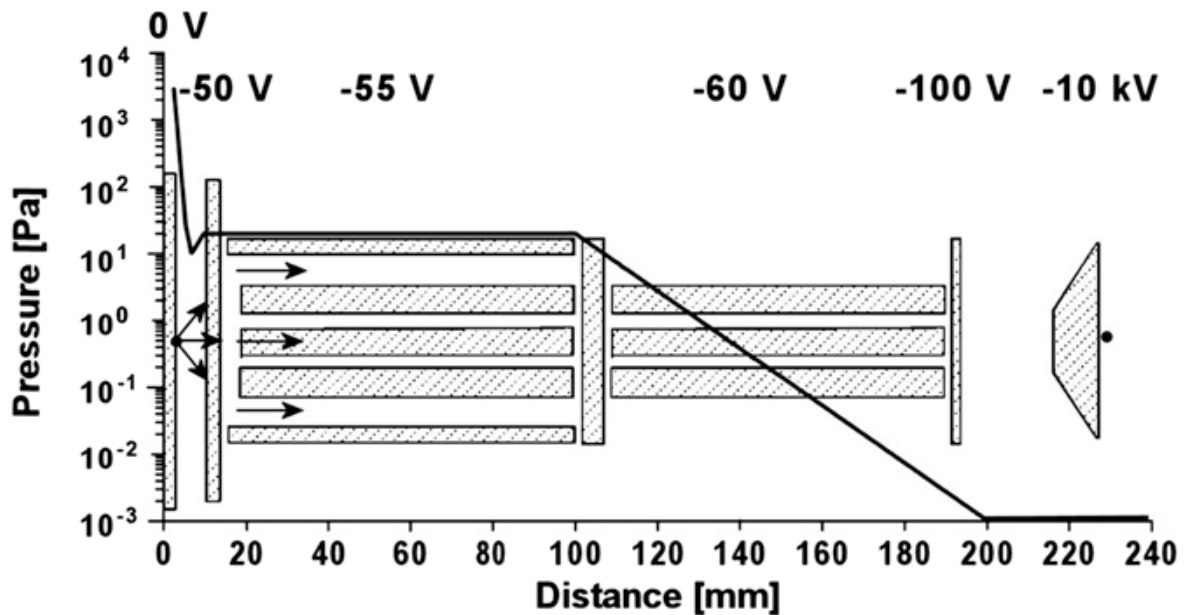


Figure 2.3: The pressure trend between the exit hole and extractor region that was used in previous simulations [18]. In this thesis only the pressure between the exit nozzle and repeller electrode is used.

With user programming, a hard sphere collision model [21] and explosion model (see the appendix) were introduced into the simulations. The hard sphere collision model was used to simulate elastic collisions between ions and background gas atoms by using a Maxwellian velocity distribution for the atoms and random collision angles. The collision probability was determined by the collision cross section, the relative velocity between an ion and gas atom and the carrier gas density. The collision cross section was determined by the van der Waals radii of the accelerated ion and neutral buffer gas atom. The carrier gas density was determined by kinetic gas theory with the aid of three dimensional pressure and temperature models.

Simulations were performed with the two typically used carrier gases, helium and argon with a gas cell pressure of 60 mbar. Nickel ions were simulated, representing the ion species used in the repeller electrode experiments. The buffer gases helium and argon act differently in the simulation not only because the gas atoms

differ in mass, but also because different van der Waals radii have been used, 1.40 Å and 1.88 Å, respectively [22]. The van der Waals radius of nickel was estimated to be around 1.60 Å.

The pressure trend used for the earlier SPIG simulation [18] is shown in Figure 2.3. For the current work only the trend between the exit nozzle and the repeller electrode is applied. The velocity of the gas is assumed to be constant at 1000 m/s in the case of helium and 500 m/s in the case of argon. The temperature of the gas is expected to fall to about 100 K as the gas jet exits from the nozzle and to reach room temperature downstream. This is also taken into account in the simulations.

2.2 Simulation results

2.2.1 Simulation of the repeller electrode

The simulations were performed for two gap sizes, 1 mm and 1 cm between the exit nozzle and repeller electrode for helium and argon buffer gases. The number of Ni⁺ ions in each of the simulations was 1000, created in random positions inside the nozzle aperture at the start of each run. The ions were transported from the aperture by the buffer gas collisions towards the repelling potential barrier. The potential barrier height, in other words, the repeller electrode voltage, was changed for each run and the number of ions that overcame the barrier and entered the SPIG were counted. The repeller voltage was changed from 0 V to 80 V in steps of 2 V in each simulation.

The simulation results are marked with solid lines and triangles, and are shown for the 1 cm gap in Figure 2.4a and for the 1 mm gap in Figure 2.4b. The ion yield is normalised to the number of ions obtained for 0 V in each case. In each simulation the voltages needed for a complete repelling of the ions are significantly higher than 1 V which would represent the kinetic energy of the Ni⁺ ions without buffer gas

collisions.

The actual experimental results of the repelling effect of Ni^+ ions are also shown in Figures 2.4a and 2.4b by circles and dashed lines for 1 cm and 1 mm gap sizes, respectively. The experiment was also done with the two buffer gases used in the simulations, helium and argon.

It is apparent from simulation and experimental data that the argon buffer gas can push the Ni^+ ions more efficiently over the potential barrier than helium, even though the argon gas velocity is half of that of helium. All the curves representing the argon buffer gas are located at higher repelling potentials than the corresponding curves for helium buffer gas. This is caused by the mass of an argon atom which is ten times heavier than the helium atom. In addition, a larger van der Waals radius of the argon atom compared to helium results in a collision cross section for argon over 30% higher.

The most striking difference between the simulation and experimental data can be seen in the 1 mm gap result illustrated in Figure 2.4b. The experimental data

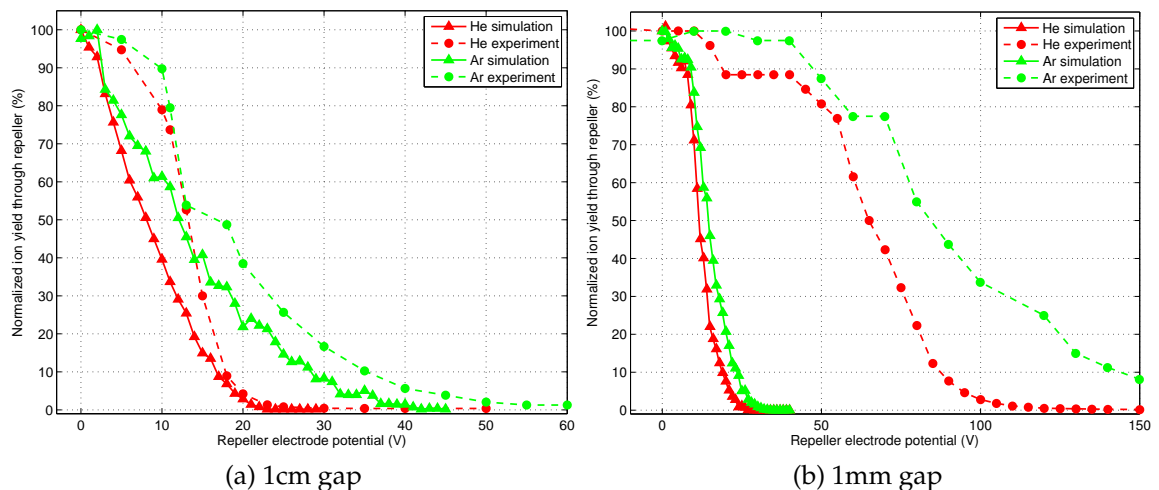


Figure 2.4: Simulation vs. experimental data of the ion count rate as a function of the repelling voltage with a 1 cm gap (a) and 1 mm gap (b) between the ion source and the repeller electrode.

shows significantly larger potentials for both helium and argon than the simulated data. Experimentally, repelling voltages over 100 V for helium and over 150 V for argon were needed for the full repulsion of nickel ions. The results might be explained as follows: with a 1 mm gap the pressure in reality is significantly higher downstream of the gas jet than was estimated in the simulations. Also the buffer gas flow in reality may be more parallel than the flow defined by the explosion model. The effect of different simulation environments, such as the background pressure, is discussed in section 2.2.2 below.

On the other hand, the experimental results of the 1 cm case in Figure 2.4a show approximately the same potential needed for total repelling of the Ni^+ ions as in the corresponding simulations. For helium, the potential which repels over 99% of the ions, is about 24 V in both simulation and experiment. For argon the total repulsion of ions happens at a potential of a little over 40 V in the simulation and approximately 50 V in the experiment. In argon, both simulation and experiment exhibit a tail in the curve.

Although the simulation of the 1 mm gap did not match the corresponding experimental data, there is still a clear, albeit not a large, difference in the simulated data between the 1mm and 1cm gap. The simulated difference in the repelling potential between the two gap sizes is about 5 V for helium and 10 V for argon at a repelling efficiency of 99%.

In summary, the simulations were able to qualitatively reproduce a similar behaviour of repelling efficiency as a function of the repelling potential that was measured in the experiments performed in a controlled environment similar to the simulation conditions. The differences between simulation conditions and experimental environment may explain why the simulation data is quantitatively quite different from the experimental data in the case of the 1 mm gap. The simulation of the 1 cm gap, on the other hand, exhibited also quantitatively good agreement with the

experimental data.

Both the experiments and the simulations presented in this chapter demonstrate that the full suppression of the non-neutral part of the gas jet, which is an important condition for the LIST method, is achieved by repelling potentials much larger than would be expected if the ions had only an initial kinetic energy comparable to the gas jet velocity. The simulations show that the need for several tens of volts for the full repulsion of the ions can be explained by the constant collisions between the fast moving background buffer gas atoms and the ions.

2.2.2 Influence of the simulation environment

A series of simulations were run using argon buffer gas and a 1 mm gap in order to test the effect of different environmental parameters such as the higher pressure conditions described in the previous section. In Figure 2.5 the repelling effect is plotted against the repelling potential for different scenarios. The experimental data is plotted as circles and the original simulation data is plotted as triangles from Figure 2.4b. High pressure conditions were tested by keeping the pressure at a constant 50 mbar throughout the ion guide/repeller region during the simulations. In the figure the repelling effect in that case is illustrated with diamonds. Although the simulation shows a weaker repelling efficiency than the original simulation, it does not yet match the experimental values.

The strongest weakening of the repelling effect is shown by modifying the gas flow velocity direction. In the simulations with the explosion model the velocity of the buffer gas coming out of the nozzle is considered to be isotropic. Simulating a gas velocity that is directed towards the repeller as a parallel flow weakens the repelling efficiency considerably as is seen by the red line in Figure 2.5. This suggests that the repelling may be more effective at lower repelling potentials if it is done perpendicular to the optical axis and not only towards the gas flow.

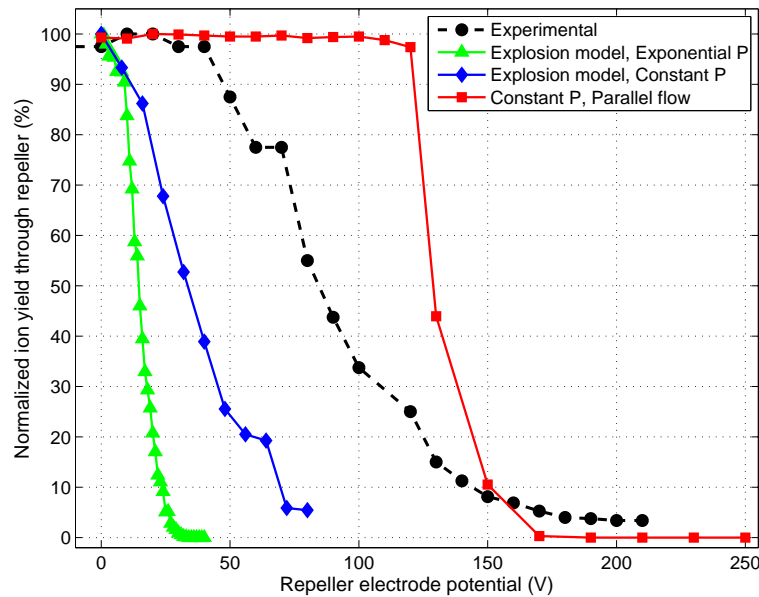


Figure 2.5: Comparison of simulation conditions. Both simulations with (triangle, diamond) and without (square) the explosion model, and between exponentially decaying pressure (triangle) versus constant pressure (diamond, square) have an effect on the repelling voltage. Experimental data is plotted for comparison (circle).

2.2.3 Transverse ion collector

Because the repelling voltage had to be increased considerably at small gap distances the system becomes susceptible for unwanted discharging. More effective repelling geometries were therefore studied. A more effective repelling means that the ions are restrained and prevented successfully from entering the SPIG region using lower repelling potentials.

Instead of pushing the ions against the flow of the buffer gas with the repeller electrode, a model of a transverse ion repelling system was simulated. This is realized by placing a simple set of deflection plates between the ion source and the repeller electrode. The plates deflects the ions in the transverse direction, and thus the ions do not have to work against the gas flow. The deflector plate system in the simulation can be compared the ion collector of the LISOL laser ion source gas cell

described in reference [23]. The ion collector in this simulation is positioned after the exit hole and not inside the gas cell as is the case in [23].

A cross section of the simulated repeller electrode system with deflection plates acting as an ion collector is illustrated in Figure 2.6. The plates have dimensions of 3×6 mm. The gap size in this case is 5 mm. Figure 2.7 shows the electric field lines of the simulated system. The positive plate of the ion collector is kept at the same potential as the SPIG repeller electrode. The negative plate that actually collects the ions is simulated either grounded to 0 V or with the same absolute voltage as the positive plate but negatively biased. Figure 2.7 also shows ion trajectories of a few Ni^+ ions run within the simulations.

The simulation environment used was identical to the simulations without the ion collector plates describe in the previous sections. Three simulation runs were

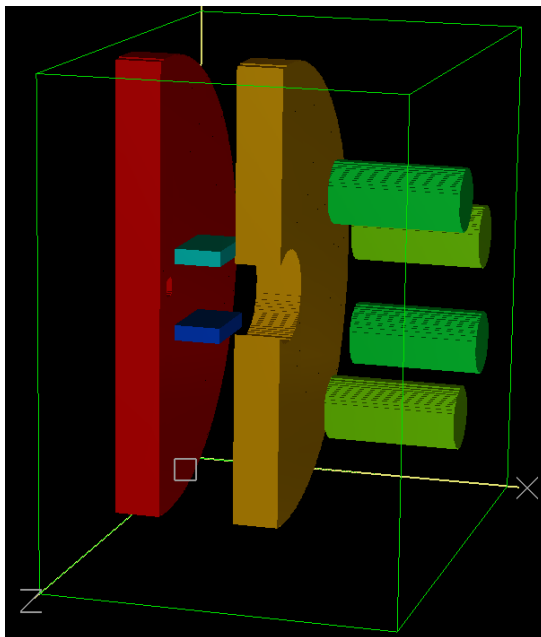


Figure 2.6: A cross sectional 3D model of the simulated repeller electrode system with deflection plates (blue) as the ion collector

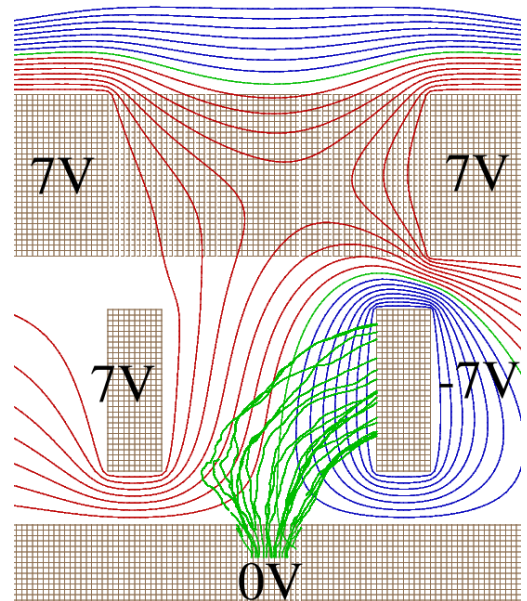


Figure 2.7: Electric field lines of the ion collector at the front of the repelling electrode. The collecting electrode was simulated with negative voltage and 0 V. Ion trajectories are also shown.

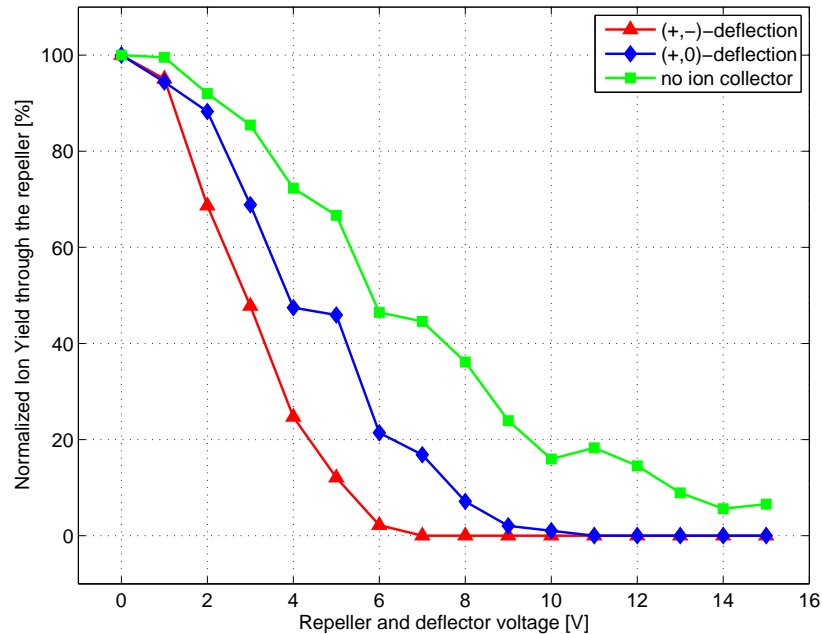


Figure 2.8: The simulation results of the transverse ion collector repelling. The normalized number of ions going through to the SPIG are given as a function of the repelling voltage. (+,-) denotes that the collecting plate is in negative voltage and (+,0) denotes that it is grounded to 0 V. A simulation result without the ion collector is shown also.

performed, and in order to compare the results a run without the ion collector was made for comparison. The ion collector simulations were done with negative and grounded collector plate potentials. The repelling potential was changed from 0 V to 15 V in steps of 1 V. Each repelling voltage was simulated with 350 ions.

Figure 2.8 shows the results. The green curve illustrates the simulation without the ion collector plates. The repelling with the ion collector plate grounded shows about 30 % more effective repelling at 50 % repelling efficiency than the repelling without the ion collector. Biasing the collector plate to negative voltage provides 50% more effective repelling than without the ion collector.

Especially noteworthy is the absence of the long tail as is seen in the simulation without the ion collector. At an ion yield of 1% the repelling with the negatively

CHAPTER 2. SIMULATION STUDIES OF THE REPELLER ELECTRODE

biased ion collector is already over 50 % more efficient than without the ion collector.

In conclusion the simulations showed a noticeable improvement in the repelling effect when using the ion collector to deflect the ions transversely. The problem with the ion collector design presented here is that the plates between the ion source and the repeller electrode form strong electric gradients, where potential sparking might occur. Therefore, the system used by LISOL whereby the ion collector is before the gas cell exit nozzle is preferred. However the electrodes need to be screened from the weak plasma inside the gas cell in order to operate efficiently.

3 Studies for optimization of the LIST method

3.1 Motivation

A good efficiency of the LIST method requires efficient resonant ionization of the atoms inside the SPIG. There are two main factors that affect the photo ion yield resulting from the resonant ionization process. These are the efficiency of the transportation of neutral atoms from the ion guide through the exit nozzle to the SPIG, and the duty cycle of the lasers [24].

Because of the difference between the gas cell inlet pressure and the background pressure at the SPIG entrance, the buffer gas flow in the nozzle region is supersonic. This will cause the gas jet exiting from the nozzle to behave in a complicated manner. The jet forms multiple shock structures whose shape depends on the nozzle design, pressure conditions and the type of buffer gas. The shape of the gas jet, especially the width, determines how the gas will be coupled into the SPIG through the 6 mm aperture of the repeller electrode. When the gas is injected efficiently to the SPIG the number of gas atoms which are geometrically overlapped with the lasers is high and the ionization efficiency increases.

The overlap efficiency is also affected by the duty cycle of the laser system, which in the current system is fixed to 10 kHz. So that each atom has a chance to interact at least once with the propagating laser pulses, the SPIG needs to be 10cm long for a jet velocity of 1000 m/s.

The question of how to couple the gas jet as efficiently as possible provides the motivation for the work in this chapter. In the following sections, firstly, the theory of supersonic gas jets and the motivation for the nozzle design is shortly discussed.

In later sections the gas jet dimensions are studied with gas jet photography in a similar manner as done in reference [25]. In this work we focus on how different pressure environments, and different exit nozzle shapes and sizes affect the gas jet diameter and its coupling to the SPIG.

3.2 Supersonic gas flow

In this section, firstly a few basic fluid dynamics equations concerning supersonic flow are shortly derived in similar manner as done in basic fluid dynamics books, for example in reference [26]. The discussion is continued by describing how supersonic flow through a converging-diverging nozzle forms and evolves when the pressure difference between a high pressure reservoir and an extraction chamber is increased. Also a converging-only nozzle is discussed.

3.2.1 Area-velocity and Area-Mach number relations

In subsonic gas flow, the highest velocity of the gas in a duct is naturally expected to be at the position of the narrowest diameter of the duct. With supersonic flow, however, the opposite is true. Narrowing of the duct actually slows down the flow. In the following, this behaviour is shown by deriving the relationship between the duct area and flow velocity.

If we have stationary flow, the mass density does not change. This leads to the following continuity equation, which is applicable throughout the nozzle:

$$\frac{dm}{dt} = \rho Au = \text{constant}, \quad (3.1)$$

where ρ is the gas density, A is the duct area, and u is the gas velocity. In other words equation (3.1) means that the flow rate does not vary in the duct. By taking

the logarithm of the continuity equation and differentiating it we get

$$\frac{dp}{a^2\rho} + \frac{dA}{A} + \frac{du}{u} = 0, \quad (3.2)$$

where dp has been rewritten in terms of the speed of sound $a = \sqrt{(dp/d\rho)_0}$. By assuming an inert, adiabatic and inviscid (isentropic) gas, the following differential form of Bernoulli's equation can be assumed:

$$dh + d\left(\frac{u^2}{2}\right) = \frac{dp}{\rho} + udu = 0, \quad (3.3)$$

where we used the fact that the process is isentropic, $dh = U + vdp = TdS + vdp = vdp$. Now we can write equation (3.2) with the help of equation (3.3):

$$\left(\frac{u^2}{a^2} - 1\right) \frac{du}{u} = \frac{dA}{A} \quad (3.4)$$

from which we can finally conclude by replacing u/a with the Mach number $M = u/a$:

$$\frac{dA}{A} = (M^2 - 1) \frac{du}{u}. \quad (3.5)$$

Equation (3.5) shows how the narrowing of a duct ($dA < 0$) in subsonic flow increases the velocity ($du > 0$) but in supersonic flow it decreases the velocity ($du < 0$). Equation (3.5) also states that at the throat ($dA = 0$) of a nozzle the flow of the gas reaches the speed of sound ($M = 1$). In the case of a converging-diverging nozzle such as in Figure 3.1, after the throat the nozzle opens ($dA > 0$) and the gas expands to supersonic flow.

Continuing further with the continuity equation (3.1) we note that a converging-diverging nozzle agrees with the following:

$$A\rho u = A_{min}\rho'u' = const, \quad (3.6)$$

where A_{min} , ρ' and u' describe the conditions at the throat of the nozzle. By applying the ideal gas law, sound-velocity equation and Mach number definition as well as the definitions of stagnation pressure and temperature to the continuity equation, we can derive the Area-Mach number relation:

$$\frac{A}{A_{min}} = \frac{1}{M^2} \left(\frac{2}{\gamma + 1} \left(1 + \frac{\gamma - 1}{2} M^2 \right) \right)^{\frac{\gamma + 1}{\gamma - 1}}. \quad (3.7)$$

In the equation γ is the ratio of specific heats which for monoatomic gases is $\gamma = C_p/C_v = 5/3$. As we now have the variation of Mach number through a nozzle, other parameters such as temperature, density and pressure can be calculated. Respectively, the relationship between pressure and Mach number can be calculated using the equation below

$$\frac{P}{P_{in}} = \left(1 + \frac{\gamma - 1}{2} M^2 \right)^{-\frac{\gamma}{\gamma - 1}}, \quad (3.8)$$

where P_{in} is the static pressure for $M = 0$ in other words the pressure of the reservoir.

We know from equation (3.5) that when the nozzle is operating as desired, the Mach number equals to $M = 1$ at nozzle throat. Thus we can define from equation (3.8) the so-called design operating condition for a converging-diverging nozzle. At the design condition equation (3.8) reduces to:

$$\frac{P}{P_{in}} = \left(\frac{2}{\gamma + 1} \right)^{\frac{\gamma}{\gamma - 1}}, \quad (3.9)$$

because the Mach number is unity. The equation above for monoatomic gases gives the pressure ratio $P/P_{in} = \sim 0.49$.

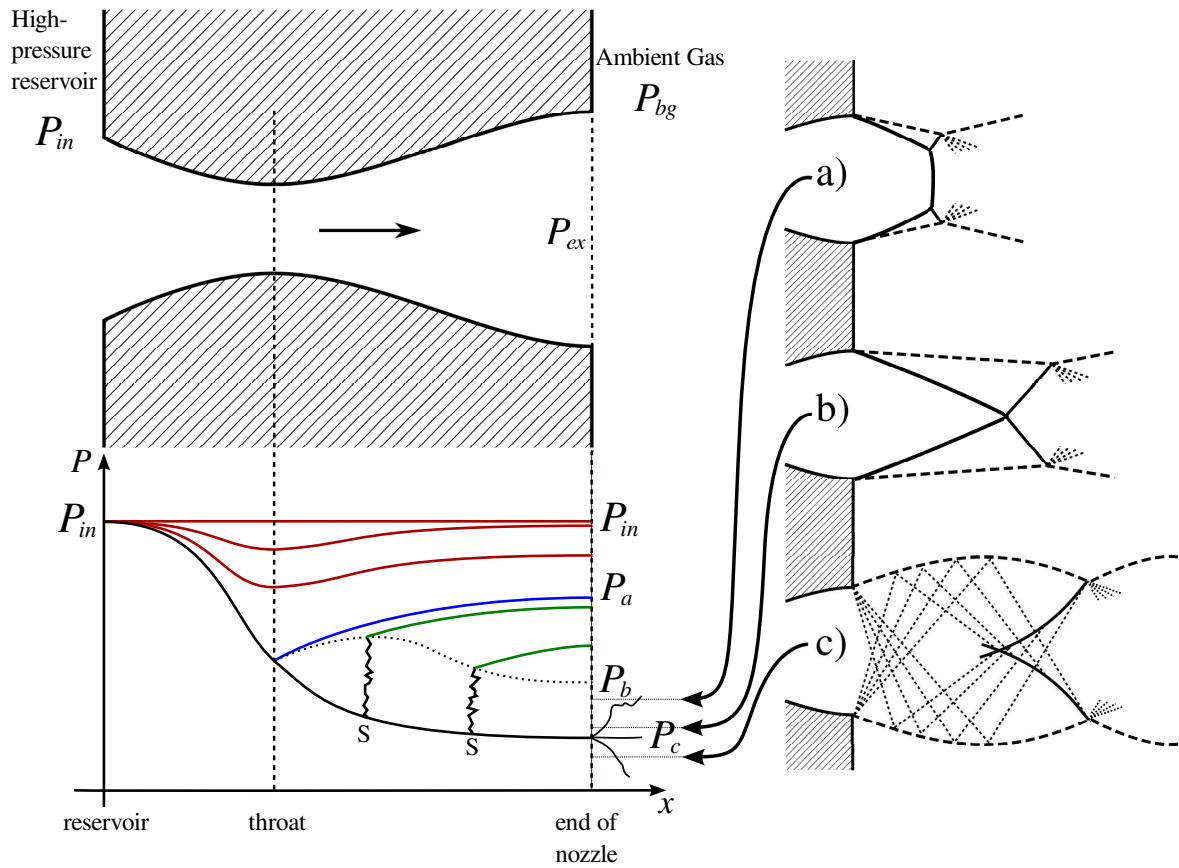


Figure 3.1: The pressure as a function of distance for different flow regimes. Red curves: subsonic, blue curve: sonic at throat, green curves: shock disk inside the nozzle (marked with S). The shape of the converging-diverging nozzle is given also above the plot. The illustrations a) and b) show overexpanded jets, and c) an underexpanded jet.

3.2.2 The Gas flow regimes for a converging-diverging nozzle

The characteristics of gas flow inside a converging-diverging shaped nozzle vary depending on the pressure condition, namely the pressure difference between the gas reservoir and expansion chamber. In Figure 3.1 the pressure behaviour is given as a function of distance through the nozzle for different pressure conditions. The pressure of the high-pressure reservoir P_{in} , the pressure inside the expansion chamber P_{bg} , and the pressure at the nozzle exit P_{ex} are shown in the figure. As the pressure

difference between P_{in} and P_{bg} is increased the characteristics of the gas flow change. The different characteristics form flow regimes that are briefly described here.

The subsonic regime is shown by red lines in the (x,P) -plot. In this regime $P_{ex} = P_{bg} > P_a$ and the flow is subsonic everywhere inside and outside the nozzle. When the pressure difference P_{in}/P_{bg} is increased, the background pressure P_{bg} reaches the pressure P_a , and the flow at the throat of the nozzle is sonic. After this, when $P_{bg} < P_a$, shock structures start to form in the diverging section of the nozzle. By reducing the nozzle pressure P_{bg} towards the pressure P_b the shock structure becomes more prominent and moves to the nozzle exit in which $P_{ex} = P_{bg} = P_b$.

Continuing the increase of the pressure difference so that $P_c < P_{bg} < P_b$, causes the shock disk to move outside of the nozzle. In fact, the gas inside the diverging section of the nozzle has expanded so strongly that the pressure at the exit $P_{ex} < P_{bg}$ and thus the pressure equalizing oblique shocks compress the jet. In this regime the jet is said to be overexpanded. From the rim of the nozzle oblique shocks appear which meet a shock disk normal to the axis which is called the Mach disk. At the meeting point of the oblique shock and the Mach disk is the Mach triple point where a third, reflected shock is emitted towards the jet boundary, and is reflected as an expansion fan. This flow is depicted in the illustration a) of Figure 3.1.

When the pressure difference is increased again, so that $P_c < P_{bg} < P_b$ still holds, the Mach disk continues to shrink and is finally no longer present, and the shocks from the nozzle rim simply meet and reflect off each other. This is depicted in illustration b).

The reduction of the pressure reduces the strength of the shocks in the overexpanded regime. The strength reduces until $P_{bg} = P_c$ and the shocks emitting from the rim have no strength. In this regime the jet is fully expanded and exits as a parallel beam. The flow is supersonic throughout the nozzle and outside as well. This is the condition when the nozzle is operating at its design condition specified by

equation (3.9).

By continuing to increase the pressure difference until $P_{bg} < P_c$ the jet becomes underexpanded. The pressure at the nozzle exit P_{ex} is larger than the chamber pressure P_{bg} . When the jet exits the nozzle it is radially accelerated and the jet diameter increases while the jet pressure reduces until it becomes less than the chamber pressure P_{bg} and the jet is once again in an over-expanded region which reduces the jet diameter. In an underexpanded jet, the jet boundary emitted from the nozzle rim has to adapt to the chamber pressure immediately, because pressure equalizing oblique shocks as in the over-expanded jet are no longer present. The pressure equalization happens by emanating an expansion fan, similar to the triple point of the overexpanded jet, but now emanating directly from the nozzle rim. This fan is the so-called Prandtl-Meyer expansion fan which explains how a smooth turn in the jet flow can be accomplished isentropically. The expansion waves reflect from the jet boundary and intersect to form a curved shock. This is shown in illustration c) of Figure 3.1.

In the underexpanded jet, the formed curved shock wave meets the jet boundary and causes a new formation of expansion fan to emanate from the contact point and the process begins again and repeats itself. The jet undergoes successively over-expanded and underexpanded regions until viscous effects at the jet boundary destroys the jet. This is seen as several shock diamonds downstream of the jet. It should be noted however that overexpanded jets also have repeating characteristics and exhibit shock diamonds.

The increase of the pressure difference even further expands the jet steeply when exiting the nozzle and a Mach disk forms normal to the symmetry axis. This type of jet is said to be strongly underexpanded and is equal to the strongly underexpanded free jet emitted from a converging-only nozzle described in the next section.

3.2.3 The formation of an underexpanded free jet

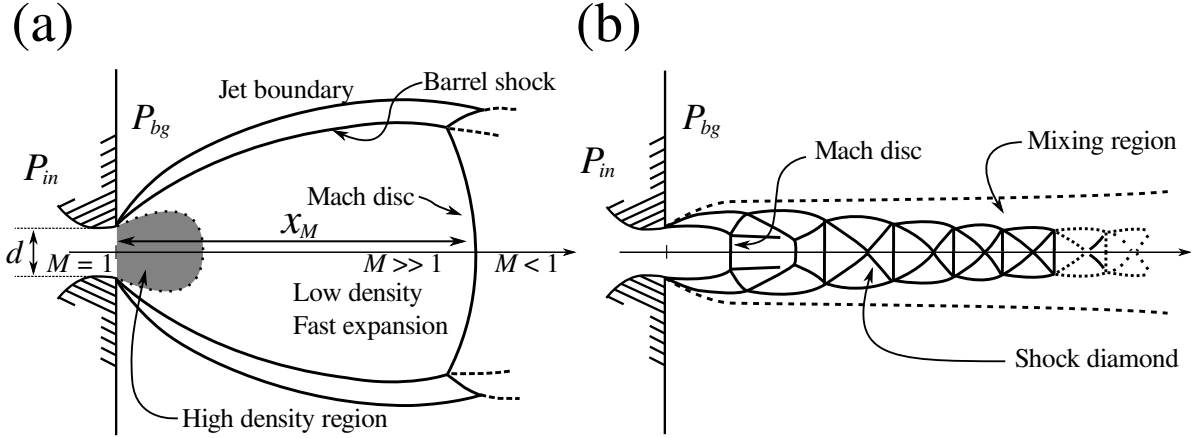


Figure 3.2: The structure of an underexpanded free jet when the pressure ratio $P_{in}/P_{bg} > 100$ (a) and when $P_{in}/P_{bg} \ll 100$. The Mach disc position x_M , the throat diameter d and Mach numbers in the strongly underexpanded jet are shown in the figure.

When a gas jet expands out of a gas cell through a converging-only nozzle to a low pressure extraction chamber, an underexpanded free jet forms in the extraction region as in the case of a converging-diverging nozzle. That is, if the extraction chamber background pressure is much below the inlet pressure. The converging-only nozzle has the narrowest duct at the exit where the Mach number is near $M = 1$. Right after the exit the gas can freely (free jet) expand into the extraction chamber and starts to accelerate to supersonic velocities [27].

As the free gas flows supersonically into the low pressure region shock waves are formed inside the jet. The shock waves begin as an expansion fan, which is emitted from all points of the nozzle circumference. The expansion fan is reflected as compression waves at the jet boundary and consequently forms the barrel shock. The compression waves coalesce further into a Mach shock disc normal to the axis. See Figure 3.2 [28].

At pressure differences $P_{in}/P_{bg} \ll 100$ the free jet shows a structure of repeat-

ing multiple shocks which form shock diamonds in the same way as the underexpanded jet from a converging-diverging nozzle. The shocks repeat themselves until turbulent mixing starts to dominate the flow downstream. The structure of an underexpanded free jet is shown in Figure 3.2b.

When the pressure difference between the background and reservoir pressures grows even greater so that $P_{in}/P_{bg} > 100$, the free jet starts to show the behaviour associated with a strongly underexpanded free jet. Illustration (a) shows the behaviour of such a jet. The high density gas exits the nozzle and starts to accelerate to high speeds $M \gg 1$ while the density drops. The fast flowing gas impacts against the Mach disc where the shock may be so strong that the flow continues as subsonic and only a single shock structure dominates.

In short, the typical characteristics found in a strongly underexpanded free jet are the strong expansion of the gas jet after the nozzle, the formation of a barrel shock near the jet boundary, and the formation of the Mach disc as a single shock structure.

3.2.4 Mach disc position

The shape and size of the Mach disc in an underexpanded free jet, as well as its location, are determined by the ratio of gas cell pressure P_{in} and background pressure P_{bg} . It was experimentally found by Ashkenas and Sherman that the Mach disc location x_M relates to the nozzle throat diameter d , and to the ratio of the pressures P_{in}/P_{bg} in the following way [28]

$$x_M = 0.67 \cdot d \left(\frac{P_{in}}{P_{bg}} \right)^{1/2}. \quad (3.10)$$

This result applies to pressure ratios $15 \leq P_{in}/P_{bg} \leq 17000$ and is independent of the ratio of specific heats γ and thus should be applicable to any gas.

3.3 Experiments for gas jet studies

3.3.1 Exit nozzle shapes

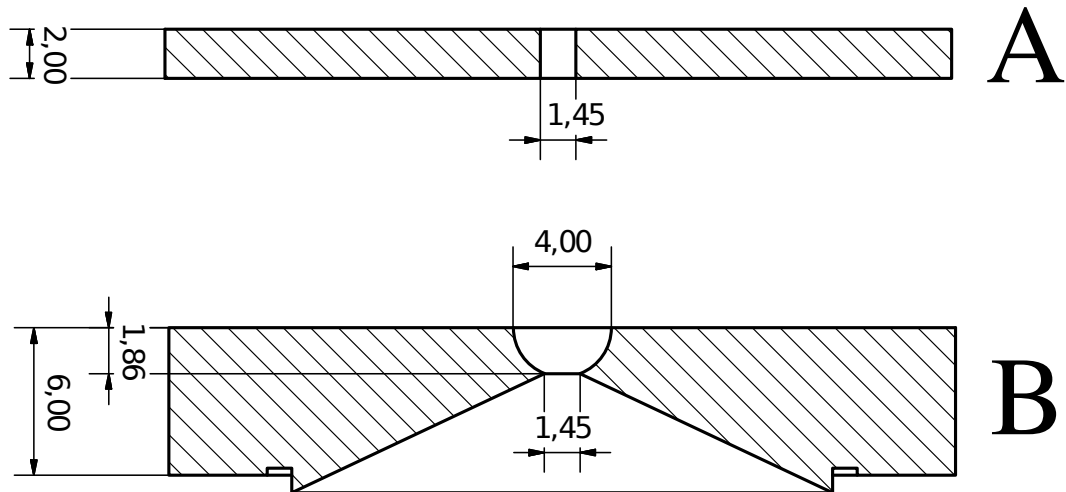


Figure 3.3: Schematic drawings of the two nozzle types studied with the gas jet photography in this work. (A) standard exit hole (B), converging-diverging nozzle

In this work three different nozzles were studied of which two were standard exit hole type nozzles in use at IGISOL and one converging-diverging nozzle. The motivation for studying the 0.7 mm and 1.45 mm diameter exit holes is that the typical exit hole size used with IGISOL ion guides is 1.2 mm and for a gas cell operated as a laser ion source, the exit hole size is approximately a factor of two smaller in order to increase the evacuation time and thus to achieve neutralization of the recoiling nuclei [2, 29]. Schematic pictures of the two nozzle types are shown in Figure 3.3.

The converging-diverging nozzle was shaped so that the nozzle would operate at the design condition with the achievable pressure conditions. This would create a narrow and well-collimated gas jet which could be coupled into the SPIG.

The dimensions of the converging-diverging nozzle have been estimated from equations (3.7) and (3.8). At the time of the design of the nozzles the pressure ratio between the ion guide inlet and extraction chamber was about 1% due to the limited

pumping capacity. Equation (3.8) was solved for this pressure difference resulting in a design condition Mach number $M = 4$, from which the relationship between nozzle area at the exit compared to the the throat location can be calculated using equation (3.7). The calculated relationship is about 5.6 and thus a diameter ratio of approximately 2.4 between the nozzle exit and throat is required. An exit diameter of 4mm has therefore been specified for the converging-diverging nozzle.

3.3.2 Experimental setup for gas jet photography

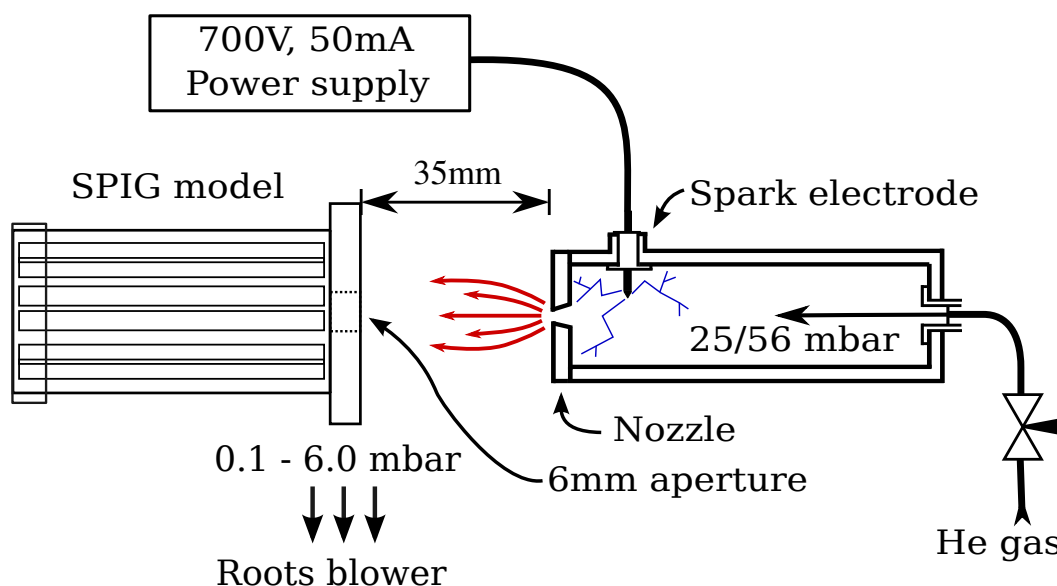


Figure 3.4: Schematic illustration of the experimental setup for gas jet photography.

The gas jet photography studies were performed in an IGISOL off-line setup designed for a new ion-guide quadrupole mass spectrometer system. The off-line setup contained an arc discharge gas cell. The different nozzle types can be mounted to the head of the gas cell which has an outer diameter of 3.5 cm. The gas cell head is in the center of a vacuum chamber measuring $\sim 0.5 \times 0.5 \times 0.5$ m with a viewing window on the side of the chamber allowing for visual access. An optional perspex model of the SPIG can be mounted on the vacuum chamber flange so that the re-

sulting distance between the gas cell and the SPIG model is about 3.5 cm. In order to have an efficient removal of the jet gas, the vacuum chamber is connected via a valve to a Roots blower with a specified pumping speed of 4000 m³/h. A schematic picture of the experimental setup is shown in Figure 3.4.

In the arc discharge gas cell a plasma is produced by applying voltage on a needle electrode from which an electrical discharge hits the grounded inner wall of the gas cell. A voltage of ≥ 300 V from a 50 mA current limited power source is needed to start the discharge. In order to have visible glow of the gas jet exiting the gas cell the voltage is raised to 700 V.

Photography of the gas jets was performed through the vacuum chamber window with a Casio Exilim Ex-F1 PRO digital camera, which was mounted to a fixed support so that each photograph could be taken at exactly the same position. The camera was positioned so that the gas jets would be photographed in a perpendicular geometry at a distance of about 20 cm. Due to the limited size of the window this was not always accomplished. The camera was manually set to a sensitivity of ISO 100, an aperture of F7.5 and an exposure time of 1 second. Long exposure times were possible as long as the gas jet was stable. Photographs were saved in RAW format so that the images would be as little preprocessed as possible.

In order to reduce scattered light to the chamber, open parts of the chamber window were covered during the photography. Black cardboard was placed behind the gas jet so that the fluorescence emitting from the jet would not be reflected from the vacuum chamber walls. With these precautions and with a long exposure time the resulting photographs had low noise.

3.3.3 Gas cell and background pressures

The gas cell was maintained at a high pressure with a constant gas flow of helium or argon through a needle valve. The gas cell inlet pressure was monitored with a

CHAPTER 3. STUDIES FOR OPTIMIZATION OF THE LIST METHOD

DI2000 Leybold capacitive pressure sensor attached to the gas line. The background pressure was measured with a TPR-010 Balzers Pirani gauge attached to a flange on the vacuum chamber, about 20 cm away from the gas jet region.

The photographs were taken using different nozzle types with constant gas cell pressure while varying the background pressure by adjusting the valve between the chamber and the Roots blower. Each nozzle type was photographed with two gas cell pressures: 56 mbar and 25 mbar. The background pressure was roughly varied from 0.1 mbar to 6 mbar while taking about 10 photographs at evenly spaced pressure intervals.

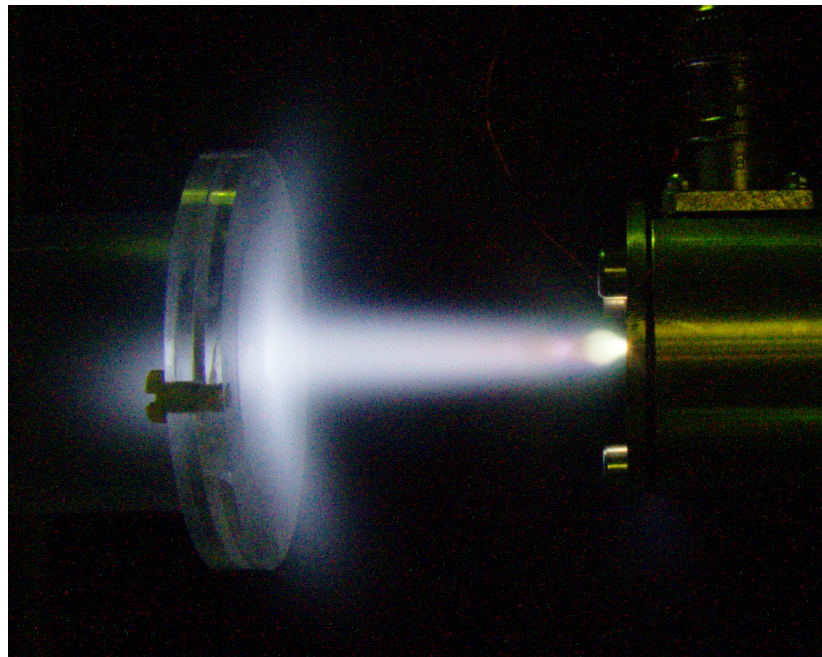


Figure 3.5: An example of a photograph of a jet formed with the converging-diverging nozzle. A shock structure is faintly seen immediately after the nozzle on the right.

3.3.4 Gas jet fluorescence

The discharge plasma inside the gas cell mainly consists of neutral ground state atoms in which positive and negative ions, free electrons and atoms in excited states are embedded. Metastable excited states with millisecond lifetimes are formed in the carrier gas. The relaxation of the states can be seen as a glow of the gas jet that grows fainter with increasing distance from the exit nozzle.

The excited states and the reactions in which they formed and subsequently depopulated are difficult to determine without spectroscopic measurements of the after glow. The production of metastable states can occur via inelastic scattering of electrons, ion-atom impact excitation, or in electron-ion recombination. The relaxation of the states can happen via various reactions, which can be affected by impurities in the gas. For more details see references [30,31].

In a local region, the gas jet emits the fluorescence most strongly where the gas density is the highest. Essentially what the photographs show, is the emitted fluorescence of the three dimensional gas jet projected onto a two dimensional profile. This is taken as an indirect representation of the gas density. The characteristics of the jets, including the width and in many cases shock structures, can be seen from the fluorescence. An example of a photograph taken with a 1.45 mm converging-diverging nozzle with 56 mbar of gas cell pressure and 5.6 mbar of background pressure is shown in Figure 3.5. For a more clearer depiction of the intensity change, a contour map is shown in Figure 3.13.

3.3.5 Gas jet analysis procedure

In order to have a more quantitative approach to the analysis of the gas jet, the FWHM of the jet at a constant distance from the nozzle was determined with a consistent procedure. This includes visual inspection of the photographs for possible

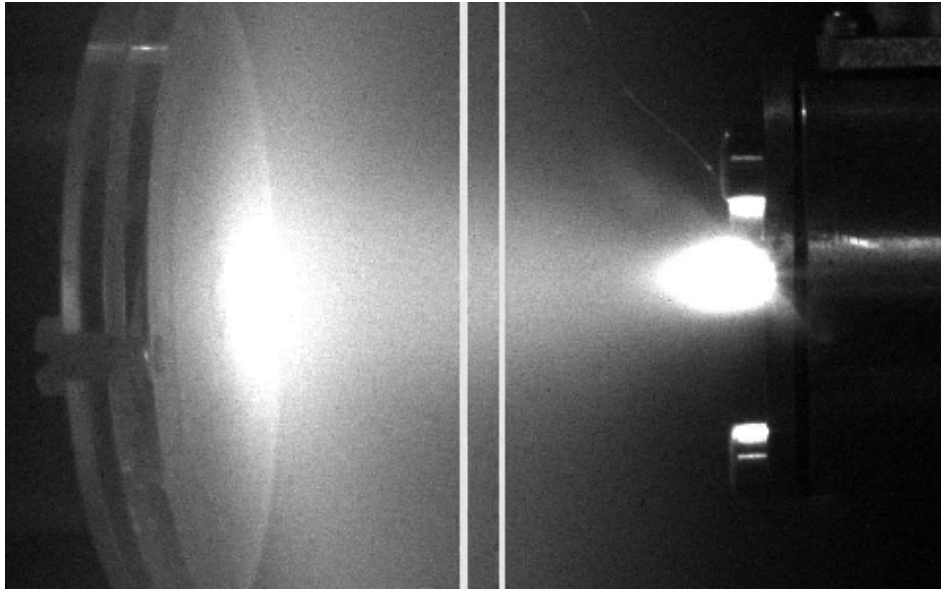


Figure 3.6: A gray-scale gas jet photograph representing the summed colour channels. The white lines show the location and width of the slice taken from each photograph.

artefacts, the determination of the nozzle position, taking a slice of the photograph for the determination of an intensity curve, and fitting the intensity curve with an appropriate function.

Each photograph, in 48-bit integer RGB colour presentation, was loaded by a Matlab [32] script. For the intensity determination, an average of the colour channels of each pixel was made, as the colour information is not needed for absolute brightness. The brightness value of each pixel was taken to directly represent the intensity of the fluorescence at the location of the pixel. One pixel represents the sum of the all intensity projected from the inside of the jet towards the camera eye at the pixel location.

The distances in the analysis procedure are in the units of pixels. To convert pixels to millimeters, a relationship was determined by measuring the size of the SPIG model in pixels. From the known SPIG model size a conversion factor of about 0.07 mm/pixel was determined.

After the colour channel averaging, a 40 pixel or ~ 2.5 mm wide vertical slice is made at a distance of about 2 cm from the gas cell. Each 40 pixel row is summed representing an average horizontal intensity of the 2.5 mm slice at a certain radial distance from the nozzle axis. The corresponding error is determined by calculating the standard deviation of each pixel row. Figure 3.6 shows an example photograph with the location and width of the slice as two white lines.

The slice translates into an intensity curve as a function of radial distance from the nozzle axis for each photograph. All the intensity plots are in Figures 3.7 and 3.8 in which there are two graphs for each nozzle type, for 56 mbar or 25 mbar gas cell pressure. One graph is an exponential representation of the intensity and the other is linear.

In order to extract a FWHM in a consistent way from each intensity plot, the data was fitted with either a Gaussian or Lorentzian profile. The FWHM was determined by the fitting parameters. A chi-squared test was calculated for each fit to see which profile was more representative of the intensity plot, and the FWHM of the better fitting profile was taken as the gas jet diameter. It should be noted, however, that the choice of the Gaussian or Lorentzian profiles is not motivated by known physical phenomena. The choice was made due to the fact that the intensity curves were similar to or almost precisely shaped like Gaussian or Lorentzian profiles and that a FWHM would be extracted in a consistent manner.

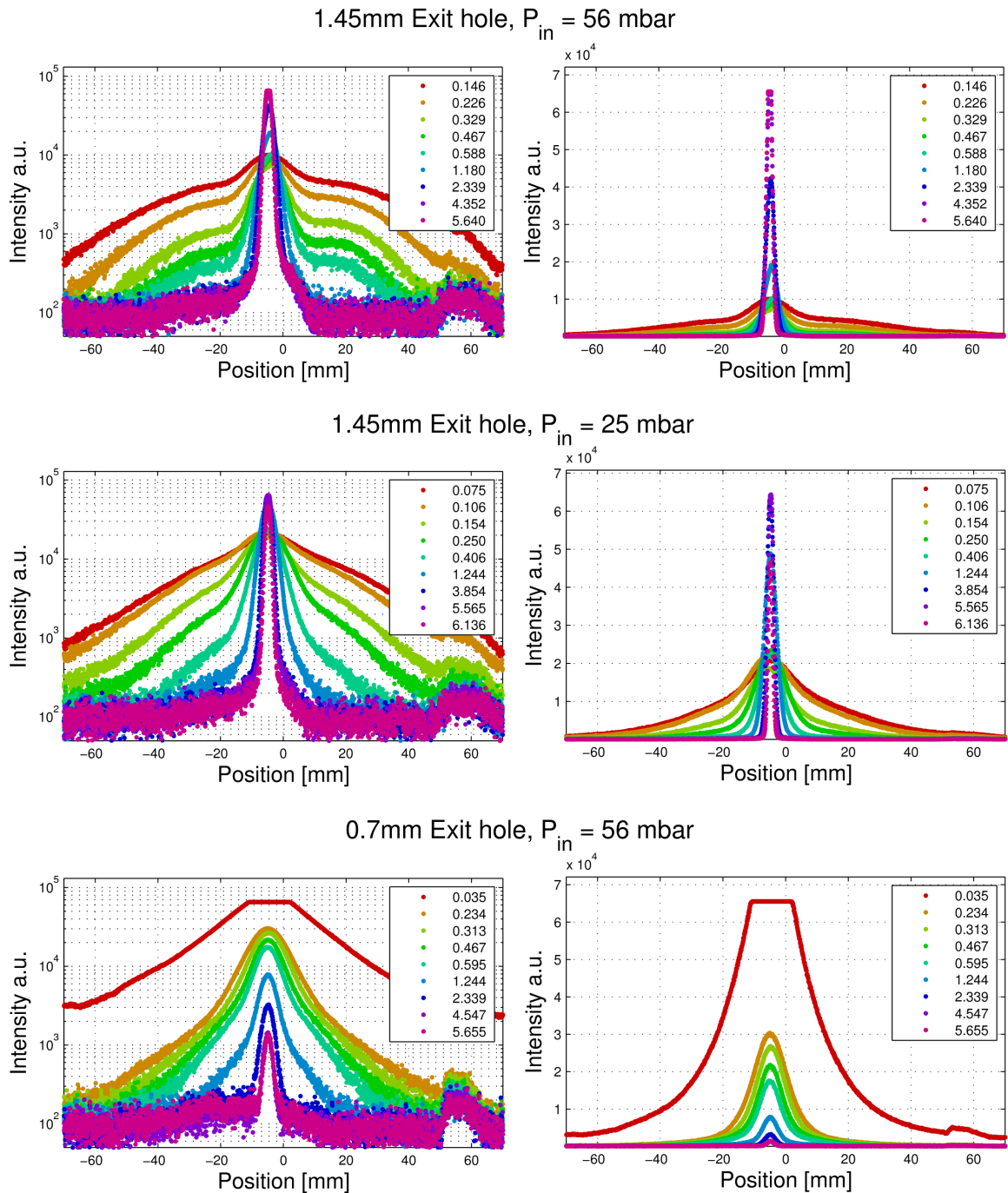


Figure 3.7: Gas jet intensities in exponential and linear formats for the 1.45 mm exit hole in 56 mbar and 25 mbar, as well as for the 0.7 mm exit hole in 56 mbar of gas cell pressure. The background pressure of each curve is labelled in the boxes.

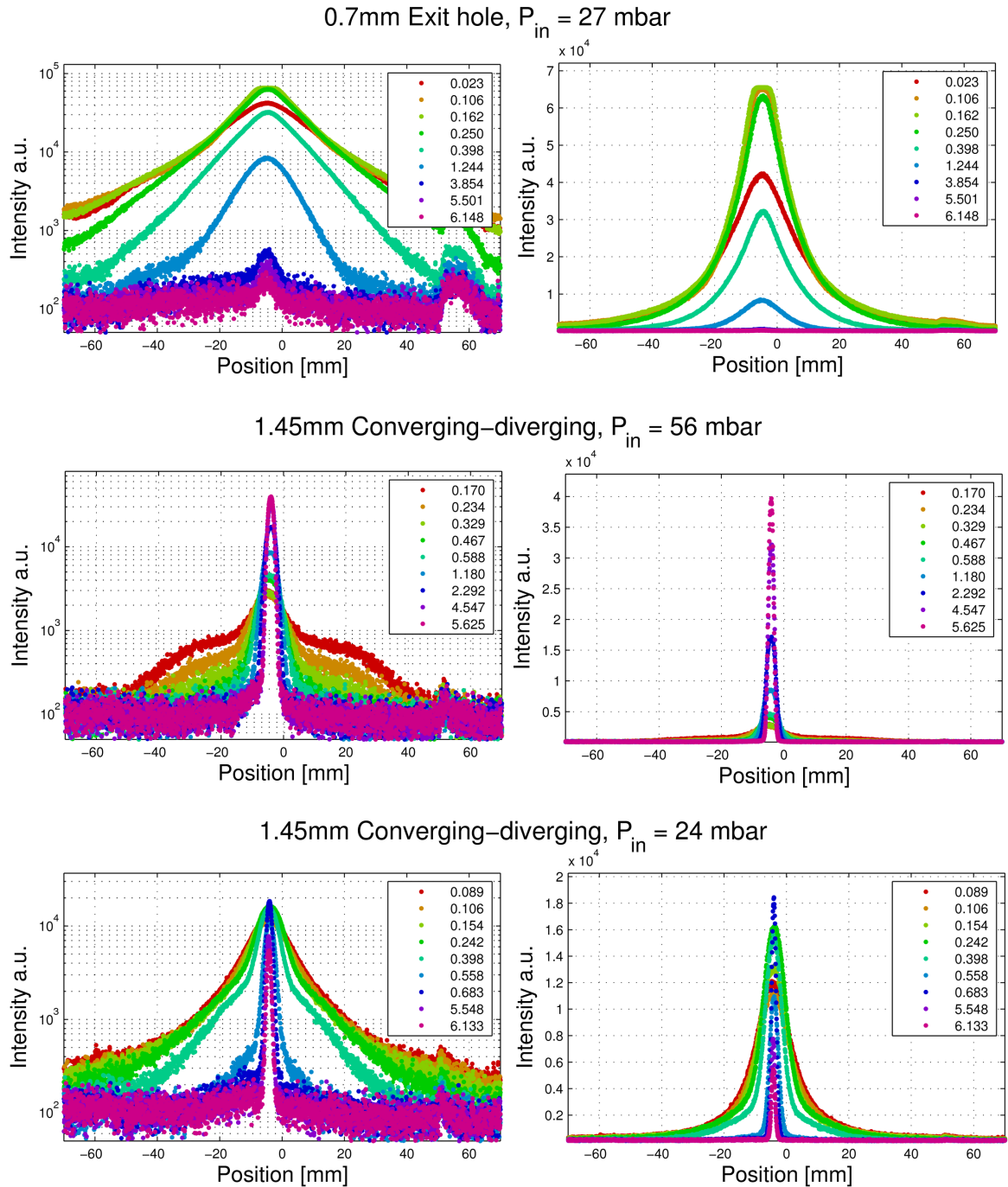


Figure 3.8: Gas jet intensities in exponential and linear formats for the 0.7 mm exit hole in 27 mbar, as well as the for the 1.45 mm converging–diverging nozzle in 56 mbar and 24 mbar of gas cell pressure. The background pressure of each curve is labelled in the boxes.

In the figures the linear plots show cases where the intensity curve seems to follow a Gaussian profile, in other cases Lorentzian profile, but also arbitrary shaped profiles. Some of the curves at low background pressures show over exposed or nearly over exposed intensities. Either these curves were not used or the over exposed part was removed before the fitting.

3.4 Discussion

3.4.1 Gas jet characteristics

Figure 3.9 shows 12 false colour photographs of gas jets emitted from a 1.45 mm exit hole and 1.45 mm converging-diverging nozzle with 56 mbar of gas cell pressure. The background pressure is labelled for every photograph. Gas jets emitting from the exit hole are on the left side, and another six gas jet on the left are from a 1.45 mm converging-diverging nozzle. The colours are cycled multiple times from black to white through several colours with increasing intensity. The resulting photographs have coloured lines representing an intensity change similar to contours on a topographic map.

Both nozzles show strongly underexpanded free jet behaviour at low background pressures (~ 0.1 mbar). By raising the background pressure the jet behaviour changes towards a slightly underexpanded regime.

Because the exit hole nozzle does not have a diverging part, it is assumed to behave like a converging-only nozzle. The strongly underexpanded free jet is evident at low background pressures by the size of the expanding jet. The gas jet adapts quickly to the background pressure which is seen as a single shock wave after the bright high density region right next to the nozzle aperture. For example, the gas jet at 0.46 mbar shows a shock wave as green spot about 1 cm away from the nozzle. The distance of the shock wave is in concordance with the Mach disc location

calculated by equation (3.10).

When the background pressure is increased the gas jet makes a transition from a strongly underexpanded jet towards a “normal” underexpanded jet. This transition is nicely seen in the photographs as the appearance of shock structures and gas jet narrowing with rising background pressure.

The jets emitted from the converging-diverging nozzle do not differ substantially from the exit hole jets. The diverging duct is relatively short in the nozzle (shown in Figure 3.3), and because of this the nozzle design may very well be behaving more like a converging-only nozzle. This would explain the similarity in the jets between the two nozzle types.

A similar kind of behaviour was also seen with the same nozzles at a gas cell pressure of 24 mbar, however the length of the fluorescing narrow jet in high background pressure conditions was shorter. The differences between the 1.45 mm exit hole and converging-diverging nozzle is not readily apparent. The 0.7 mm exit hole nozzle was harder to analyze because of the strong overexposure right after the nozzle exit. Nevertheless, none of the gas jet photographs of the 0.7 mm exit hole showed a intense narrow gas jet as seen in Figure 3.9, which is at least partly explained by the lower conductance of the smaller aperture.

The fitting of Gaussian and Lorentzian profiles followed a consistent pattern. At low pressures, in which the gas jet was not confined but was expanding and diffusing strongly, the dominant intensity profile was Lorentzian. On the other hand, at high pressures, in which the narrow confined gas jet was formed, the intensity profile showed a Gaussian shape. This is demonstrated more quantitatively in Figure 3.10 where the number of Gaussian-shaped and Lorentzian-shaped profiles are plotted in a histogram as a function of the background pressure. The plot includes all the fitted profiles.

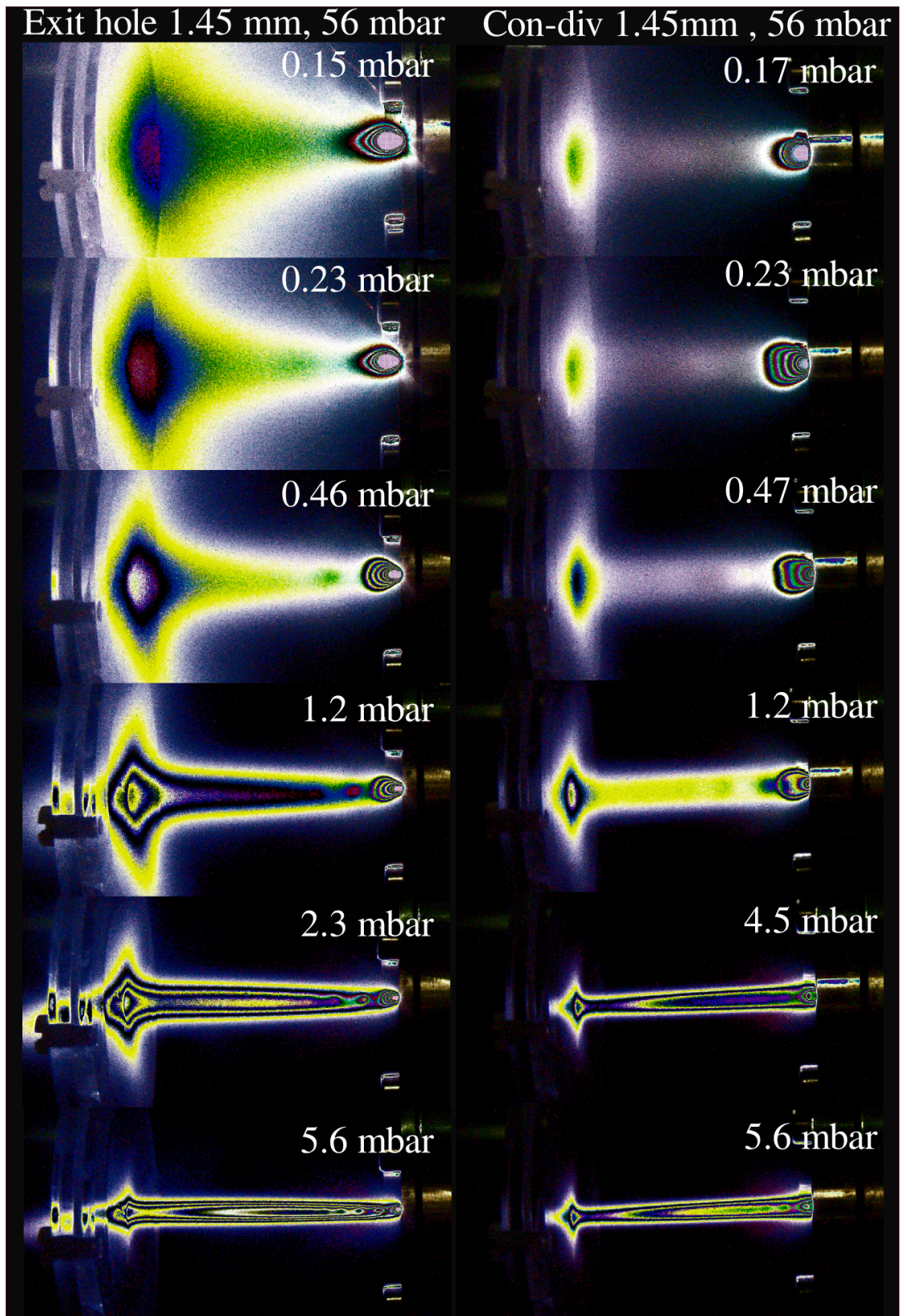


Figure 3.9: Six false colour photographs of the gas jets formed by the 1.45 mm exit-hole at left and by the 1.45 mm converging-diverging nozzle at right. The gas cell is operating at 56 mbar. The photographs show how the jet transforms from a strongly underexpanded jet towards a slightly underexpanded regime. The distance between the nozzle and the SPIG model is 3.5 cm.

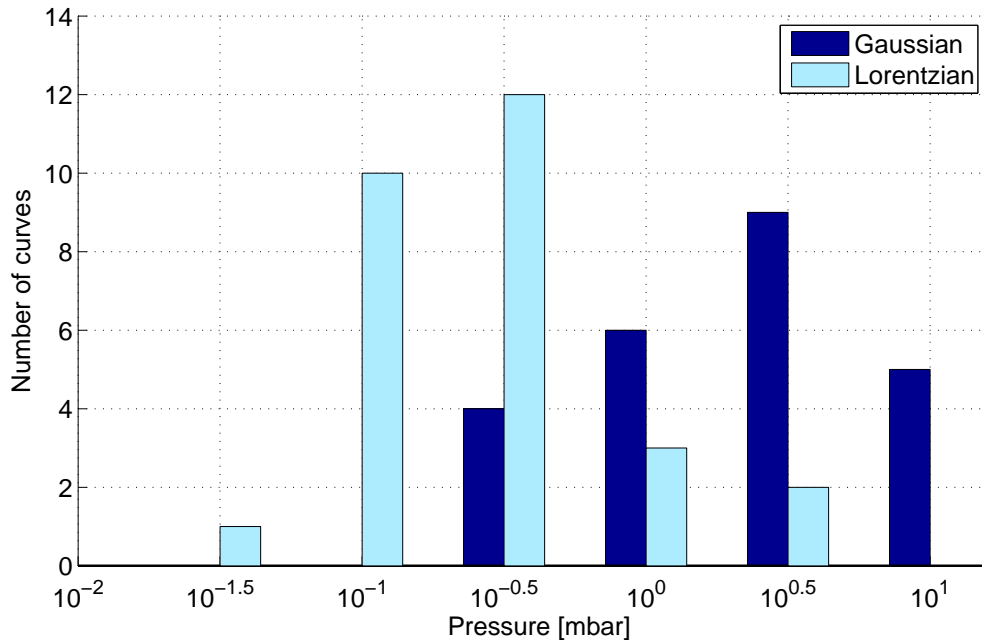


Figure 3.10: The number Gaussian like and Lorentzian like intensity profiles as a function of background pressure. Lorentzian profiles dominates at low background pressure and Gaussian at high background pressure.

3.4.2 The FWHM vs. the background pressure

Figure 3.11 shows the change in the gas jet FWHM for the three nozzle types of two gas cell pressures as a function of background pressure changing from 0.1 mbar to 7 mbar. The data for the 1.45 mm converging-diverging nozzle operated with a gas cell pressure of 24 mbar is omitted because of poor data quality. Similar to the FWHM plot of Figure 3.11, Figure 3.12 shows the peak intensity or the brightness of the gas jet fluorescence in the slice region.

With the exception of the 0.7 mm exit hole with 27 mbar gas cell pressure, the FWHM of the gas jet shows a lack of sensitivity to the nozzle type used and to the inlet pressure. The behaviour of the gas jet FWHM shows a rapid drop from about 40 mm at low background pressures (~ 0.1 mbar) to about 6 mm at 0.5 mbar of background pressure. After 0.5 mbar the increase of the background pressure up to 6

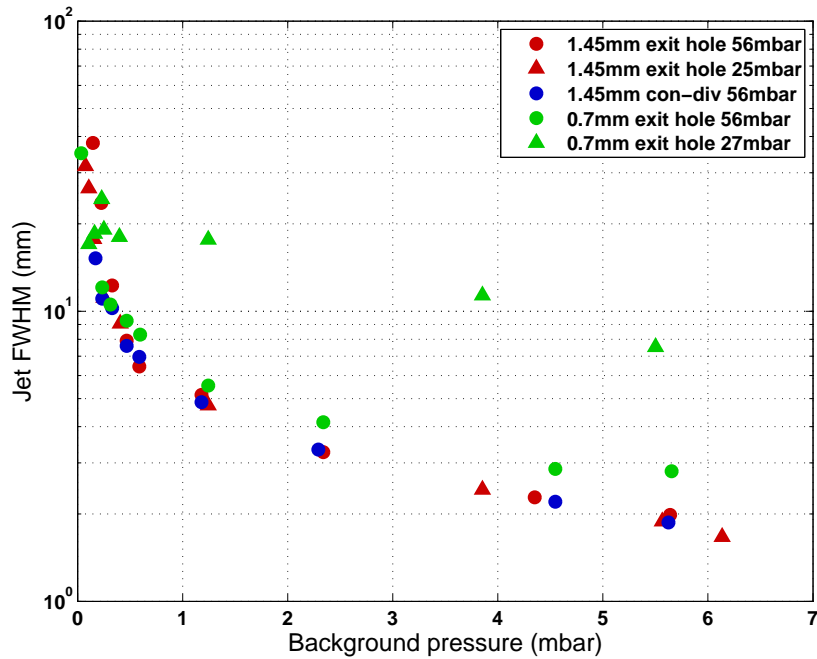


Figure 3.11: Gas jet FWHM as a function of extraction chamber background pressure for different gas cell pressures and nozzles.

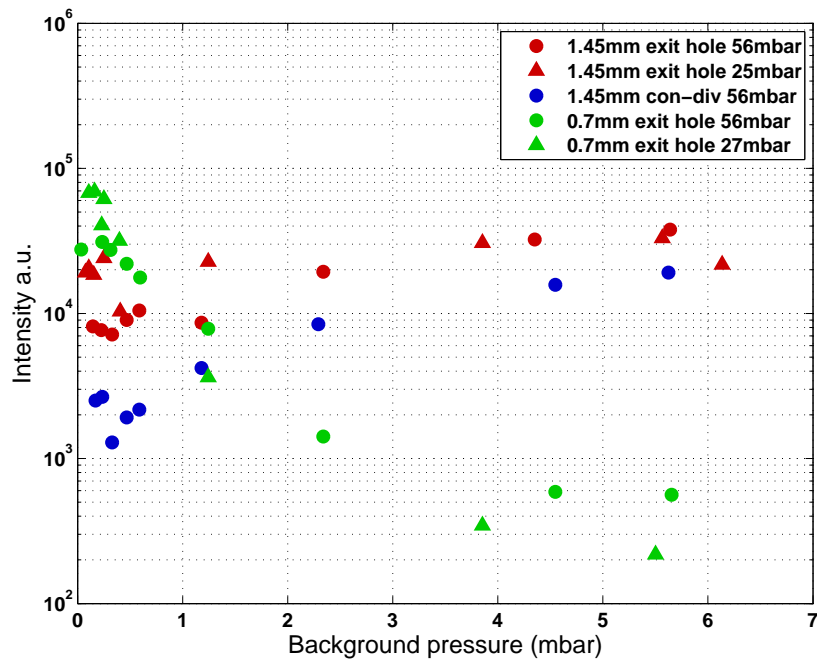


Figure 3.12: Gas jet intensity as a function of extraction chamber background pressure for different gas cell pressures and nozzles.

mbar has a slower but still gradually narrowing effect on the gas jet diameter. At 6 mbar the gas jet diameter has narrowed to 2-3 mm of FWHM. The intensity qualitatively reflects the compression of the gas jet as the background pressure increases. Firstly, the intensity drops, but as the gas jet is compressed the gas density increases and the intensity increases. This effect can be seen most strikingly in the 1.45 mm converging-diverging nozzle with 56 mbar gas cell pressure.

The 0.7 mm exit hole with 27 mbar gas cell pressure does not show the kind of rapid reduction of the gas jet diameter as seen in the other cases. The jet intensity with the 0.7 mm exit hole at both inlet pressures seems to be significantly lower than it is for the larger aperture nozzles. This is partly explained by the smaller amount of gas exiting the ion guide due to the smaller aperture size, but also the gas does not show significant narrowing at high background pressures. Rather the gas diffuses into a large volume and the intensity drops.

When background pressures are greater than 1 mbar the gas jet diameter is less than 6 mm and can couple into the SPIG without disturbances. Ideally, however, the narrowing should happen at low pressures because in practice, the higher the background pressure the increase in the probability of discharge in high electric field gradients of the SPIG.

In order to illustrate the noticeable effect of gas jet narrowing with increasing background pressure, contour maps were generated from two photographs taken at 0.2 mbar and 5.6 mbar background pressure. Before determination of the contour lines the photographs were noise-reduced by a Wiener filter provided by Matlab's Image Processing Toolbox (6.2). The noise reduction was used to soften photographs so that noise would not show up in the contour lines.

The contour maps are shown in Figure 3.13. The SPIG is visible on the left and the ion guide on the right. Contour lines are drawn in exponentially increasing intervals so that each line represents a 26% increase in brightness. The dark contour

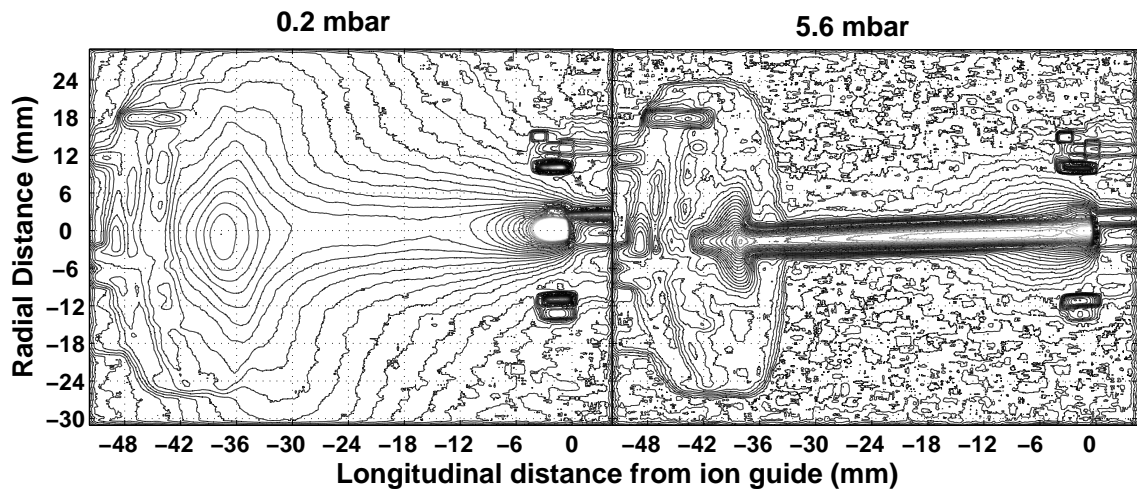


Figure 3.13: Contour maps of gas jet photographs taken at two background pressures 0.2 mbar and 5.6 mbar. The SPIG and the ion guide are visible on opposite sides of the photographs.

regions below and above the exit nozzle are connecting screws which reflect the gas jet fluorescence. The 5.6 mbar case shows the good coupling of the gas jet into the SPIG without any diffusion of the gas around the SPIG orifice. In the 0.2 mbar case the gas jet is so expanded at the SPIG that it does not enter, rather it diffuses around the SPIG orifice.

3.4.3 De Laval nozzle

A new type of nozzle was designed to tackle the problem of the need for high background pressures using the nozzles described in the previous sections. A schematic view of the new nozzle including dimensions is shown in Figure 3.14. Compared to the previously discussed converging-diverging nozzle in Figure 3.3, the distance from the nozzle throat to the nozzle exit is much longer and the curvature radius of the throat region is considerably larger. This shaping is based on designs found in literature [33,34] and has more the shape of a true converging-diverging nozzle,

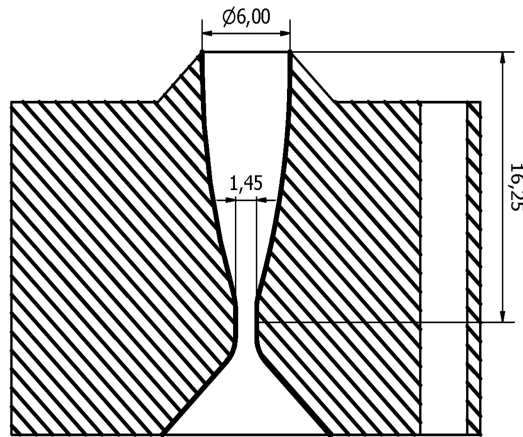


Figure 3.14: The de Laval nozzle design.

commonly called the de Laval nozzle.

The manufactured nozzle has a throat diameter of 1.45 mm and exit diameter of 6.0 mm which matches that of the SPIG repeller aperture. Using equations 3.7 and 3.8 the diameters give a design Mach number of 6.2 at the exit and thus the design pressure condition is $P_{bg}/P_{in} = 0.0014$. The nozzle was tested with argon gas using gas cell pressure of 250 mbar. This means that the background pressure should be $P_{bg} = 0.35$ mbar to satisfy the design conditions. In the test a background pressure of 0.33 mbar was realized. In Figure 3.15 a contour map of the resulting gas jet is shown, created in a similar manner as the contour maps in the previous sections. A series of underexpanded and overexpanded regions are visible along the jet, until through turbulent mixing the jet disappears suggesting that the nozzle is operating somewhat near its design condition.

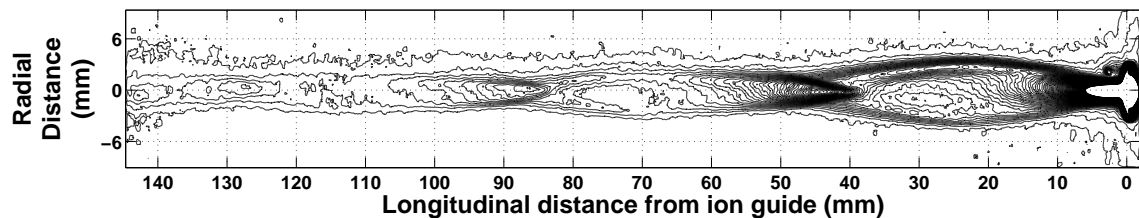


Figure 3.15: The gas jet formed by the de Laval nozzle.

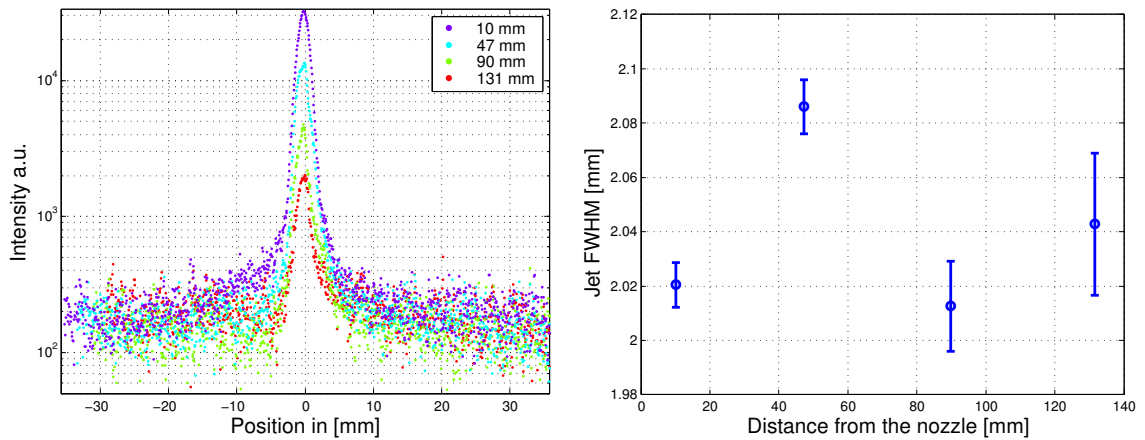


Figure 3.16: a) The intensity curves taken along the jet formed by the de Laval nozzle. The slices are positioned at the narrow boundaries between the overexpanded and underexpanded regions. b) The FWHM of the jet as a function of distance from the nozzle. The FWHM is remarkably consistent along the axis.

The most attractive feature of the jet is its narrow collimated structure. In order to investigate more quantitatively the collimation, intensity profiles were taken in the same manner as in section 3.3.5, at the boundaries of the overexpanded and underexpanded jet where the jet is the narrowest. The resulting intensity curves from the four visible boundaries are shown in Figure 3.16a. In Figure 3.16b the FWHM of the intensity curves is plotted as a function of distance from the nozzle. The jet shows a remarkably consistent width of 2.0-2.1 mm even far downstream.

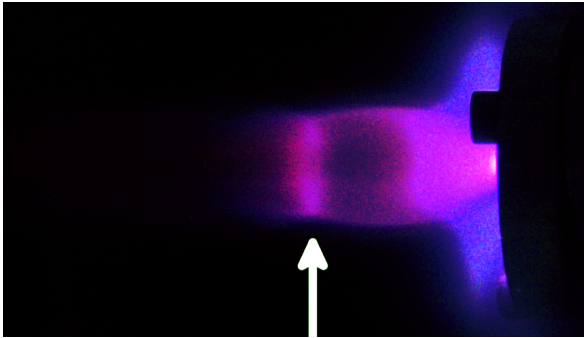


Figure 3.17: A photograph of the fluorescence of a strongly underexpanded argon jet. The Mach disc location is marked by an arrow. The oblique shocks are also clearly visible. The gas cell pressure is 300mbar.



Figure 3.18: A photograph of an underexpanded argon jet that has a lower pressure difference compared to the jet in Figure 3.17. The gas cell pressure was 50mbar. The Mach disc size has reduced and is no longer present.

3.5 The Background pressure determination by the Mach disc position

3.5.1 The background pressure determined by the Mach disc location

A series of photographs were taken of strongly underexpanded argon gas jets while varying the gas cell pressure in a similar manner as described in the jet photography of section 3.3.2. The 1.45 mm converging-diverging nozzle was attached to the gas cell filled with argon gas via the needle valve. The background pressure was measured with a TPR010 Pirani gauge located on the vacuum chamber wall. Behind the nozzle the gas cell had two spark needles to which one was raised to 700 V potential. Due to the limited size of the vacuum chamber window, the camera had to be positioned at an angle of $\sim 15^\circ$ from the perpendicular to the nozzle axis in order to photograph the full length of the gas jet.

Two examples of a total of six photographs are shown in Figures 3.17 and 3.18.

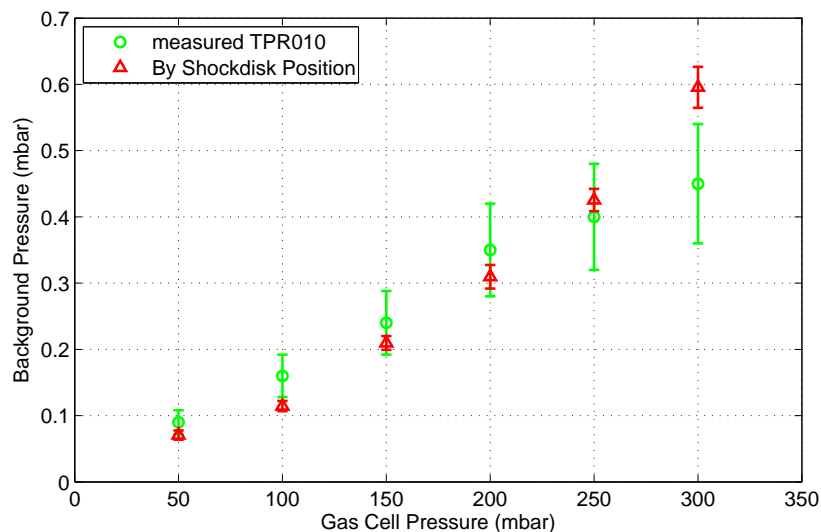


Figure 3.19: Comparison of the directly measured extraction chamber background pressure and the background pressure deduced from the Mach disc position as a function of gas cell pressure.

Both of the photographs clearly show the barrel shock structures, but only in Figure 3.17 which shows the jet extruding from the 300 mbar gas cell, a clear visible Mach disc can be seen whose position is marked by the arrow. The Mach disc is seen to move over a distance of about 7 mm away the nozzle as the pressure is reduced from 300 mbar to 100 mbar. The Mach disc size also reduces when the gas cell pressure

P_{in} mbar	x_M mm	x_{error} mm	P_{pg} mbar	$P_{bg,error}$ mbar	$P_{Machdisc}$ mbar
300	21.8	0.6	0.45	0.14	0.59
250	23.6	0.5	0.40	0.12	0.43
200	24.7	0.7	0.35	0.11	0.31
150	26.0	0.7	0.24	0.07	0.21
100	28.7	0.9	0.16	0.05	0.11
50	25.8	1.3	0.09	0.03	0.07

Table 3.1: The argon gas jet Mach disc positions and the pressure conditions in units of mbar. The column $P_{Machdisc}$ gives the pressure calculated from the Mach disc position using equation (3.10).

is reduced. In Figure 3.18 the Mach disc is barely visible as the gas jet is no longer strongly underexpanded.

The relation in equation (3.10) tells us that when the pressure ratio or the throat diameter increases the jet moves downstream from the nozzle. The Mach disc locations from the nozzle are determined by eye from the photograph. The location of the Mach disc is taken to be in the center of the higher fluorescence region after the low density region. An error in the position is also determined. The pressures and Mach disc positions are listed in table 3.1.

Using equation (3.10) the background pressure is extracted from the distance of the Mach disc to the nozzle. The extracted background pressures are compared to the directly measured background pressures. The error of the TPR010 gauge is 20% of the measured value according to the specification of the gauge. The results are shown in Figure 3.19. The pressures deduced from the Mach disc locations show excellent agreement to the measured pressures. This supports the direct background pressure measurements and the understanding of the formation of supersonic jets presented in this work.

4 Concluding remarks and outlook

The purpose of this work was to investigate the operating conditions of the IGISOL LIST method concentrating on the topics that affect the efficiency of the method. Firstly the repelling effect of the repeller electrode was studied through a series of simulations. It was investigated how a positive potential on the electrode inhibits the non-neutral fraction of the reaction products, carried by the gas jet, from entering into the SPIG. The reasons for the experimentally observed strong repelling potentials needed for a complete repulsion (an important requirement for the LIST method) have been determined. Secondly, a more efficient repelling method was studied with a transverse ion collector that needed lower repelling potentials than currently used at the IGISOL.

The simulations were able to reproduce the experimental repelling behaviour when compared against the buffer gas type and repeller electrode-gas cell distance. We were able to conclude that the continuous collisions with the gas atoms push the ions over the high potentials barriers. The transverse ion collector showed an improvement in the repelling. In particular, a suppression of the long tail was seen in the ion yield vs. repeller electrode voltage plots. The problem, however, is that the ion collector design produced strong gradients in the electric field which may lead to sparking.

In the second part of this work the efficiency of the gas jet coupling into the SPIG structure was investigated by gas jet photography and analysis. An effort was made to study the effect of different nozzle shapes and pressure conditions on the jet diameter. The jet diameter is an important parameter as it affects the geometrical overlap of the gas jet with the counterpropagating lasers, which in turn affects the

efficiency of the LIST method.

With this in mind two exit holes and one converging-diverging nozzle were studied in changing pressure environments. The analysis was done via photography of the afterglow of the gas formed inside an arc discharge ion guide, utilizing an off-line system designed for mass spectrometry. It was found that with high background pressures, the larger diameter nozzle designs, regardless of the nozzle shape and the inlet pressure, were able to produce long and narrow gas jets needed for efficient gas jet coupling into the SPIG.

The jet diameter was measured with a fitting procedure which resulted in diameters lower than 6 mm above 1 mbar of background pressure. This is required in order to couple the gas jet into the SPIG through the 6 mm aperture of the repelling electrode. The high background pressure needed to produce narrow jets was not a desired result because in practice the nozzles are always operated in a low background pressure expansion chamber. Therefore, a new type of converging-diverging nozzle, the Laval nozzle, was introduced. The analysis showed that this new type of nozzle was able to produce long and narrow jets in background pressures at least as low as 0.3 mbar.

The simulations and the gas jet study described in this thesis work contributes to the implementation of the IGISOL LIST method, which is expected to have an input on research of nuclei far from stability through an ability to produce ultra-pure radioactive ion beams. In addition, the gas jet can be utilized in optical spectroscopy because environment exhibits low pressure and temperature, which is attractive for spectroscopy as the linewidth broadening mechanisms are reduced. For example, laser spectroscopy of radioactive isotopes is planned in connection with the IGISOL LIST method in order to study nuclear charge radii. This and other future applications of the IGISOL LIST method are anticipated to play a role in the physics research at JYFL in the future.

References

- [1] J. Äystö, "Development and applications of the IGISOL technique," *Nuclear Physics A*, vol. 693, no. 1-2, pp. 477 – 494, 2001.
- [2] J. Huikari, P. Dendooven, A. Jokinen, A. Nieminen, H. Penttilä, K. Peräjärvi, A. Popov, S. Rinta-Antila, and J. Äystö, "Production of neutron deficient rare isotope beams at IGISOL; on-line and off-line studies," *Nuclear Instruments and Methods in Physics Research Section B: Beam Interactions with Materials and Atoms*, vol. 222, no. 3-4, pp. 632 – 652, 2004.
- [3] J. Ärje, J. Äystö, H. Hyvönen, P. Taskinen, V. Koponen, J. Honkanen, A. Hautojärvi, and K. Vierinen, "Submillisecond on-line mass separation of nonvolatile radioactive elements: An application of charge exchange and thermalization processes of primary recoil ions in helium," *Phys. Rev. Lett.*, vol. 54, p. 99, Jan 1985.
- [4] C. Geppert, "Laser systems for on-line laser ion sources," *Nuclear Instruments and Methods in Physics Research Section B: Beam Interactions with Materials and Atoms*, vol. 266, no. 19-20, pp. 4354 – 4361, 2008. Proceedings of the XVth International Conference on Electromagnetic Isotope Separators and Techniques Related to their Applications.
- [5] I. D. Moore, A. Nieminen, J. Billowes, P. Campbell, C. Geppert, A. Jokinen, T. Kessler, B. Marsh, H. Penttilä, S. Rinta-Antila, B. Tordoff, K. D. A. Wendt, and J. Äystö, "Development of a laser ion source at igisol," *Journal of Physics G: Nuclear and Particle Physics*, vol. 31, no. 10, p. S1499, 2005.

REFERENCES

- [6] Y. Kudryavtsev, M. Facina, M. Huyse, J. Gentens, P. V. den Bergh, and P. V. Duppen, "Beams of isotopes produced at LISOL by laser ionization after thermalization of energetic ions in a gas cell," *Nuclear Instruments and Methods in Physics Research Section B: Beam Interactions with Materials and Atoms*, vol. 204, pp. 336 – 342, 2003. 14th International Conference on Electromagnetic Isotope Separators and Techniques Related to their Applications.
- [7] C. Rauth, C. Geppert, R. Horn, J. Lassen, P. Bricault, and K. Wendt, "First laser ions at an off-line mass separator of the ISAC facility at TRIUMF," *Nuclear Instruments and Methods in Physics Research Section B: Beam Interactions with Materials and Atoms*, vol. 215, no. 1-2, pp. 268 – 277, 2004.
- [8] T. Kessler, T. Eronen, C. Mattolat, I. Moore, K. Peräjärvi, P. Ronkanen, P. Thörle, B. Tordoff, N. Trautmann, K. Wendt, K. Wies, and J. Äystö, "Upgrade to the IGISOL laser ion source towards spectroscopy on tc," *Hyperfine Interactions*, vol. 171, pp. 121–126, 2006. 10.1007/s10751-006-9496-x.
- [9] Y. Kudryavtsev, B. Bruyneel, S. Franchoo, M. Huyse, J. Gentens, K. Kruglov, W. Mueller, N. Prasad, R. Raabe, I. Reusen, P. V. den Bergh, P. V. Duppen, J. V. Roosbroeck, L. Vermeeren, and L. Weissman, "The Leuven isotope separator on-line laser ion source," *Nuclear Physics A*, vol. 701, no. 1-4, pp. 465 – 469, 2002. 5th International Conference on Radioactive Nuclear Beams.
- [10] K. Blaum, C. Geppert, H. J. Kluge, M. Mukherjee, S. Schwarz, and K. Wendt, "A novel scheme for a highly selective laser ion source," *Nuclear Instruments and Methods in Physics Research Section B: Beam Interactions with Materials and Atoms*, vol. 204, pp. 331 – 335, 2003. 14th International Conference on Electromagnetic Isotope Separators and Techniques Related to their Applications.

REFERENCES

- [11] I. D. Moore, J. Billowes, P. Campbell, T. Eronen, C. Geppert, A. Jokinen, P. Karvonen, T. Kessler, B. Marsch, A. Nieminen, H. Penttilä, S. Rinta-Antila, T. Sonoda, B. Tordoff, K. Wendt, and J. Äystö, "Laser ion source development at IGISOL," in *Nuclear Structure, Astrophysics, and Reactions*, vol. 831, pp. 511 – 513, Meville, New York, 2005.
- [12] T. Sonoda, "The laser ion source trap (LIST) soupled to a gas cell catcher," *Nucl. Instrum. Methods Phys Res.*, vol. 267, p. 2918, 2009.
- [13] P. Karvonen, T. Sonoda, I. D. Moore, J. Billowes, A. Jokinen, T. Kessler, H. Penttilae, A. Popov, B. Tordoff, and J. Aysto, "LIST developments at IGISOL," *EUROPEAN PHYSICAL JOURNAL-SPECIAL TOPICS*, vol. 150, pp. 283–284, NOV 2007.
- [14] T. Kessler, *Development and application of laser technologies at radioactive ion beam facilities*. PhD thesis, University of Jyväskylä, 2008.
- [15] B. A. Marsh, *In-Source Laser Resonance Ionization at ISOL Facilities*. PhD thesis, Shool of Physics and Astronomy, 2007.
- [16] H. XU, M. WADA, J. TANAKA, H. KAWAKAMI, I. KATAYAMA, and S. OHTANI, "A new cooling and focusing device for ion guide," *NUCLEAR INSTRUMENTS & METHODS IN PHYSICS RESEARCH SECTION A-ACCELERATORS SPECTROMETERS DETECTORS AND ASSOCIATED EQUIPMENT*, vol. 333, pp. 274–281, SEP 1 1993.
- [17] P. V. den Bergh, S. Franchoo, J. Gentens, M. Huyse, Y. Kudryavtsev, A. Piechaczek, R. Raabe, I. Reusen, P. V. Duppen, L. Vermeeren, and A. Wöhr, "The SPIG, improvement of the efficiency and beam quality of an ion-guide based on-line isotope separator," *Nuclear Instruments and Methods in Physics Research Section B: Beam Interactions with Materials and Atoms*, vol. 126, no. 1-4,

REFERENCES

- pp. 194 – 197, 1997. International Conference on Electromagnetic Isotope Separators and Techniques Related to Their Applications.
- [18] P. Karvonen, I. Moore, T. Sonoda, T. Kessler, H. Penttilä, K. Peräjärvi, P. Ronkainen, and J. Äystö, “A sextupole ion beam guide to improve the efficiency and beam quality at IGISOL,” *Nuclear Instruments and Methods in Physics Research Section B: Beam Interactions with Materials and Atoms*, vol. 266, no. 21, pp. 4794 – 4807, 2008.
- [19] S. I. S. Inc., *Simion 8.0*. 1027 Old York Rd. Ringoes NJ.
- [20] D. A. Dahl, “Simion for the personal computer in reflection,” *International Journal of Mass Spectrometry*, vol. 200, no. 1-3, pp. 3 – 25, 2000.
- [21] D. J. Manura, “Additional notes on the simion hs1 collision model,” tech. rep., Scientific Instruments Services Inc., Feb. 2007.
- [22] A. Bondi, “van der waals volumes and radii,” *The Journal of Physical Chemistry*, vol. 68, no. 3, pp. 441–451, 1964.
- [23] Y. Kudryavtsev, T. Cocolios, J. Gentens, M. Huyse, O. Ivanov, D. Pauwels, T. Sonoda, P. V. den Bergh, and P. V. Duppen, “Dual chamber laser ion source at LISOL,” *Nuclear Instruments and Methods in Physics Research Section B: Beam Interactions with Materials and Atoms*, vol. 267, no. 17, pp. 2908 – 2917, 2009.
- [24] M. Reponen, I. Moore, I. Pohjalainen, T. Kessler, P. Karvonen, J. Kurpeta, B. M. b, S. Piszczek, V. Sonnenschein, and J. Äystö, “Gas jet studies towards an optimization of the IGISOL LIST method,” *nimb (submitted)*, 2010.
- [25] M. Rasi, R. Saintola, and K. Valli, “Visualizing the expanding flow of gas from helium-jet and ion-guide nozzles,” *Nuclear Instruments and Methods in Physics*

REFERENCES

- Research Section A: Accelerators, Spectrometers, Detectors and Associated Equipment*, vol. 378, no. 1-2, pp. 251 – 257, 1996.
- [26] R. D. Zucker and O. Biblarz, *Fundamentals of Gas Dynamics*. Hoboken, New Jersey: John Wiley & Sons, Inc., 2002.
- [27] G. Sanna, *Introduction to molecular beams gas dynamics*. London : Imperial College Press ; Hackensack, NJ : Distributed by World Scientific, 2005.
- [28] H. Ashkenas and C. K. Sherman, "Rarefied gas dynamics," in *4th Symposium* (J. de Leeuw, ed.), vol. 2, Academic Press New York, 1966.
- [29] I. D. Moore, T. Kessler, T. Sonoda, Y. Kudryavstev, K. Peräjärvi, A. Popov, K. D. A. Wendt, and J. Äystö, "A study of on-line gas cell processes at IGISOL," *Nuclear Instruments and Methods in Physics Research Section B: Beam Interactions with Materials and Atoms*, vol. 268, no. 6, pp. 657 – 670, 2010.
- [30] A. Bogaerts and R. Gijbels, "Modeling of metastable argon atoms in a direct-current glow discharge," *Phys. Rev. A*, vol. 52, pp. 3743–3751, Nov 1995.
- [31] A. V. Phelps and J. P. Molnar, "Lifetimes of metastable states of noble gases," *Phys. Rev.*, vol. 89, pp. 1202–1208, Mar 1953.
- [32] T. M. Inc, *Matlab R2008B*. Natick, MA 01760-2098, USA, 2008.
- [33] V. A. Soukhanovskii, H. W. Kugel, R. Kaita, R. Majeski, and A. L. Roquemore, "Supersonic gas injector for fueling and diagnostic applications on the national spherical torus experiment," *Review of Scientific Instruments*, vol. 75, no. 10, pp. 4320–4323, 2004.
- [34] G. Dupeyrat, J. B. Marquette, and B. R. Rowe, "Design and testing of axisymmetric nozzles for ion-molecule reaction studies between 20k and 160k," *Physics of Fluids*, vol. 28, no. 5, pp. 1273–1279, 1985.

Appendices

**IGISOL offline-laitteiston
optimointi ja mallintaminen
SIMION-simulointiohjelmistolla**

Erikoistyö

Ilkka Pohjalainen

JYVÄSKYLÄN YLIOPISTO
28. Kesäkuuta 2010

1 Johdanto

Tässä työssä tarkoituksena on simuloida ionioptista offline-laitteistoa, jossa voidaan testata ja optimoida IGISOL [1] olosuhteita sekä suorittaa esimerkiksi ionisaatiospektroskopisia mittauksia. Offline-laitteisto pääpiirteissään koostuu ionilähteestä, ionioptiikasta ja kvadrupolimassaspektrometristä (QMS). Ionilähteessä muodostetut ionit kuljetetaan mahdollisimman pienellä häviöllä massaspektrometriin, jossa ionilajit tunnistetaan massan perusteella.

Offline-laitteiston ionilähteessä muodostetut ionit kuljetetaan ulos taustakaasun virtauksella, joka muodostetaan pitämällä ionilähde korkeassa paineessa. Korkean paineen takia ongelmaksi on muodostunut liian suuri tyhjiökammion paine QMS:ssään alueella. Siksi nykyiseen offline-laitteistoon rakennetaan uudella diffuusiotyhiöpumpulla varustettu jatkokappale. Jatkokappaleeseen asennetaan myös Einzel-linssisysteemi, jonka tarkoituksena on ohjata ionien kulku laitteiston läpi ja maksimoida QMS:ään saapuvien ionien määrä.

Laitteistoa on simuloitu SIMION-simulointiohjelmistolla. Simuloinnin tarkoituksena on löytää offline-laitteiston optimaalisin rakenne, ja linssisysteemien ja laitteiston eri osien sähköiset potentiaalit, sekä toisaalta tutkia ionien käyttäytymistä. Lisäksi SIMION-ohjelmistolla toteutettiin kvadrupolimassaspektrometrin mallintaminen.

Perusionioptinen simulointi on toteutettu SIMION-ohjelmiston mukana tulevilla työkaluilla. Koska kaasuvirtauksen ja paineen vaikutukset ionien liikeratoihin on otettava huomioon, eikä SIMION-ohjelmistossa ole sisäänrakennettua taustakaasun mallinnusta, on SIMION-ohjelmiston itseohjelmoitavilla käyttäjäohjelmilla toteutettu kaasumallin simulaatiot. Kaasumallin toteutus on kaksiosainen. Ionien vuorovaikutusta taustakaasun kanssa on mallinnettu kovan pallon törmäysmallilla. Taustakaasun virtausta on simuloitu räjähdysmallilla.

2 Simulaatio ympäristö

2.1 SIMION-simulointiohjelmisto

Simulaatioympäristönä käytettiin Win32-alustalla ajettavaa SIMION 8.0 ohjelmistoa, jolla voidaan mallintaa ionioptiikkaa simuloimalla ionien liikettä sähköstaattisissa ja magneettisissa potentiaaleissa. SIMION-ohjelmiston sisäänrakennetut simulaatiotyökalut ja käyttäjän itseohjelmoitavat käyttäjäohjelmat mahdollistavat monimutkaistenkin ionioptisten laitteiden si-

muloinnin. [2]

Simuloitava systeemi määritellään sähköstaattisiin ja magneettisiin potentiaalimatriiseihin, jotka voivat olla joko kolmiulotteisia epäsymmetrisiä matriiseja tai kaksiulotteisia symmetrisiä matriiseja. Kaksiulotteisista matriiseista muodostetaan kolmiulotteinen avaruus joko tasosymmetrisesti tai pyörähdyssymmetrisesti. Lisäksi piirretty systeemi voidaan vielä peilata tasojen suhteen. Potentiaalimatriisilla tarkoitetaan kolmiulotteista diskreettiä hila-avaruutta, jossa jokainen hilapiste kuvaa joko tyhjää tilaa tai elektrodia omassa potentiaalissaan.

Käytännössä potentiaalimatriisit määritellään GEM-geometriatiedostossa, jossa kussakin potentiaalissa olevat elektrodit määritellään erikseen käyttäen eri perusgeometrisiä kuviota. Koska offline-laitteistossa ei käytetä magneetteja ionioptiikassa, tässä työssä käsitellään vain SIMION-ohjelmiston sähköstaattisia kenttiä.

SIMION ratkaisee Laplacen yhtälön potentiaalimatriiseille relaksaatiomenetelmällä, jota nopeutetaan ylirelaksaatio- ja pisteen hienustusmenetelmillä (skipped point refining). [2,3] Laplacen yhtälön ratkaisun jälkeen elektrodien potentiaalia on helppo muuttaa nopealla jännitesäädöllä.

2.2 Simuloinnin kulku

Ennen ionien lennättämistä määritetään ionien määrä, alkupaikat ja -nopeudet sekä ominaisuudet kuten varaus ja massa. Lennättämisen aikana simuloinnin kulku pääpiirteissään tapahtuu laskemalla jokaiselle ionille erikseen aika-askeleen pituus. Tämän jälkeen ioneja siirretään aika-askeleen verran eteenpäin. Ionin uudessa paikassa lasketaan ioniin kohdistuvat voimat sekä mahdollinen avaruusvarauksen huomioon ottava ionirepulsio. Näistä saadaan ionin kiihtyvyys. Uuden kiihtyvyyden laskemisen jälkeen palataan takaisin siirtämään ionia aika-askeleen verran.

Kunkin ionin siirrossa tämän uusi paikka lasketaan ionin nopeudesta ja kiihtyvyydestä numeerisesti Runge-Kutta-integrointimenetelmillä. Aika-askeleen kokoa päivitetään tietyin väliajoin joko pienemmäksi, jotta ionien liikeradat tarkentuisivat, tai suuremmaksi, jotta simuloinnin suoritus aika lyhenisi. Hyvään tarkkuuteen vaadittava aika-askeleen pituus riippuu sähköstaattisen kentän jyrkkyydestä, ja mahdollisesta varausrepulsiosta

Simuloinnin eri osien suorituksen aikana SIMION kutsuu käyttäjäohjelmassa mahdollisesti määritettyjä kuhunkin simuloinnin osaan oleellisesti liittyviä funktioita. Näillä funktiolla on mahdollista lukea ja muuttaa simuloinnin eri muuttujia, kuten ionien paikkoja, nopeuksia, kiihtyvyyksiä, tai elektrodien jännitteitä. Rajapintakielenä käytetään LUA-skriptikieltä [4], joka on

helppo ja mukautuva ohjelmointikieli, ja toisaalta myös verrattain nopea. Offline-laitteiston simulointiin ohjelmoitu käyttäjäohjelma on kokonaisuudessaan liitteessä A. Käyttäjäohjelmassa käytetyt funktiot ja muuttujat on yksityiskohtaisesti selitetty viitteessä [2].

3 Offline-laitteiston kuvaus simulointiympäristöön

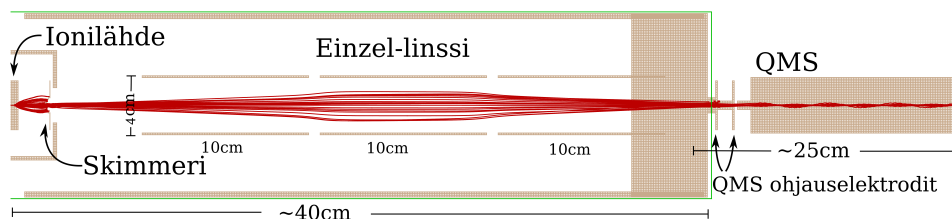
3.1 Offline-laitteisto

Offline-laitteiston lopullinen toteutus ja mitat eivät olleet simuloinnin suorittamisen aikana tarkasti tiedossa, joten tässä työssä esitetty malli ei välttämättä ole lopullinen toteutus. Kuitenkin laitteiston olennaiset osat ja mittasuhteet tiedetään riittävällä tarkkuudella. Laitteisto voidaan jakaa pääpiirteissään ionilähteen ja skimmerin alueeseen, Einzel-linssisysteemiin sekä QMS:ään.

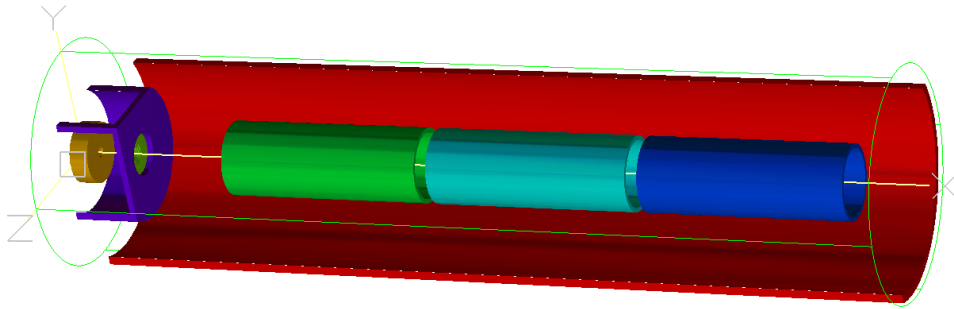
Offline-laitteiston yksi mahdollinen malli on kuvattu kokonaisuudessaan kuvassa 1, johon merkattu tärkeimmät laitteiston mittasuhteet sekä piirretty koessimulaation ionien radat punaisella. Kuvan ionien radoissa on nähtävissä QMS:lle tyyppilliset oskilloivat ioniradat.

Laitteiston ionilähteenä käytetään esimerkiksi kipinälähdettä, jossa ioneja synnytetään taustakaasuun sähköpurkausten avulla. Korkeapaineinen taustakaasu virtaa suuttimen läpi tyhjiökammioon, jolloin muodostuu ioneja sisältävä kaasusuihku. Ioneja sisältävästä kaasusuihkusta eritellään hyvin kollimoitunut ionisuihku skimmerillä, jossa on 1mm halkaisijaltaan oleva reikä, mikä jälkeen ioni suihku ohjataan edelleen Einzel-linssin läpi QMS:ään. Ionilähteen ja skimmerin väliin muodostetaan ioneja kiihdyttävä sähkökenttä kytkemällä ionilähde jännitteeseen.

Einzel-linssisysteemi koostuu kolmesta erillisestä sylinterin muotoisesta elektrodista, joiden potentiaalit ovat erikseen määriteltävissä. Einzel-linssisysteemillä ionisuihku kohdistetaan QMS:ään, joka puolestaan koostuu edessä olevasta kahdesta fokusoivasta elektrodista ja itse kvadrupolikammioista, jossa sen neljä elektrodisauvaa ovat optisen akselin ympärillä.



Kuva 1: Offline-laitteisto kokonaisuudessaan SIMION-ohjelmiston kuvassa.



Kuva 2: Ionilähde, skimmeri ja Einzel-linssisysteemi. Tyhjiökammion reuna on kuvattu punaisella.

Jotta ionit lentävät koko laitteiston läpi, systeemiin on muodostettava globaalisti aleneva sähköpotentiaali. Paikallisesti potentiaali voi nousta, kunhan ioneilla on riittävästi liike-energiaa ylittää potentiaalivalli.

3.2 Offline-laitteiston kuvaaminen SIMION-ohjelmistossa

Koska ionilähde, skimmeri ja Einzel-linssisysteemi ovat symmetrisiä optisen akselin suhteen, ne on piirretty simulaatioon kaksiulotteisella mallilla, jonka pyörähdyskappale kuvaa systeemin kolmiulotteisena. Näin saavutetaan nopeampi Laplacen yhtälön ratkaisu ja avaruudellisesti tarkempi malli systeemin osista. Kuvassa 2 on piirrettyä kyseisistä osista muodostuvan systeemin halkileikkaus.

QMS on pitänyt puolestaan piirtää suoraan kolmiulotteisena mallina, koska QMS:ään sauvat ovat optisen akselin suuntaisesti optisen akselin ympärillä, eikä systeemi ole täten sylinterisymmetrinen. Kuvassa 3 on piirretty QMS:ään halkileikkaus.

Simuloitavaan systeemiin on myös kuvattu skimmerin alustalieriö ja tyhjiökammion ulkoreuna, joiden vaikutus sähkökenttiin on otettava huomioon. Skimmerin ja Einzel-linssisysteemin väliin on jätetty noin 5cm väli, jotta siihen on mahdollista lisätä kammioiden välinen venttiili.

Ionilähde on piirretty simulaatiosysteemiin, niin että siinä on millimetrin halkaisijalla oleva aukko, joka avautuu puolipallonmuotoisen suuttimeen. Tämän on tarkoitus suurpiirteisesti mallintaa ionilähteessä useasti käytettävän kaksoiskartion muotoisen suuttimen aukkoa. Ionit muodostetaan reiän sisälle, josta kaasumallin kaasuvirtaus vie ionit kiihdyttävään sähköpotentiaaliin, ja tästä edelleen skimmerin läpi Einzel-linssisysteemiin.

QMS:ään kuuluu kaksi sen edessä olevaa ohjauselektrodia ja kvadrupolikammio, jossa neljä halkaisijaltaan noin 8mm kvadrupolisauvaa sijaitsevat symmetrisesti optisen akselin ympärillä. Kuvan 3 QMS:ään poikkileikkauk-

sessä on näkyvissä kolme näistä sauvoista.

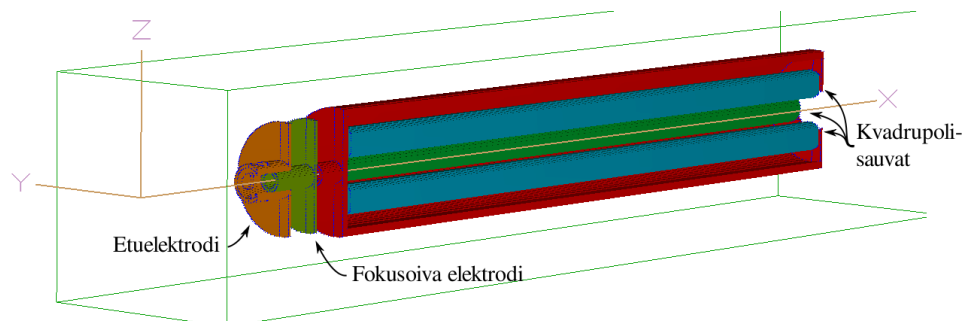
4 Kaasumalli

4.1 Kovan pallon törmäysmalli

Ionilähteen korkean paineen avulla synnytyssä kaasusuihkussa on kaasun paine niin korkea, että ionien keskimääräinen vapaa matka on lyhyt, eikä yhtä ionia voida ajatella vapaana hiukkasena. SIMION-ohjelmisto olettaa lähtökohtaisesti kaikki ionit vapaiksi hiukkasiksi, joten korkeapaineinen kaasu on täytynyt ottaa huomioon kovan pallon törmäysmallilla ja räjähdysmallilla. Kovan pallon törmäysmallilla mallinnetaan taustakaasun atomien törmäyksiä ioneihin ja räjähdysmallilla sen sijaan mallinnetaan taustakaasun virtausta.

Toteutettu kovanpallon törmäysmalli on edelleen kehitetty SIMION-ohjelmiston esimerkistä [5] ja perustuu kineettiseen kaasuteoriaan. Siinä mallinnettava ioni kulkee neutraalissa taustakaasussa, yleensä joko heliumissa tai argonissa, törmää taustakaasun atomiin ja siroaa elastisesti. Kaasun atomit kaasuteoriassa liikkuvat satunnaisesti suuntiin, niin että nopeusjakauma noudattaa Maxwell-Boltzmannin jakaumaa, eli taustakaasun atomien nopeuksien kukin avaruuskomponentit noudattavat Gaussista jakaumaa, jonka varianssi on $k_B T/m$.

Pelkästään sähköstaattisessa ionioptiikassa ionien massa ei vaikuta mallinnettuihin ionien ratoihin. Kaasumalli aiheuttaa kuitenkin massariippuvuuden ionien kulkuun, koska taustakaasun atomin törmäyksen vaikutus on kevyempään ioniin suurempi kuin suuren liikemäärän omaavaan painavampaan kaasuioniin. Tästä syystä simulaatiot on yleensä toistettu yhdellä kevyellä ionilla, kuten natriumionilla, ja yhdellä raskaalla, kuten toriumionilla.



Kuva 3: Kvadrupolimassaspektrometrin poikkileikkaus.

Ionin liikkeessa matkan $\Delta s = v_i \Delta t$ taustakaasussa se läpäisee taustakaasun törmäyksettä todennäköisyydellä.

$$P_{\text{ei törmäystä}} = e^{-\frac{\Delta s}{\lambda}} = e^{-\frac{v_i \Delta t}{\lambda}}, \quad (1)$$

jossa keskimääräistä vapaata matkaa kuvaa λ . Edelle olevan kaavan (1) mukaan on lähdekoodissa riveillä 525-534 laskettu törmäyksen todennäköisyys, jokaisen ionin liikkeessa aika-askeleen Δt eteenpäin.

Keskimääräinen vapaata matka λ voidaan ilmaista keskimääräisen törmäystaajuuden avulla $f_c = v_i/\lambda$, joka edelleen voidaan ilmaista törmäyksen vaikutusalan σ , ionin keskimääräisen suhteellisen nopeuden v_r ja taustakaasun hiukkastiheyden n_g avulla. [5]

$$f_c = \sigma v_r n_g, \quad (2)$$

Keskimääräinen suhteellinen nopeus tarkoittaa tässä ionin keskimääräistä nopeutta kaasuun verrattuna, eli

$$v_r = \int_V |\mathbf{v}_i - \mathbf{v}_g| f(\mathbf{v}_g) d\mathbf{v}_g, \quad (3)$$

jossa siis $f(\mathbf{v}_g)$ on Gaussinen jakauma varianssilla $k_B T/m$. Viitteessä [5] on suoraviivaisella laskulla osoitettu, että

$$v_r = \frac{\langle v_g \rangle}{2} \left(\left(s + \frac{1}{2s} \right) \pi \operatorname{erf}(s) + e^{-s^2} \right), \quad (4)$$

jossa $\langle v_g \rangle = \sqrt{8kT/\pi m}$ ja $s = v_i \sqrt{m/2kT}$.

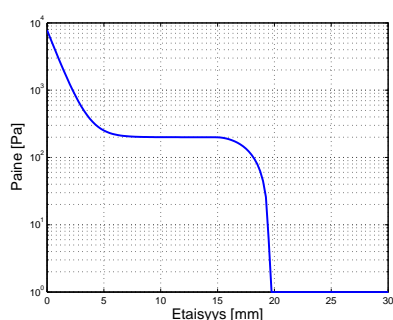
Kaavan (2) vaikutusala σ lasketaan törmäyvän ionin ja taustakaasun atomin van der Waalsin säteiden r_i ja r_g avulla seuraavasti

$$\sigma = \pi (r_i + r_g)^2. \quad (5)$$

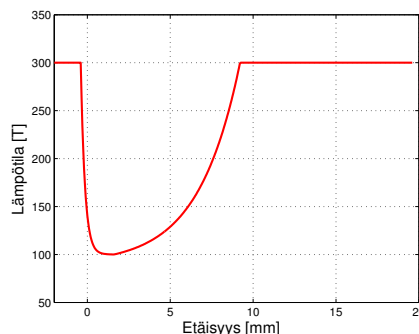
Kaikki tässä työssä esiintyvät simulaatiot on tehty heliumtaustakaasulla, jossa $r_g = 140\text{pm}$.

Kaavan (2) hiukkastiheys n_g lasketaan yksinkertaisesti ideaalikaasulaista, kun kaasun paine P ja lämpötila T tunnetaan ionin liikkeen kohdalla. Kun paine, lämpötila, vaikutusala ja keskimääräinen suhteellinen nopeus tiedetään, voidaan keskimääräinen vapaa matka laskea ja tästä edelleen törmäyksen todennäköisyys. Edellä kuvattu laskenta keskimääräisen vapaan matkan λ määrittämiseksi on toteutettu lähdekoodissa riveillä 485-518.

Kun törmäys tapahtuu, taustakaasun atomin nopeuden komponenteille



(a) painefunktio



(b) lämpötilafunktio

Kuva 4: Simuloinnissa käytetyt paine- ja lämpötilafunktioiden kuvaajat. Paine ja lämpötila muuttuvat kuvaajien mukaisesti pallosymmetrisesti suuttimen katsoen.

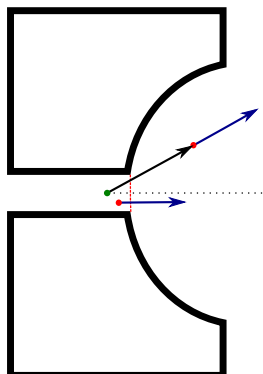
asetetaan arvot Gaussisen jakauman mukaisesti. Tämän jälkeen siirrytään koordinaatistoon, jossa taustakaasun atomi on paikallaan, ja lasketaan ionin uusi nopeus satunnaisella törmäyskulmalla ja -parametrilla käyttäen elastisen törmäyksen kinematiikkaa. Katso ohjelmakoodin rivit 552-620.

4.2 paine- ja lämpötila mallit

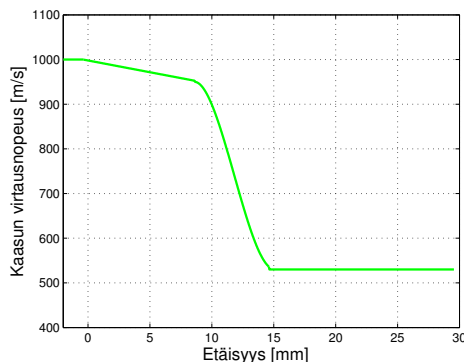
Ongelmaksi kuitenkin muodostuu, että kaasun paine ja lämpötila on tunnettava välittömästi ionilähteen suuttimen jälkeen. Paineita ja lämpötilaa on arvioitu aiemmilla CosmosFlowWorks2006 [6] simulaatioilla. Paineen käyttäytymistä on lisäksi arvioitu offline-laitteistoa vastaavanlaisessa systeemissä tehdyillä kaasusuihkujen paineen neulamittauksilla. [7]

Paineen on oletettu muuttuvan pallosymmetrisesti etäisyyden funktiona suuttimen aukosta katsottuna, ja paineen tippuvan eksponentiaalisesti ja saturoituvan noin 1 mbar:iin varsin nopeasti. Skimmerin jälkeen paine laskee niin alas, ettei törmäyksiä enää tapahdu, ja ioneja voidaan tämän jälkeen pitää vapaina hiukkasina. Kuvassa 4a on simulaatioissa käytetyn painefunktion kuvaaja, joka kertoo paineen tippumisen suuttimen ja ionin välisen etäisyyden funktiona. Ohjelmalle annetaan ionilähteen paineen arvo ja painefunktio skaalataan niin, että paineen maksimi arvo vastaa annettua paineen arvoa. Lähdekoodissa funktio riveillä 143-169 antaa paineen arvon kunkin ionin kohdalla ionilähteen paineen ja ionin ja suuttimen välisen etäisyyden avulla.

Koska kaasusuihku laajenee adiabaattisesti välittömästi suuttimesta poistuessa, sen lämpötilan odotetaan jäähtyvän nopeasti huoneenlämmöstä noin 100K asteeseen ja sen jälkeen lämpenevän takaisin huoneenlämpöön. Simu-



Kuva 5: Räjähdyksmallin toimintaperiaate. Ioni tuntee kaasuvirtauksen tulevan suuttimen aukosta.



Kuva 6: Kaasuvirtauksen suuruus ionilähteen ja suuttimen välisen etäisyyden funktiona

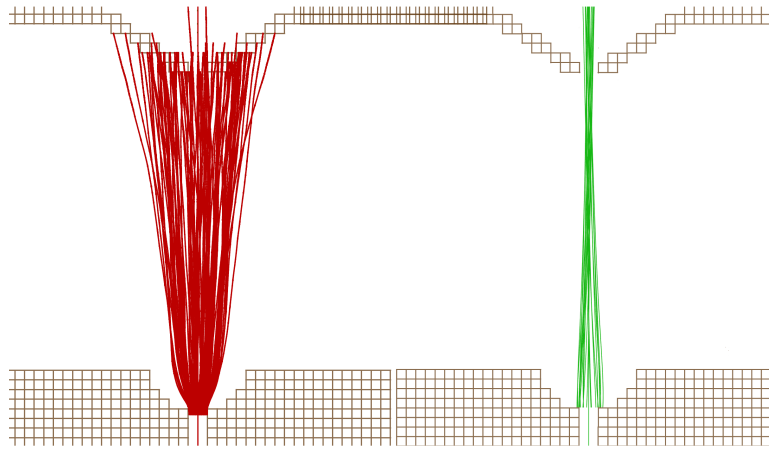
laatioihin perustuen kaasun lämpötilan on oletettu käyttäytyvän kutakuinkin kuvaajan 4b mukaisesti. Lähdekoodissa funktio riveillä 196-223 antaa lämpötilan paikan funktiona.

4.3 Räjähdyksmalli

Suuttimesta tulevan puskurikaasun virtausta on mallinnettu yksinkertaisella räjähdysmallilla, jota on käytetty aiemmassa samankaltaisessa simulaatiossa. [8] Tässä mallissa taustakaasuvirtauksen suunta tietyn ionin kohdalla määräytyy kyseisen ionin etäisyydestä sekä suuttimeen että optiseen akseliin.

Kuvassa 5 on räjähdysmallin toimintaperiaate kuvattu yksinkertaisella piirroksella. Kuvassa on optinen akseli mustalla katkoviivalla, jossa räjähdysmallin vertauspiste on vihreällä. Punainen viiva kuvaa rajaa, josta suutin alkaa avautua ja jonka jälkeen kaasuvirtauksen suunta määräytyy vertauspisteeseen mukaan. Kuvassa suuttimen aukosta tullut ioni kokee taustakaasuvirtauksen saman suuntaisena kuin siihen piirretty paikkavektori vertauspisteestä. Vertauspisteestä katsottuna nopeuksien suuntajakaumasta tulee isotrooppinen.

Kaasuvirtauksen nopeuden suuruus, joka on esitetty kuvan 6 kuvaajassa ionin ja suuttimen välisen etäisyyden funktiona, on arvioitu samojen CosmosFloWorks simulaatioiden avulla. Kaasuvirtauksen nopeus on suuttimesta tullessaan lähellä heliumkaasun äänen nopeutta eli noin 1000m/s ja virtaa edelleen melko tasaisella nopeudella, kunnes edessä oleva skimmeri hidastaa kaasuvirtauksen nopeuden noin 500m/s paikkeille.



Kuva 7: Punaiset ioniradat ovat levinneet kovan pallon törmäysmallin ja räjähdysmallin vaikutuksesta. Vihreät ioniradat kuvaavat ionien liikettä ilman kaasumalleja.

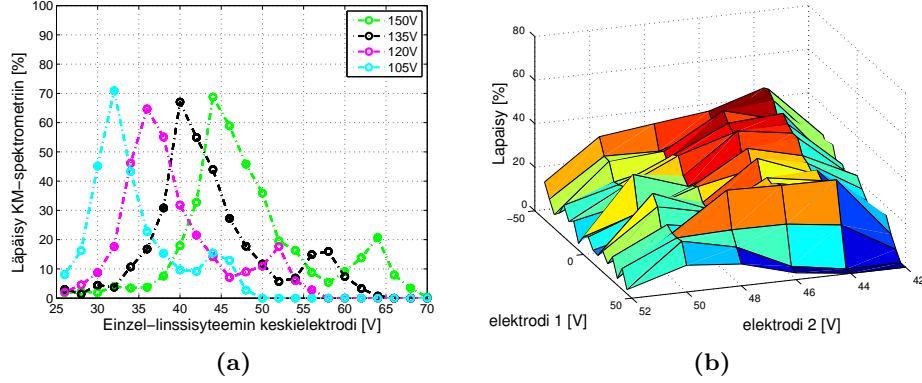
Räjähdysmalli käytettynä kovan pallon törmäysmallin kanssa aiheuttaa ionien leviämisen heti suuttimen jälkeen. Räjähdysmallin eri muuttujien arvoilla, kuten vertauspisteen kohdalla, voidaan vaikuttaa leviämisen voimakkuuteen. Lisäksi siihen vaikuttavat ionin massa, törmäysmallin vaikutusala, ja ionilähteen ja skimmerin välisen sähkökentän voimakkuus. Räjähdysmallin säätäminen todellista tilannetta vastaavaksi on vaikeaa, mutta ionien leviäminen suuttimen alueella noin 30° optisen akselin ympärille on oletettu vastaavan oikeaa tilannetta. Kuvassa 7 on kuvattu ioniradat kaasumallin käytössä ollessa ja ilman kaasumallia. Kuvissa on nähtävissä huomattava ero.

5 Simuloinnin tulokset

5.1 Elektrodien optimointi

Optimaalisimmat elektrodien potentiaalit riippuvat paljon systeemissä liikkuvien ionien massasta ja taustakaasusta ja niiden välisestä vuorovaikutuksesta. Kun ionit kulkevat skimmerin läpi niiden liike-energia on riippuvainen kaasumallin olosuhteista kuten paineesta ionin massasta, sekä ionilähteen ja skimmerin välisestä jännitteestä. Tästä syystä kaikissa olosuhteissa päteviä elektrodien jännitteitä on hankala antaa.

Ongelmia optimoinnissa aiheuttaa ionien taipumus levittäytyä laajalle alalle, jolloin ionisuihkun pitäminen kapeana ja korkeaintensiteettisenä on vaikeaa. Leviämistä esiintyy esimerkiksi heti ionilähteen jälkeen, mikä ai-



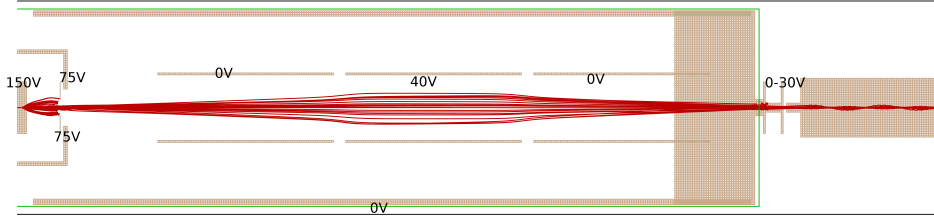
Kuva 8: (a): Lämpäisy QMS:än Einzel-linssisysteemin keskielektrodin jännitteen funktiona eri ionilähteen jännitteillä (b): QMS:än fokusoivan elektrodin(1) ja Einzel-linssisysteemin keskielektrodin jännitteiden vaikutus läpäisyyn QMS:än sisälle.

heuttaa häiviöitä ionien osuessa skimmeriin. Kuitenkin pitämällä ionilähteen skimmerin potentiaaliero mahdollisimman suurena, ja ionilähteen paine matalana, voidaan skimmerin läpi läpäisyä parantaa.

E erityisesti ongelmaa aiheuttaa ionisuihkun leviäminen heti skimmerin jälkeen, koska seuraava fokusoiva efekti tapahtuu vasta ensimmäisen Einzel-linssielektrodin jälkeen. Leviämistä voi yrittää estää alentamalla Einzel-linssisysteemin ensimmäisen elektrodin potentiaalia, mutta simuloinnissa ei huomattu havaittavaa eroa QMS:än saapuvien ionien määrässä eri elektrodin jännitteillä.

Itse Einzel-linssin optimaalisin potentiaali on myös vaikea määrittää, mutta hyvänä lähtökohtana on noin puolet skimmerin potentiaalista. Kuvassa 8a on QMS:ään pääsevien ionien määrä prosentteina skimmerin läpäis-seistä ioneista. Lämpäisy on kuvattu Einzel-linssisysteemin keskielektrodin jännitteen funktiona neljällä eri ionilähteen jännitteellä. Skimmerin jännite oli puolet ionilähteen jännitteestä, ionilähteessä oli 60mbar ja ionien massa oli 232u. Pienempi maksimi 70 % prosentin maksimia suuremmilla jännitteillä johtuu siitä, että ionivirta fokusoituu toisen kerran riittävän isoilla jännitteillä.

Kuvassa 8b on kuvattu kuinka QMS:än fokusoiva elektrodi (kuvan 3 vihreä elektrodi) vaikuttaa ionien läpäisyyn QMS:än kvadrupolikammioon huonosti Einzel-linssillä fokusoidulla ionivirralla. Huomattavaa vaikutusta ohjauselektrodin jännitteillä ei ole ionien läpäisyyn. QMS-ohjauselektrodeista ensimmäistä etuelektrodia on paras pitää mahdollisimman alhaisena.



Kuva 9: Esimerkki optimaalisista elektrodi jännitteistä.

Kuvassa 9 on esimerkki systeemin eri osien ja elektrodien optimaalisimmista jännitteistä, kun kaasun paine on noin 50mbar ja ionin massa noin 200u. Jos eri elektrodien tarkat jännitteet halutaan tietää simulointi kannattaakin suorittaa jokaiselle koejärjestelylle erikseen.

5.2 Emittanssi systeemissä

Jotta ionisuihkun leviämistä ja siitä aiheutuvia ongelmia voidaan analysoida tarkemmin, ionisuihkun laatua tarkasteltiin laskemalla poikittainen emittanssi systeemin eri kohdissa. Poikittainen emittanssi määriteltiin y -akselin suuntaisena neliöllisenä keskiemittanssina, joka laskettiin ionien paikoista ja nopeuksista seuraavasti: [9]

$$\epsilon_y = 4\sqrt{\Delta(y^2)\Delta(y'^2) - \Delta(yy')}, \quad (6)$$

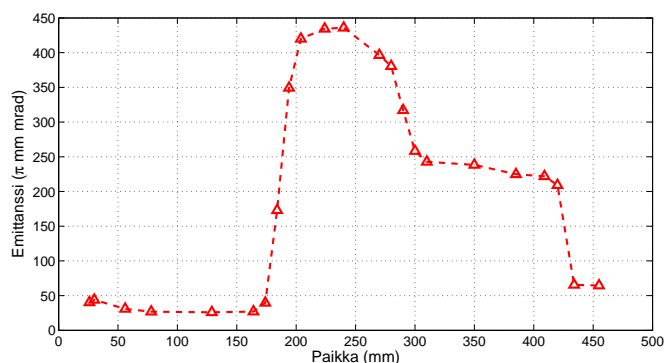
jossa Δ kuvaa standardipoikkeamaa. y' on määritelty ionin poikittaisen nopeuden v_y ja pitkittäisen nopeuden v_x mukaan:

$$y' = \arctan \frac{v_y}{v_x} \approx \frac{v_y}{v_x} \quad (7)$$

Huomaa siis, että x -akseli on optisen akselin suuntainen.

Emittanssin ja faasiavaruuksien laatimiseksi systeemissä simuloitiin noin 1000 skimmerin läpi kulkevaa ionia, kuvan 9 mukaisilla jännitteillä. Kaasuna oli helium 50mbar ionilähteen paineella. Emitanssi mitattiin kaavan (6) mukaisesti useasta kohdasta pitkin simuloitua systeemiä. Kuvassa 10 on merkitty kolmioilla mitatut emitanssin arvot etäisyyden funktiona. Etäisyys mitataan ionilähteen kärjestä.

Ionisuihkun käyttäytymistä tarkasteltiin myös piirtämällä ionit (y, y') -faasiavaruuteen. Kuvassa 11 on kuvattu kuusi eri (y, y') -faasiavaruuden kuvaajaa nuolien mukaisilla paikoilla simuloitavaa systeemiä kuvaavassa esimerkkikuvassa. Faasiavaruuskuvajissa on kukin ioni piirretty pisteellä.



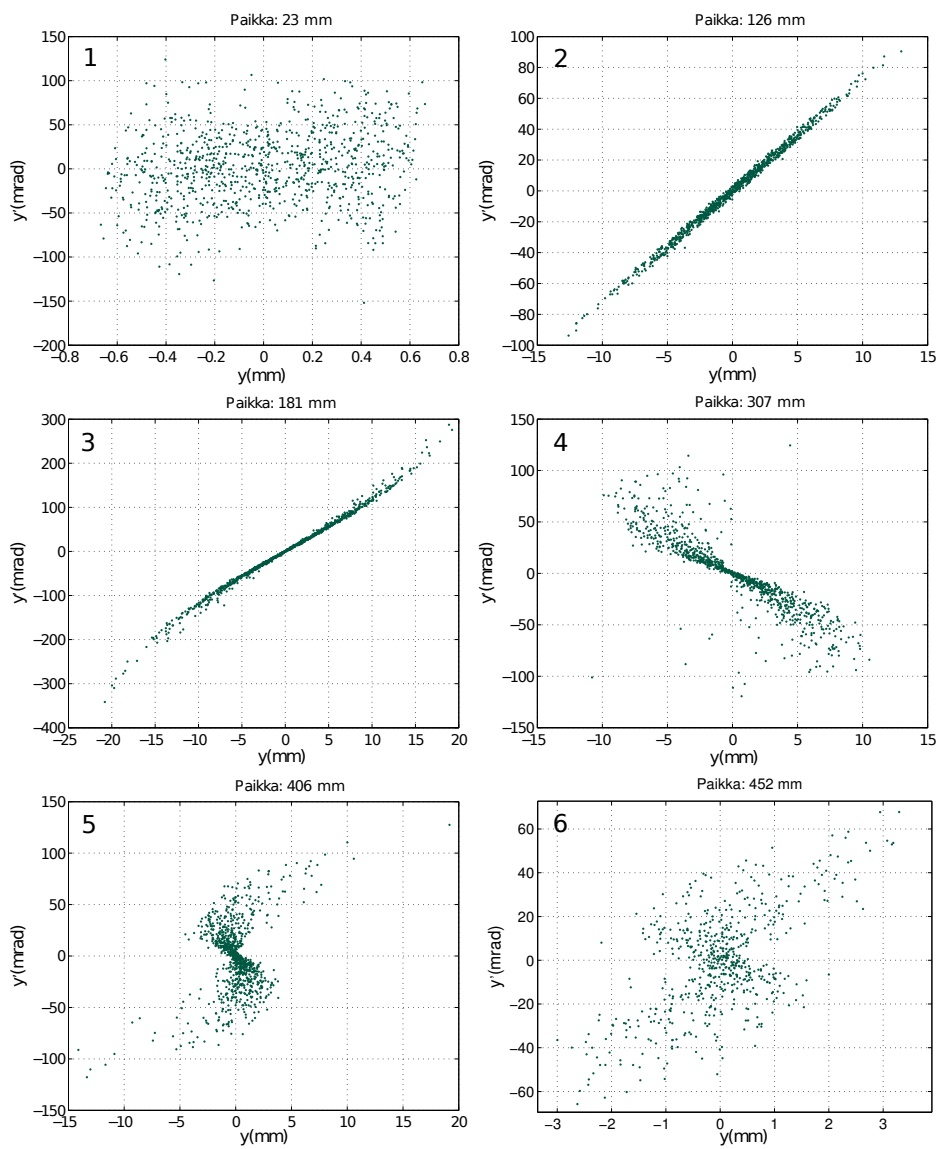
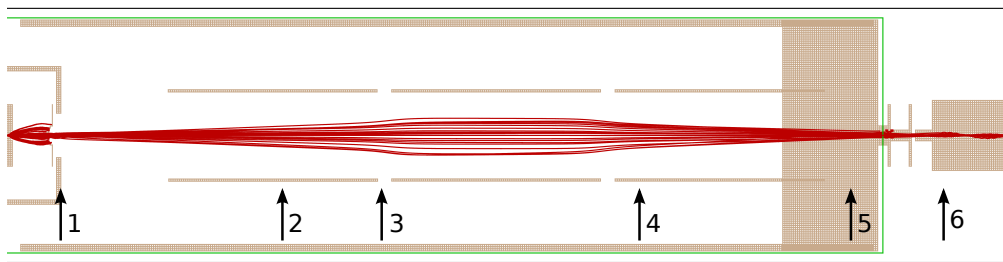
Kuva 10: Emittanssin muutos systeemissä etäisyyden funktiona ionilähteeseen.

Faasiavaruuksista nähdään, että ionisuihku ennen Einzel-linssisysteemin toista elektrodia käyttäytyy lineaarisesti. Ensimmäisessä faasiavaruudessa 1. ionit ovat asettuneet pienelle alueella vähäisellä kulmanopeudella, koska ovat juuri tulleet ulos skimmeristä. Ionit ovat sijoittuneet faasiavaruuteen 2 126mm etäisyydellä ilman vääristymiä kapean ellipsin muotoiselle alueelle. Ionisuihku voidaan sanoa olevan laminaarista tällä alueella.

Emittanssi voimakas kasvu noin 190mm kohdalla johtuu Einzel-linssisysteemin ensimmäisen ja toisen Einzel-elektrodin välissä olevasta ioneja hidastavasta sähkökentästä, mutta toisaalta myös sähkökentän aiheuttaman voiman epälineaarisuudesta. Emittanssi kasvaa hidastavassa sähkökentässä siksi, että pitkittäinen nopeus v_x optisen akselin suuntaan pienenee, mutta poikittainen nopeus v_y ei muutu. Tällöin kaavan (7) mukaan kulmanopeus y' kasvaa ja ionit leviävät suuremmalle alueelle (y, y') -faasiavaruudessa, jolloin emittanssi kasvaa.

Emittanssia kasvattaa myös sähkökentän ioneihin vaikuttava voima, joka on epälineaarinen verrattuna etäisyyteen optisesta akselistä. Tämän epälineaarisen voiman aiheuttava vääristymän synty näkyy faasiavaruudessa 3, jossa kapean ellipsin reunat alkavat kaareutua. Vääristymä kasvattaa irversiibelisti emittanssia, mikä näkyy kuvassa 10 siinä, että emittanssi ei palaudu kiihdyttävän sähkökentän jälkeen kohdassa 300mm. Jos emittanssia kasvattavaa vääristymää ei syntyisi emittanssin tulisi olla sama välillä 300mm-400mm kuin se on välillä 50mm-150mm, koska hidastava- ja kiihdyttävä sähkökenttä ovat symmetrisesti saman muotoisia ja yhtä voimakkaita.

Epälineaarista voimista aiheutuva ioniratojen aberratio näkyy hyvin QMS:än etuelektrodin edessä määritellyssä faasiavaruudessa 5 etäisyydellä



Kuva 11: Ionien muodostamat (y,y') -avaruudet kuudessa eri systeemin kohdassa.

406mm. Tässä faasiavaruudessa tietyillä paikan arvoilla kulmanopeus saa sekä positiivisia että negatiivisia arvoja. Tämä tarkoittaa, että näissä kohdissa ionien radat menevät ristiin ja ionisuihkun laminaarisuus on huonoa, mikä vaikeuttaa ionien fokuointia QMS:än sisälle. Emittanssi pienenee noin 430mm kohdalla, koska osa ioneista osuu QMS-etuelektrodiin, jolloin osu-
neet ionit eivät enää etene systeemissä. Vain QMS-etuelektrodin aukosta sisään liikkuvat hyvin suuntautuneet ionit pääsevät liikkumaan eteenpäin. Näillä ioneilla on siksi matala emittanssi. Kyseiset ionit on kuvattu (y,y') -avaruudessa kuvan 11 kaaviossa 6.

Vääritymisistä johtuva aberratio on seurausta siitä, että ionisuihku on niin levinnyt niin paljon tullessaan Einzel-linssisysteemiin, että siihen vaikuttavat Einzel-linssisysteemin elektrodien reunamien epälineaariset voimat. Tästä syystä ionien leviämistä skimmerin jälkeen olisi hyvä pienentää.

5.3 Lämpäisyn tehokkuus

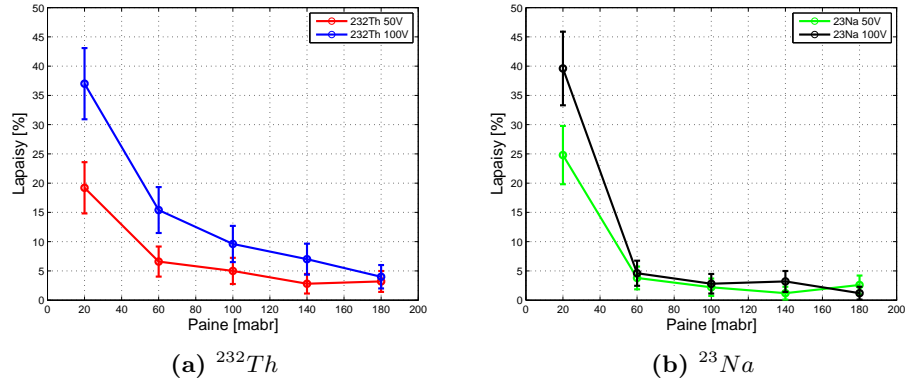
Ioneja menetetään niiden liikkuessa offline-laitteiston läpi. Menetykset ovat etenkin suuria skimmerin alueella, koska ionit leviävät kaasumallin vaikutuksesta. Leviämisen suuruus on suoraan verrannollinen ionilähteen ja skimmerin väliseen jännitteeseen ja on erittäin herkästi riippuva paineesta. Kuvassa 12a ja 12b on kuvattu toriumin ja natriumin läpäisy paineen funktiona ionilähteen ja skimmerin välisillä 50V ja 100V potentiaalieroilla.

Räjähdysmallin antamia läpäisytehokkuuksia pitää kuitenkin tarkastella vain suuntaa antavina, koska todellinen kaasusuihku on ylisooninen, ja sen virtaus voi olla hyvinkin erilainen räjähdysmalliin verrattuna. Ylisoonisen kaasusuihkun muotoon voidaan mm. vaikuttaa taustapaineen muutoksilla. [10]

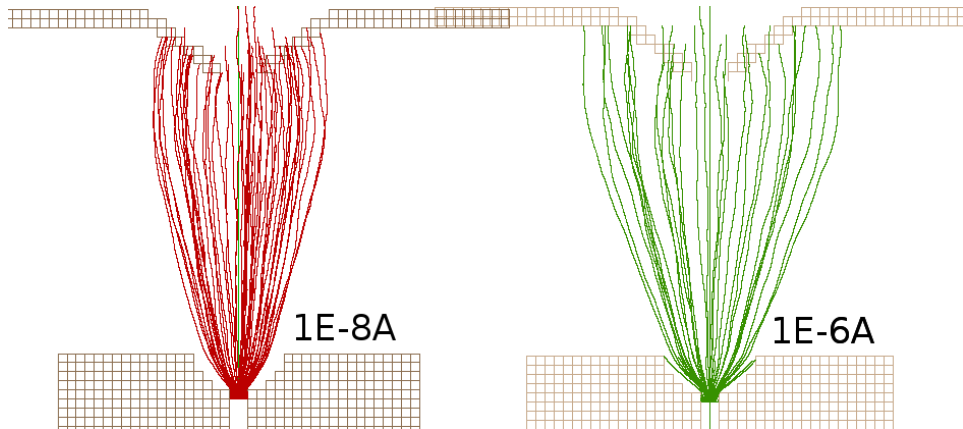
Skimmerin jälkeen suurimmat häviöt tapahtuvat QMS-etuelektrodiin. Einzel-linssisysteemissä voi myös tapahtua häviöitä, jos ionisuihku leviää paljon skimmerin jälkeen. Simulaatioiden perusteella voidaan arvioida häviöiden olevan noin 30% luokkaa ennen QMS:än kammiota.

5.4 Avaruusvarauksen vaikutus

Avaruusvarauksen vaikutusta simuloitiin SIMION-ohjelmiston sisäänrakennetulla beam-repulsion toiminnolla, jolla avaruusvarauksen vaikutusta mallinnetaan olettamalla jokainen ioni kulkusuuntaansa äärettömän pitkäksi viivavaraukseksi. Viivavarauksen suuruuden SIMION-ohjelmisto arvioi ionin nopeudesta ja käyttäjän ampeereissa antamasta kokonaisionivirran suuruudesta. SIMION-ohjelmisto ottaa huomioon vain ioni-ioni -vuorovaikutuksen. Mahdollista ionien vaikutusta itse sähkökenttiin ei oteta huomioon.



Kuva 12: Toriumin ja natriumin skimmerin läpäisy paineen funktiona kahdella eri skimmerin ja ionilähteen potentiaali erolla.



Kuva 13: Avaruusvarauksen vaikutus ioniratoihin ionilähteen ja skimmerin alueella.

Beam-repulsion simulaatioon vaatii, että kaikki simuloitavat ionit lennätetään yhtä aikaa ja ionit pidetään samassa tasossa. Tämä tapahtuu siirtämällä jokaista ionia omalla aika-askeleella siten, että ionit pysyvät yhdessä tasossa. Tason suunnan määrää johtava ionit, joka pakotetaan siirtymään koko simuloitavan systeemin läpi.

Kuvassa 13 on kuvattu avaruusvarauksen vaikutus kahdella ionivirran arvolla $1 \cdot 10^{-8}\text{A}$ ja $1 \cdot 10^{-6}\text{A}$. Simulaatioiden perusteella $1 \cdot 10^{-6}\text{A}$ ionisuihkun läpäisy on noin 50% huonompi verrattuna tilanteeseen, jossa ionisuihkun virta ei aiheuta leviämistä

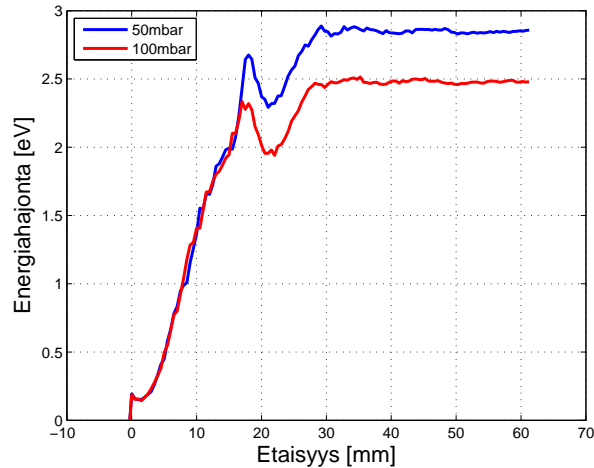
5.5 Energiahajonta

QMS:sän massaerottelukykyyn vaikuttavan energiahajonnan muodostumista tutkittiin laskemalla simulaation aikana ionien kokonaisnopeuden neliön standardipoikkeama $\Delta(v^2) = \langle v^2 - \langle v^2 \rangle \rangle$ etäisyyden funktiona ionilähteestä. Nopeuden neliön standardipoikkeamasta voidaan edelleen laskea energiahajonta:

$$\Delta E = \frac{1}{2} m_{ion} \Delta(v^2) \quad (8)$$

Toisin kuin ioniradat, energiahajonnan suuruus on herkkä skimmerin jälkeisen alueen paineelle. Siksi energiahajontaa simuloidessa painemallia muutettiin muissa simulaatioissa käytetystä painemallista niin, että painemallissa on varovaisempi paineenlasku skimmerin jälkeen estäen näin energiahajonnan aliarvioinnin. Energiahajontaa simuloitaessa painekäyrä kuvata 4a poikkeava siinä, että skimmerin jälkeinen paine laskee eksponentiaalisesti neliöllisen laskun sijasta. Lisäksi taustapaine on laskettu alle 1 mbar:in.

Kuvassa 14 on energiahajonnan muodostuminen ioneihin ionilähteen ja skimmerin alueella. Ionilähde sijaitsee 0mm:in kohdalla ja skimmeri noin 15mm:in kohdalla. Kuvaaajassa otettu huomioon kaikissa kohdissa vain ne ionit, jotka läpäisivät skimmerin. Läpäisseiden ionien määrä oli 244 ionia 50mbar paineessa ja 224 ionia 100mbar paineessa ja ionien massana käytettiin 232u. Simulaatioissa käytetyt jännitteet olivat 150V ionilähteessä ja 75V skimmerissä. Einzel-linssisysteemin ensimmäinen elektrodi on maas-



Kuva 14: Energiahajonnan muodostuminen kahdella ionilähteen paineen arvolla. Energiahajonta tasoittuu noin 3eV tienoille.

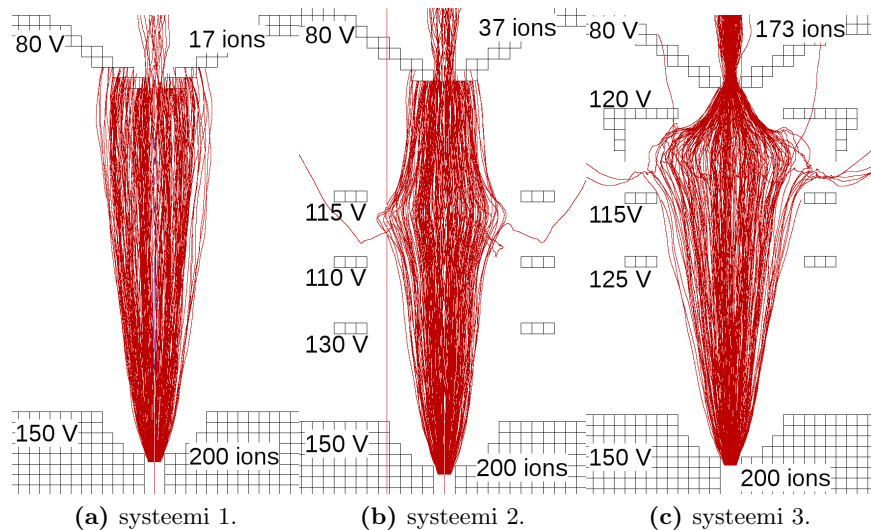
sa (0V), jolloin skimmerin jälkeen on myös ioneja kiihdyttävä sähkökenttä.

Ionien energiahajonta kasvaa kunnes skimmerin alueella taustakaasun nopeus laskee ja sähköisen potentiaalin muutos on hyvin pieni. Tällä alueella ionien satunnainen liike hidastuu törmäyksissä taustakaasun atomeihin ja energiahajonta laskee. Ionien tullessa ulos skimmerin aukosta ionit lähtevät voimakkaasti kiihtymään alhaisen paineen takia. Tällöin ionien törmäyksistä taustakaasun atomeihin tulee voimakkaita ja energiahajonta nousee, kunnes paine laskee niin alas ettei törmäyksiä enää tapahdu ja energiahajonta tasaantuu. Paineesta ja ionilähteen potentiaalista riippuen energiahajonnan suuruuden voidaan arvioida olevan noin 2-3eV luokkaa.

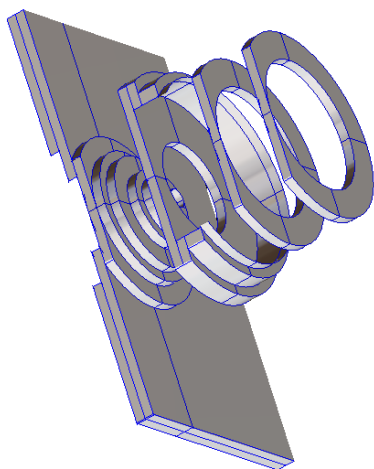
5.6 Ohjauslinssisysteemi

Koska häviöt skimmeriin ovat edellisten simulaatioiden mukaan suuret ionien leviämisen vuoksi, skimmerin edessä testattiin ohjauslinssisysteemejä, jotka koostuvat noin 1-0,5cm halkaisijaltaan olevista renkaan muotoisista elektrodeista. Näillä elektrodeilla yritettiin estää ionien leviäminen ja ohjata ne skimmerin aukkoa kohti.

Simulaatiolla testattiin kahta eri tyyppistä ratkaisua. Ensimmäinen testattava rengaselektrodisysteemi koostui kolmesta noin 7mm halkaisijaltaan



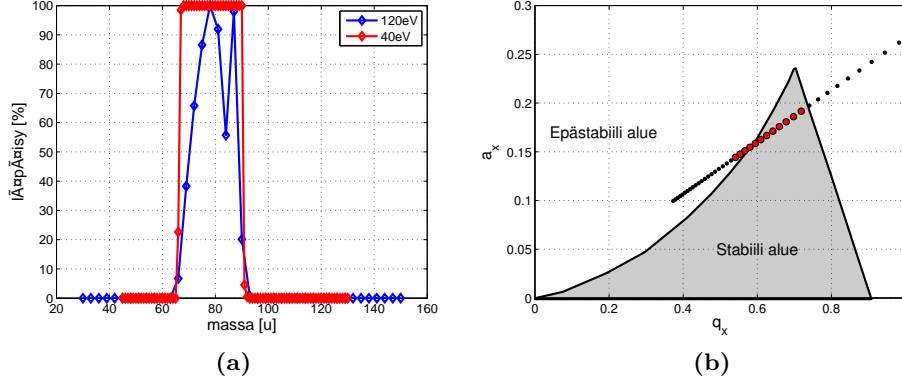
Kuva 15: Rengaselektrodisysteemien mallit sekä niiden tuottamat ioniradat ja läpäisyt. Yksinkertainen toteutus on kuvassa 15b ja kuvassa 15c on viimeinen elektrodi muotoiltu optimaalisesti. Kuvassa 15a on tilanne ilman rengaselektrodeja.



Kuva 16: Toisen rengaselektrodisysteemin kolmiulotteisen mallin poikkileikkaus.

olevasta rengaselektrodista kuvan 15b mukaisesti. Toisessa testattavassa rengaselektrodisysteemissä viimeinen rengaselektrodi oli muotoiltu ohjaavaksi ja siirretty lähemmäksi skimmeriä. Tämä rengaselektrodi systeemi on kuvattu ioniratoineen vastaavasti kuvissa 15c ja 16.

Verrattuna simulaatioon ilman ohjauselektrodiä (kuva 15a), missä skimmerin läpäisy vain 17 ionia, simulaatioiden mukaan ohjauselektrodeilla voi olla mahdollista lisätä huomattavasti ionien läpäisyä skimmerin läpi. Toisaalta optimaalisen läpäisyn aikaan saamiseksi elektrodien oikea muoto on tärkeää, sekä se, että viimeinen rengaselektrodi sijaitsee lähellä skimmeriä. Lisäksi sen jännite tulisi olla huomattavasti korkeammalla kuin skimmerin. Liian suuri potentiaaliero, etenkin korkeapaineisessa ympäristössä, voi kuitenkin aiheuttaa kipinöintiä. Lisäksi todellisuudessa rengaselektrodit vaikuttavat kaasusuihkun virtaukseen, mitä ei huomioitu simulaatiossa. Näistä syistä simulaatioissa saavutettua läpäisyä voi olla vaikea saavuttaa käytännössä. Simulaatioiden perusteella voi kuitenkin todeta, että jo varsin yksinkertaisella rengaselektrodisysteemillä on mahdollista parantamaan ionien läpäisyä skimmerin läpi.



Kuva 17: QMS simuloinnin massaerottelu. Kuvassa (a) on ionien läpäisy ionin massan funktiona kahdella eri ionienergialla. Kuvassa (b) on kuvattu QMS:än stabiilisuus alue (q_x, a_x)-avaruudessa, sekä massaskannaus pisteillä, jossa isommat punaiset pisteet kuvaavat yli 50% läpäisyä.

5.7 QMS simulaatiot

QMS:än toiminnan mallintaminen toteutettiin myös käyttÄäjäohjelmilla, jossa käytettiin SIMION-ohjelmiston fast-adjust-toimintoa. Offline-laitteistossa käytetyn QMS:än tarkkaa toimintaa ei kuitenkaan tunneta, joten sen toiminnan mallintamisen ohjelmoitu toteutus perustuu kirjallisuudessa esiintyvÄän yleiseen malliin. [11] Toteutus on lähdekoodissa riveillä 331-349, missÄ spektrometrin sauvojen rf-potentiaalia muutetaan ionin lentoajan ja QMS:än toimintataajuuden $\omega = 2\pi f$ mukaan. Ohjelmalle annetaan rf-potentiaalin amplitudi V ja aksiaalinen DC-potentiaali U , sekä mahdollinen sauvojen kelluntajÄännite. Sauvoissa on siis jÄännite

$$U_{tot}(t) = \pm (U + V \sin(\omega t)) \quad (9)$$

QMS:ssÄ liikkuvien ionien ratoja kuvaavat Mathieun yhtÄlÖiden ratkaisut, joista voidaan mÄÄrittÄÄ vaakasuuntaan (x) ja pystysuuntaan (y) seuraavat stabiilisuusparametrit:

$$a_x = -a_y = \frac{8eU}{mr_0^2\omega^2} \quad q_x = -q_y = \frac{4eV}{mr_0^2\omega^2}, \quad (10)$$

jossa m on ionin massa ja r_0 on etÄisyys optiselta akselilta sauvaan. NÄmÄ yhtÄlÖt olettavat, ettÄ sauvojen säteen r_r ja niiden etÄisyyden optiselta akselilta r_0 vÄlillÄ pÄtee $r_r \approx 1.3r_0$, mikÄ simuloidussa QMS:ssÄ pitÄÄ paikkansa. Ionien radat ovat vain tietyillÄ stabiilisuusparametreillÄ a ja q sellaisia,

että ionit liikkuvat QMS:än läpi. Kuvassa 17b on kuvattu harmaalla alueella (a,q) -stabiilisuusalue.

QMS:än toimintaa testattiin ajamalla erimassaisia ioneja vakioenergialla spektrometrin läpi, kun $U = 40V$, $V = 300V$ ja $f = 2.23MHz$. Kuvassa 17a on kuvattu läpäisy QMS:ään ionin massan funktiona välillä 30u-150u 120eV:in ioneille ja välillä 45u-130u 40eV:in ioneille. Ioneja kussakin simulaatiossa oli 200 kappaletta. Lisäksi kuvaan 17b on piirretty piste kunkin simuloidun 40eV ionin massan kohdalle niin, että isot punaiset pisteet kuvaavat yli 50% läpäisyä ja pienet mustat pisteet alle 50% läpäisyä. Kuvasta 17a näkee, että liian suuri ionien energia saattaa häiritä QMS:än toimintaa. Simulaatioiden perusteella on silti vaikea sanoa millä ionien energioilla käytössä olevan QMS:än toiminta häiriintyy. Kuva 17b perusteella voidaan kuitenkin todeta, että QMS:än simuloitu toiminta vastaa erinomaisesti teoriassa ennustettuja arvoja.

6 Yhteenveto

Kaasumallin takia simuloinnin kvantitatiivinen tulos riippuu suuresti käytetyn ionin massasta, van der Waals säteestä, sekä etenkin kaasun paine ja nopeusfunktioista, joiden tarkkoja arvoja on hankala tietää. Siksi tarkkoja elektrodien potentiaaleja ja läpäisyjä on vaikea arvioida simulaatioiden perusteella. Kuitenkin matalan paineen alueilla voidaan suurpiirteisesti arvioida tarvittavien jännitteiden suuruuksia.

Kvadrupolimassaspektrometrin simuloinnin vertaus teoreettisiin odotuksiin osoitti, että spektrometrin toimintaa on myös mahdollista mallintaa tämän työn simulaatiototeutuksessa. Näin voidaan tutkia etukäteen, että kuinka koeolosuhteet voivat vaikuttaa massaspektrometrin toimintaan.

Simulaation nopeus oli verrattain hidas, koska kovan pallon törmäysmallissa suurissa paineissa tapahtuvien törmäysten määrä on suuri. Tässä työssä tehtyä vastaavaa nopeampaa simulointia ilman painetta vastaavissa paineissa on tehty statistisilla diffuusio simuloinnilla. [12] Tässä esitettyä simulaatiototeutusta on mahdollista muuntaa tällaiseksi diffuusio simuloinniksi. Tämä tulee kysymykseen etenkin, jos tässä työssä esitettyiltä simuloinneilta vaaditaan nopeaa suoriutumista.

Simulaatiot osoittavat, että hyvää läpäisyä koko systeemissä voi olla käytännössä vaikea saavuttaa. Läpäisyä skimmerin läpi voidaan parantaa pitämällä ionilähteen skimmerin potentiaaliero mahdollisimman suurena, ja ionilähteen paine matalana. Lisäksi ionisuihkun leviäminen Einzel-linssisysteemissä aiheuttaa emittanssin kasvua ja vaikeuttaa ionien tehokasta siirtymistä QMS:ään. Optimaalisimmillaan koko systeemin läpäisytehokkuuden

voidaan arvioida olevan noin 20% luokkaa. Einzel-linssin optimaalisen potentiaali on vaikea määrittää yleispätevästi, mutta hyvänä lähtökohtana on noin puolet skimmerin potentiaalista. Tässä esitettyjen simulaatioiden todellinen hyöty tulee esiin sitten, kun offline-laitteistossa suoritettavien kokeiden tarkat järjestelyt tiedetään. Tällöin tehtyjen simulaatioiden avulla voidaan optimoida mittalaitteisto ja paikantaa mahdollisia ongelmakohtia.

Viitteet

- [1] J. Äystö, “Development and applications of the igisol technique,” *Nuclear Physics A*, vol. 693, no. 1-2, pp. 477 – 494, 2001.
- [2] D. J. Manura and D. A. Dahl, *SIMION® Version 8.0 User Manual*. Ringoes, NJ: Scientific Instruments Services Inc., 2008.
- [3] D. A. Dahl, “Simion for the personal computer in reflection,” *International Journal of Mass Spectrometry*, vol. 200, no. 1-3, pp. 3 – 25, 2000.
- [4] R. Ierusalimsky, W. Celes, and L. H. de Figueiredo, “The programming language lua.” <http://www.lua.org/>, Jan. 2010.
- [5] D. J. Manura, “Additional notes on the simion hs1 collision model,” tech. rep., Scientific Instruments Services Inc., Feb. 2007.
- [6] CosmosFloWorks 2006PE SPO, Structural Research and Analysis Corp.
- [7] A. Iivonen, K. Riikonen, R. Saintola, K. Valli, and K. Morita, “Focusing ions by viscous drag and weak electric fields in an ion guide,” *Nuclear Instruments and Methods in Physics Research A*, vol. 307, pp. 69–79, Sept. 1991.
- [8] P. Karvonen, I. Moore, T. Sonoda, T. Kessler, H. Penttilä, K. Peräjärvi, P. Ronkanen, and J. Äystö, “A sextupole ion beam guide to improve the efficiency and beam quality at igisol,” *Nuclear Instruments and Methods in Physics Research Section B: Beam Interactions with Materials and Atoms*, vol. 266, no. 21, pp. 4794 – 4807, 2008.
- [9] P. M. Lapostolle, “Possible emittance increase through filamentation due to space charge in continuous beams,” *Nuclear Science, IEEE Transactions on*, vol. 18, pp. 1101 –1104, june 1971.
- [10] B. A. Marsh, *In-Source Laser Resonance Ionization at ISOL Facilities*. PhD thesis, School of Physics and Astronomy, University of Manchester, 2007.
- [11] P. H. Dawson, *Quadrupole mass spectrometry and its applications*. American Institute of Physics, 1995.
- [12] A. D. Appelhans and D. A. Dahl, “Simion ion optics simulations at atmospheric pressure,” *International Journal of Mass Spectrometry*, vol. 244, no. 1, pp. 1 – 14, 2005.

Liitteet

A Lähdekoodi

```
1  simion.workbench_program()
2
3  -- ### ALL IONS SPLAT at
4  adjustable force_all_ions_splat_at_x_mm = 70
5  local ions_forced_to_splat = {}
6  adjustable _Leading_Ion_Splat_Pos_mm = 10
7  adjustable _disable_collisions_at = 60
8
9  local test_variable_1_start = 150 --not used
10 local test_variable_1_step = 40
11 local test_variable_1_end = 10
12 local test_variable_2_start = 75 --not used
13 local test_variable_2_step = 100
14 local test_variable_2_end = 15
15 local current_test_variable_1_value = test_variable_1_start
16 local current_test_variable_2_value = test_variable_2_start
17 local potentials1 = {} --an array of used potentials1 for each fly
18 local potentials2 = {} --an array of used potentials2 for each fly
19
20 -- Ion guide pressure
21 local const_pressure = 100 --mbar
22
23 local is_program_initialized = false
24 local m_is_previously_opened = false
25 local v_is_previously_opened = false
26 local recording_planes = {7,10,24,29,35,185,292,400,461} --{10,26,34,77,185,292,396,418,425,435,450}
27 local plane_data = {}
28 local flies_ions_in_plane = {} -- ion count for each fly aand plane
29 local ions_flied = 0 -- total number of ions flied in a fly
30
31 local ion_velocities = {}
32 local xpositions_sum = {}
33 local xpotentials_sum = {}
34 local xstep=0.5
35 local xstart=7
36 local xcurrent = {}
37 local xend=69
38 local xindex = {}
39 local vx_ion_count={}
40
41 local sim.i = 0 --index for fly, used as array index
42
43
44 --##### GAS MODEL
45
46 local collisions_for_leading_ion = true
47 local _mean_free_path_mm = -1 -- negative=program calculates mean free path
48 local _gas_mass_amu = 4.0 -- For He
49 local _temperature_k = 300.0
50
51 local _pressure_pa = 10000 --dummy variable
52
53 -- Collision-cross section (m^2)
54 -- adjustable _sigma_m2 = 2.88E-19 -- (He_vdW_radius + Ni+1_vdW_radius)^2*Pi
55 -- local _sigma_m2 = 2.72E-19 -- (He_vdW_radius + Na+1(Ne)_vdW_radius)^2*Pi
56 local _sigma_m2 = 3.33E-19 -- (He_vdW_radius + U_vdW_radius)^2*Pi
57 -- Mean number of time steps per MFP.
58 local _steps_per_MFP = 20.0
59
60 -- Collision marker flag.
61 local collisions_marked = false
62
63 -- How much trace data (average KE) to output.
64 -- (0=none, 1=at each splat, 2=at each collision)
65 adjustable _trace_level = 0
66 -- If _trace_level is 2, this is the number of collisions before each trace.
67 -- This reduces the verbosity of the trace.
68 adjustable _trace_skip = 100
69
70 adjustable explosion_model_limit_z_mm = 23
71 -- current running average of KE for each particle. maps ion_number --> KE.
72 local ke_averages = {}
73
74 local last_collision_times = {}
75 local last_ion_number = -1
76 local last_speed_ion = -1
```

```

77
78 -- Currently used mean-free path (-1 = undefined).
79 local effective_mean_free_path_mm = -1
80
81 -- Maximum time step (usec) that fast-adjust should permit.
82 -- This is continually updated so that the _steps_per_MFP setting
83 -- remains meaningful.
84 local max_timestep = 0.000002
85
86 -- ##### QMS
87 local is_QMS_enabled = false
88 adjustable phase_angle_deg = 0.0 -- entry phase angle of ion
89 adjustable frequency_hz = 2.23E6 -- RF frequency of quad (in hz)
90 adjustable pe_update_each_usec = 0.005 -- PE display update period (in usec)
91 adjustable _quad_axis_voltage = 0.0 -- quad axis voltage
92
93 local omega = 1.0 -- freq in radians / usec
94 local theta = 0.0 -- phase offset in radians
95
96 local next_pe_update = 0.0 -- next time to update pe surface
97
98
99
100
101
102 -- ##### Define constants
103 local k = 1.3806505e-23 -- Boltzmann constant (J/K)
104 local kg_amu = 1.6605402e-27 -- (kg/amu) conversion factor
105 local pi = 3.1415926535 -- PI constant
106 local eV_J = 6.2415095e+18 -- (eV/J) conversion factor
107
108 local is_QMS_values_initialized = false
109
110 -- ##### Other Global variables
111 local is_previously_opened = false
112
113 function erf(z)
114     local z2 = abs(z)
115     local t = 1 / (1 + 0.32759109962 * z2)
116     local res = ( - 1.061405429 ) * t
117     res = (res + 1.453152027 ) * t
118     res = (res - 1.421413741 ) * t
119     res = (res + 0.2844966736) * t
120     res = ((res - 0.254829592 ) * t) * exp(-z2*z2)
121     res = res + 1
122     if z < 0 then res = -res end
123     return res
124 end
125
126 -- Normal distribution calculated with Box-Muller algorithm:
127 function gaussian_random()
128     local s = 1
129     local var1, var2
130     while s >= 1 do
131         var1 = 2*rand() - 1
132         var2 = 2*rand() - 1
133         s = var1*var1 + var2*var2
134     end
135     return var1*sqrt(-2*ln(s) / s)
136 end
137
138
139 --zeropoint at optical axis for functions below,
140 --usually near to ion creation and nozzle positio
141 local f_zero_x_mm=7.25
142
143 --Gas pressure, exponential decrease
144 function pressure(ionx, iony, ionz, scale)
145     local conservative_pressure_drop = false
146     local distance = 0
147     local nozzle_expstart_offset = 0
148     local skimmer_pos = 15.0
149     if ionx > f_zero_x_mm then
150         distance = ((ionx-f_zero_x_mm)^2 + iony^2 + ionz^2)^0.5
151     end
152     local A,B,C,d1,d2 = 10000,200,30,1,0.5
153     local h = 8.6
154     local h2 = 1300
155     local cutpoint = 11
156     local pos_x_mm = ionx - f_zero_x_mm
157     if (pos_x_mm < 0) or distance < nozzle_expstart_offset then
158         return scale*10000
159     elseif (conservative_pressure_drop and
160         distance < 1.0) then

```

```

161     return scale*(A*0.6-h2*(distance-nozzle_expstart_offset)^2)
162 elseif (pos_x_mm < skimmer_pos) then
163     return scale*((A-B)*math.exp(-d1*(distance-nozzle_expstart_offset))+B)
164 elseif (pos_x_mm < 20.0) then
165     return scale*(B-h*(pos_x_mm-skimmer_pos)^2)
166 else
167     return 1
168 end
169 end
170
171 -- Gas velocity (explosion model)
172 function gas_velocity(ionx, iony, ionz, scale)
173     local v_tot = 1
174     local v_max,a = 1000,1.2/3;
175     local pos_x_mm = ionx - f_zero_x_mm
176     if pos_x_mm < 0 then
177         v_tot = scale*v_max
178     elseif pos_x_mm < 9 then
179         v_tot = scale*(v_max-(100/9)*pos_x_mm)
180     elseif pos_x_mm < 15 then
181         v_tot = scale*(900-100*(a*(pos_x_mm-9))^2 + 15*(a*(pos_x_mm-9))^3)
182     else
183         v_tot = scale*530
184     end
185     v_tot = v_tot/1000 --from m/s to mm/usec
186     local x_component_mm = ionx - f_zero_x_mm + 0.5
187     if (ionx < explosion_model_limit_z_mm) and (x_component_mm > 0.75) then
188         local dist = (x_component_mm^2 + iony^2 + ionz^2)^0.5
189         return x_component_mm/dist*v_tot, iony/dist*v_tot, ionz/dist*v_tot
190     else
191         return v_tot, 0, 0
192     end
193 end
194 end
195
196 function temperature(ionx, iony, ionz)
197     local cutpoint = 2
198     local A=300
199     local B=100
200     local C=10
201     local d1=4
202     local d2=0.4
203     if ionx > f_zero_x_mm then
204         distance = ((ionx-f_zero_x_mm)^2 + iony^2 + ionz^2)^0.5
205     else
206         distance = false
207     end
208
209     if distance then
210         if distance < cutpoint then
211             T=(A-B)*math.exp(-d1*distance)+B;
212         else
213             T=C*math.exp(d2*(distance-cutpoint))+B-C;
214         end
215         if T < A then
216             return T
217         else
218             return A
219         end
220     else
221         return A
222     end
223 end
224
225 --#### Potentials
226 function segment.init_p_values()
227     if ion_instance == 1 then
228         adj_elect01 = current_test_variable_1_value
229         adj_elect02 = current_test_variable_1_value/2
230     end
231     print('test_var_1 = ', current_test_variable_1_value, 'test_var_2 = ', current_test_variable_2_value)
232 end
233
234
235 function segment.initialize()
236     -- Initialization chunk for variable and table initialization
237     if (not is_program_initialized) then
238         is_program_initialized = true
239
240         for i=1,#recording_planes do
241             flys_ions_in_plane[i] = {
242                 ["plane_pos"] = recording_planes[i],
243                 ["count"] = {}
244             }

```

```

245     end
246     for i=1,#recording_planes do
247         plane_data[i]={
248             ["plane_pos"] = recording_planes[i],
249             ["is_previously_opened"] = false,
250             ["is_passed"]={},
251             ["tof"]={},
252             ["x_pos"]={},
253             ["y_pos"]={},
254             ["z_pos"]={},
255             ["x_vel"]={},
256             ["y_vel"]={},
257             ["z_vel"]={},
258             ["potential"]={},
259         }
260     end
261     print("initialization ready")
262 end
263
264 if ions_flied < ion_number then
265     ions_flied = ion_number
266 end
267
268 xcurrent[ion_number] = xstart
269 xindex[ion_number] = 1
270 -- New index and counting starts from zero for each fly
271 if ion_number ~= 1 then
272     return
273 end
274 -- Increase simulation run counter
275 sim_i = sim_i+1
276
277 ion_velocities = {}
278 times_skipped = {}
279 xpositions_sum = {}
280 xpentials_sum = {}
281 vx_ion_count = {}
282
283 -- Each fly gets clean plane_data tables for data recording
284 -- one plane_data table for one recording plane
285 for i,v in ipairs(plane_data) do
286     v.is_passed = {}
287     v.tof = {}
288     v.x_pos = {}
289     v.y_pos = {}
290     v.z_pos = {}
291     v.x_vel = {}
292     v.y_vel = {}
293     v.z_vel = {}
294 end
295 -- In begining any ion has not passed any of the planes
296 for i,v in ipairs(plane_data) do
297     v.is_passed[ion_number] = false
298     v.is_passed[ion_number] = false
299     v.is_passed[ion_number] = false
300 end
301
302 for i,v in ipairs(flys_ions_in_plane) do
303     v.count[sim_i] = 0
304 end
305 end
306
307 function segment.tstep_adjust()
308     -- Ensure time steps are sufficiently small. They should be some
309     -- fraction of mean-free-path so that collisions are not missed.
310
311
312     if max_timestep and ion_time_step > max_timestep then
313         ion_time_step = max_timestep
314     end
315
316     -- local temp = abs(xstep*0.1/ion_vx.mm)
317     -- if ion_time_step > temp then
318     --     -- print(ion_time_step, " \t", temp)
319     --     ion_time_step = temp
320     -- end
321 end
322
323 function segment.efield_adjust()
324     -- No field y,z-directions for leading ion
325     if ion_number == 1 then
326         ion_dvoltsy_mm = 0
327         ion_dvoltsz_mm = 0
328     end

```

```

329 end
330
331 function segment.fast_adjust()
332     if is_QMS_enabled then
333         -- initialize values
334         if is_QMS_values_initialized == false then
335             is_QMS_values_initialized = true
336             theta = phase_angle_deg * 3.141592 / 180
337             omega = frequency_hz * 6.28318E-6 -- Hz to rads/usec
338         end
339
340         local dcvolts = 0
341         local rfvolts = 295.607
342         local tempvolts = sin(ion_time_of_flight * omega + theta) * rfvolts + dcvolts
343         if (ion_instance == 2) then
344             adj_elect03 = -quad_axis_voltage + tempvolts
345             adj_elect04 = -quad_axis_voltage - tempvolts
346         end
347     end
348 end
349
350 function segment.other_actions()
351     for i,v in ipairs(plane_data) do --For every recording plane
352         if (not v.is_passed[ion_number]) then
353             if ion_px_mm > v.plane_pos then --record data when ion passes the plane
354                 v.is_passed[ion_number] = true
355                 v.tof[ion_number] = ion_time_of_flight
356                 v.x_pos[ion_number] = ion_px_mm
357                 v.y_pos[ion_number] = ion_py_mm
358                 v.z_pos[ion_number] = ion_pz_mm
359                 v.x_vel[ion_number] = ion_vx_mm
360                 v.y_vel[ion_number] = ion_vy_mm
361                 v.z_vel[ion_number] = ion_vz_mm
362                 v.potential[ion_number] = ion_volts
363             end
364         end
365     end
366 end
367 if (ion_number ~= 1) then
368     if ion_px_mm > xcurrent[ion_number] and xcurrent[ion_number] < xend then
369         local multpl = 1;
370         if not times_skipped[xindex[ion_number]] then
371             times_skipped[xindex[ion_number]] = 0
372         end
373         while ion_px_mm > xcurrent[ion_number] + xstep*multpl do
374             if not times_skipped[xindex[ion_number]] then
375                 times_skipped[xindex[ion_number]] = 0
376             end
377             times_skipped[xindex[ion_number]] =
378                 times_skipped[xindex[ion_number]] + 1
379             xindex[ion_number] = xindex[ion_number] + 1
380             multpl = multpl + 1
381         end
382         if not vx_ion_count[xindex[ion_number]] then
383             vx_ion_count[xindex[ion_number]] = 0
384         end
385         vx_ion_count[xindex[ion_number]] =
386             vx_ion_count[xindex[ion_number]] + 1
387         if not xpositions_sum[xindex[ion_number]] then
388             xpositions_sum[xindex[ion_number]] = 0
389         end
390         xpositions_sum[xindex[ion_number]] =
391             xpositions_sum[xindex[ion_number]] + ion_px_mm
392         if not xpentials_sum[xindex[ion_number]] then
393             xpentials_sum[xindex[ion_number]] = 0
394         end
395         xpentials_sum[xindex[ion_number]] =
396             xpentials_sum[xindex[ion_number]] + ion_volts
397
398         if not ion_velocities[xindex[ion_number]] then
399             print(xindex[ion_number])
400             ion_velocities[xindex[ion_number]] = {
401                 ["velocity2"] = {},
402                 ["vel_x"] = {},
403                 ["vel_y"] = {},
404                 ["vel_z"] = {}
405             }
406         end
407         ion_velocities[xindex[ion_number]].velocity2[ion_number] =
408             ion_vx_mm^2 + ion_vy_mm^2 + ion_vz_mm^2
409         ion_velocities[xindex[ion_number]].vel_x[ion_number] =
410             math.abs(ion_vx_mm)
411         ion_velocities[xindex[ion_number]].vel_y[ion_number] =
412             math.abs(ion_vy_mm)

```

```

413         ion_velocities[xindex[ion_number]].vel_z[ion_number] =
414             math.abs(ion_vz_mm)
415         xindex[ion_number] = xindex[ion_number] + 1
416         xcurrent[ion_number] = xcurrent[ion_number] + xstep
417     end
418 end
419 -- For first leading ion:
420 -- * Leading ion is kept at optical axis (y=0 and z=0) as beam repulsion
421 -- needs to calculate time steps
422 -- * Forced splat after 566mm so that terminate segment is ran for
423 -- ion_number 1
424
425 if ion_number == 1 then
426     ion_py_mm = 0
427     ion_pz_mm = 0
428     ion_vy_mm = 0
429     ion_vz_mm = 0
430     if ion_px_mm > _Leading_Ion_Splat_Pos_mm then
431         ion_splat = -1
432     end
433 end
434
435 if is_QMS_enabled then
436     if ion_time_of_flight >= next_pe_update then
437         next_pe_update = ion_time_of_flight + pe_update_each_usec
438         sim_update_pe_surface = 1 -- Request a PE surface display update.
439     end
440 end
441
442 -- Force ions to splat at force_all_ions_splat_at_x_mm
443 if ion_px_mm > force_all_ions_splat_at_x_mm then
444     ion_splat = -1
445     ions_forced_to_splat[#ions_forced_to_splat + 1] = ion_number
446 end
447 -- Force ions to splat if traveling to negative x-direction
448 -- if ion_vx_mm < 0 then
449 --     ion_splat = -1
450 -- end
451
452 if (ion_px_mm > 130) then
453     return
454 end
455
456 if not collisions_for_leading_ion and (ion_number == 1) then
457     return
458 end
459
460 -- Adjust pressure
461 _pressure_pa = pressure(ion_px_mm,
462                        ion_py_mm,
463                        ion_pz_mm,
464                        current_test_variable_1_value/100)--const_pressure/100)
465
466 -- Adjust velocity
467 local vx_bar_gas_mmusec, vy_bar_gas_mmusec, vz_bar_gas_mmusec =
468     gas_velocity(ion_px_mm, ion_py_mm, ion_pz_mm, 1)
469 -- Adjust temperature
470 .temperature.k = temperature(ion_px_mm, ion_py_mm, ion_pz_mm)
471
472 -- Temporarily translate ion velocity (mm/us) frame of
473 -- reference such that mean background gas velocity is zero.
474 local vx = ion_vx_mm - vx_bar_gas_mmusec
475 local vy = ion_vy_mm - vy_bar_gas_mmusec
476 local vz = ion_vz_mm - vz_bar_gas_mmusec
477
478 local speed_ion = sqrt(vx^2 + vy^2 + vz^2)
479 -- prevent div-by-zero
480 if speed_ion < 1E-6 then
481     speed_ion = 1E-6
482 end
483
484 -- Compute mean-free-path.
485 if _mean_free_path_mm > 0 then -- explicitly specified
486     effective_mean_free_path_mm = _mean_free_path_mm
487 else -- calculate from current ion velocity
488     -- Only recompute mean-free-path if speed_ion has
489     -- changed significantly. This is intended to speed up the
490     -- calculation a bit. This code will handle flying ions by groups.
491     if last_ion_number ~= ion_number or
492        abs(speed_ion / last_speed_ion - 1) > 0.05 -- changed
493     then
494         -- Compute mean gas speed (mm/us)
495         local c_bar_gas =

```

```

497         sqrt(8*k*_temperature_k/pi/(_gas_mass_amu * kg_amu)) / 1000
498
499     -- Compute median gas speed (mm/us)
500     local c_star_gas =
501         sqrt(2*k*_temperature_k/(_gas_mass_amu * kg_amu)) / 1000
502
503     -- Compute mean relative speed (mm/us) between gas and ion.
504     local s = speed_ion / c_star_gas
505     local c_bar_rel =
506         c_bar_gas * ((s + 1/(2*s)) * 0.5 * sqrt(pi) * erf(s) +
507                     0.5 * exp(-s*s))
508     -- Compute mean-free-path (mm)
509     effective_mean_free_path_mm =
510         1000 * k * _temperature_k *
511         (speed_ion / c_bar_rel) / (_pressure_pa * _sigma.m2)
512
513     -- Store data about this calculation.
514     last_speed_ion = speed_ion
515     last_ion_number = ion_number
516
517     end
518 end
519
520 if (ion_px_mm > _disable_collisions_at) then
521     return
522 end
523 -- Limit time-step size to a fraction of the MFP.
524 max_timestep = effective_mean_free_path_mm / speed_ion / _steps_per_MFP
525
526 -- Compute probability of no collision with current time-step and speed.
527 local no_collision_prob =
528     exp(- speed_ion * ion_time_step / effective_mean_free_path_mm)
529
530 -- Test for collision.
531 if rand() < no_collision_prob then
532     return -- no collision
533 end
534 --- Collision happened
535
536 -- Compute standard deviation of background gas velocity in
537 -- one dimension (mm/us).
538 -- > From kinetic gas theory (Maxwell-Boltzmann), velocity in
539 -- one dimension is normally distributed with standard
540 -- deviation sqrt(kT/m).
541 local vr_stdev_gas =
542     sqrt(k * _temperature_k / (_gas_mass_amu * kg_amu)) / 1000
543
544 local vx_gas, vy_gas, vz_gas -- computed velocities
545 local scale = speed_ion + vr_stdev_gas * 1.732 * 3 -- sqrt(3)=~1.732
546 repeat
547     vx_gas = gaussian_random() * vr_stdev_gas
548     vy_gas = gaussian_random() * vr_stdev_gas
549     vz_gas = gaussian_random() * vr_stdev_gas
550     local len = sqrt((vx_gas - vx)^2 + (vy_gas - vy)^2 + (vz_gas - vz)^2)
551     -- assert(len <= scale) -- true at least 99% of the time.
552 until rand() < len / scale
553
554 -- Translate velocity reference frame so that colliding
555 -- background gas particle is stationary.
556 -- > This simplifies the subsequent analysis.
557 vx = vx - vx_gas
558 vy = vy - vy_gas
559 vz = vz - vz_gas
560
561
562 local impact_offset = sqrt(0.99999999 * rand())
563
564
565 local impact_angle = asin(impact_offset)
566
567 -- In other words, the effect of the above is that impact_angle has
568 -- a distribution of p(impact_angle) = sin(2 * impact_angle).
569
570 -- Compute randomized angle [0, 2*pi] for rotation of collision
571 -- plane around radial axis. This is the angle around the
572 -- center of the dart board.
573 -- Note: all angles are equally likely to hit.
574 -- The effect is that impact_theta has a distribution
575 -- of p(impact_theta) = 1/(2*pi).
576 local impact_theta = 2*pi*rand()
577
578 -- Compute polar coordinates in current velocity reference frame.
579 local speed_ion_r, az_ion_r, el_ion_r = rect3d_to_polar3d(vx, vy, vz)
580

```

```

581 -- Compute ion velocity components (mm/us).
582 local vr_ion = speed_ion_r * cos(impact_angle) -- radial velocity
583 local vt_ion = speed_ion_r * sin(impact_angle) -- normal velocity
584
585 -- Attenuate ion velocity due to elastic collision.
586 -- This is the standard equation for a one-dimensional
587 -- elastic collision, assuming the other particle is initially at rest
588 -- (in the current reference frame).
589 -- Note that the force acts only in the radial direction, which is
590 -- normal to the surfaces at the point of contact.
591 local vr_ion2 = (vr_ion * (ion_mass - _gas_mass_amu))
592 / (ion_mass + _gas_mass_amu)
593
594 -- Rotate velocity reference frame so that original ion velocity
595 -- vector is on the +y axis.
596 -- Note: The angle of the new velocity vector with respect to the
597 -- +y axis then represents the deflection angle.
598 vx, vy, vz = elevation_rotate(90 - deg(impact_angle), vr_ion2, vt_ion, 0)
599
600 -- Rotate velocity reference frame around +y axis.
601 -- This rotates the deflection angle and in effect selects the
602 -- randomized impact_theta.
603 vx, vy, vz = azimuth_rotate(deg(impact_theta), vx, vy, vz)
604
605 -- Rotate velocity reference frame back to the original.
606 -- For the incident ion velocity, this would have the effect
607 -- of restoring it.
608 vx, vy, vz = elevation_rotate(-90 + el_ion_r, vx, vy, vz)
609 vx, vy, vz = azimuth_rotate(az_ion_r, vx, vy, vz)
610
611 -- Translate velocity reference frame back to original.
612 -- This undoes the prior two translations that make velocity
613 -- relative to the colliding gas particle.
614 vx = vx + vx_gas + vx_bar_gas.mmusec
615 vy = vy + vy_gas + vy_bar_gas.mmusec
616 vz = vz + vz_gas + vz_bar_gas.mmusec
617
618 -- Set new velocity vector of deflected ion.
619 ion_vx.mm, ion_vy.mm, ion_vz.mm = vx, vy, vz
620
621 -- Now lets compute some statistics...
622
623 -- Compute running average of KE. This is for statistical reporting only.
624 -- At thermal equilibrium, KE of the ion and KE of the gas would
625 -- be approximately equal according to theory.
626 if _trace_level >= 1 then
627 -- Compute new ion speed and KE.
628 local speed_ion2 = sqrt(ion_vx.mm^2 + ion_vy.mm^2 + ion_vz.mm^2)
629 local ke2_ion = speed_to_ke(speed_ion2, ion_mass)
630
631 -- To average ion KE somewhat reliably, we do a running (exponential
632 -- decay)
633 -- average of ion KE over time. The reset time of the exponential
634 -- decay
635 -- is set to some fraction of the total time-of-flight, so the average
636 -- will become more steady as the run progresses (we assume this is a
637 -- system that approaches equilibrium).
638 -- Note: exp(-x) can be approximated with 1-x for small x.
639
640 -- time between most recent collisions
641 local dt = ion_time_of_flight - (last_collision_times[ion_number] or 0)
642 -- average over some fraction of TOF
643 reset_time = ion_time_of_flight * 0.5
644 -- weight for averaging.
645 local w = 1 - (dt / reset_time) -- ~= exp(-dt / reset_time)
646 -- update average ion KE
647 ke_averages[ion_number] = w * (ke_averages[ion_number] or ke2_ion)
648 + (1-w) * ke2_ion
649 last_collision_times[ion_number] = ion_time_of_flight
650 end
651
652 if collisions_marked == true then
653 mark() -- draw dot at collision point
654 end
655 end
656
657 function segment.terminate()
658 -- Run the chunk below only once as fly ends
659 if ion_number ~= 1 then
660 return
661 end
662 print("Terminate Segment Begun:")
663 print("Potential :", current_test_variable_1_value, "/", test_variable_1_end,
664 " simulated!")

```



```

665 local sim1_data = current_test_variable_1_value
666 local sim2_data = current_test_variable_2_value
667
668 -- Change potentials for next run.
669 potentials1[sim_i] = current_test_variable_1_value
670 current_test_variable_1_value = current_test_variable_1_value + test_variable_1_step
671 sim_rerun_flym = 1 --Rerun simulation as default
672
673 --Count passed ions for each plane
674 for i,v in ipairs(plane_data) do
675     local sum = 0
676     for j=1,ions_flied do
677         if v.is_passed[j] then
678             sum = sum + 1
679         end
680     end
681     flys_ions_in_plane[i].count[sim_i] = sum
682 end
683
684 local xpositions_mean = {}
685 local xpentials_mean = {}
686 local ion_velocities_mean = {}
687 local ion_velocities_std = {}
688 local ion_vel_x_mean = {}
689 local ion_vel_y_mean = {}
690 local ion_vel_z_mean = {}
691 local ion_vel_x_std = {}
692 local ion_vel_y_std = {}
693 local ion_vel_z_std = {}
694 local ion_count = {}
695
696 print("#ion_velocities: ", #ion_velocities, " ", ion_velocities[1].velocity2[1])
697 for i,v in ipairs(ion_velocities) do
698     xpositions_mean[i] = xpositions_sum[i]/vx_ion_count[i]
699     print("pos:", xpositions_mean[i], " skipped", times_skipped[i])
700     xpentials_mean[i] = xpentials_sum[i]/vx_ion_count[i]
701
702     ion_count[i] = 0
703
704     local v2_sum = 0
705     for j,s in ipairs(ions_forced_to_splat) do
706         if not v.velocity2[s] then
707             break
708         end
709         ion_count[i] = ion_count[i] + 1
710         v2_sum = v2_sum + v.velocity2[s]
711     end
712
713     ion_velocities_mean[i] = v2_sum/(#ions_forced_to_splat-times_skipped[i])
714     local v2_std_sum = 0
715     for j,s in ipairs(ions_forced_to_splat) do
716         if not v.velocity2[s] then
717             break
718         end
719         v2_std_sum = v2_std_sum + (v.velocity2[s]-ion_velocities_mean[i])^2
720     end
721     ion_velocities_std[i] = (v2_std_sum/(#ions_forced_to_splat-times_skipped[i]))^0.5
722
723     local v_sum = 0
724     for j,s in ipairs(ions_forced_to_splat) do
725         if not v.velocity2[s] then
726             break
727         end
728         v_sum = v_sum + v.vel_x[s]^2
729     end
730     ion_vel_x_mean[i] = v_sum/(#ions_forced_to_splat-times_skipped[i])
731     local v_std_sum = 0
732     for j,s in ipairs(ions_forced_to_splat) do
733         if not v.velocity2[s] then
734             break
735         end
736         v_std_sum = v_std_sum + (v.vel_x[s]^2-ion_vel_x_mean[i])^2
737     end
738     ion_vel_x_std[i] = (v_std_sum/(#ions_forced_to_splat-times_skipped[i]))^0.5
739
740     local v_sum = 0
741     for j,s in ipairs(ions_forced_to_splat) do
742         if not v.velocity2[s] then
743             break
744         end
745         v_sum = v_sum + v.vel_y[s]^2
746     end
747     ion_vel_y_mean[i] = v_sum/(#ions_forced_to_splat-times_skipped[i])
748     local v_std_sum = 0

```

```

749     for j,s in ipairs(ions_forced_to_splat) do
750         if not v.velocity2[s] then
751             break
752         end
753         v_std_sum = v_std_sum + (v.vel_y[s]^2-ion_vel_y_mean[i])^2
754     end
755     ion_vel_y_std[i] = (v_std_sum/(#ions_forced_to_splat-times_skipped[i]))^0.5
756
757     local v_sum = 0
758     for j,s in ipairs(ions_forced_to_splat) do
759         if not v.velocity2[s] then
760             break
761         end
762         v_sum = v_sum + v.vel_z[s]^2
763     end
764     ion_vel_z_mean[i] = v_sum/(#ions_forced_to_splat-times_skipped[i])
765     local v_std_sum = 0
766     for j,s in ipairs(ions_forced_to_splat) do
767         if not v.velocity2[s] then
768             break
769         end
770         v_std_sum = v_std_sum + (v.vel_z[s]^2-ion_vel_z_mean[i])^2
771     end
772     ion_vel_z_std[i] = (v_std_sum/(#ions_forced_to_splat-times_skipped[i]))^0.5
773
774
775 end
776 print("splat ions", #ions_forced_to_splat)
777 local fout
778 if v.is_previously_opened then
779     fout = io.open("velocities_data.out", "a")
780 else
781     fout = io.open("velocities_data.out", "w")
782     v.is_previously_opened = true
783 end
784 for i,v in ipairs(ion_velocities_mean) do
785     fout:write(sim2_data, " ", sim1_data, " ", ion_count[i], " ",
786               xpositions_mean[i], " ", v, " ", ion_velocities_std[i], " ",
787               ion_vel_x_mean[i], " ", ion_vel_x_std[i], " ",
788               ion_vel_y_mean[i], " ", ion_vel_y_std[i], " ",
789               ion_vel_z_mean[i], " ", ion_vel_z_std[i], " ",
790               xpotentials_mean[i], " ", times_skipped[i], "\n")
791 end
792 fout:close()
793
794
795 -- Save each recorded plane data (done for each fly)
796 -- one file for one plane
797 -- The first time the file is created and following times data is
798 -- appended to the file
799 for i,v in ipairs(plane_data) do
800     local fout
801     if v.is_previously_opened then
802         fout = io.open("plane_data." .. v.plane_pos .. "nm.out", "a")
803     else
804         fout = io.open("plane_data." .. v.plane_pos .. "nm.out", "w")
805         v.is_previously_opened = true
806     end
807     for j=1,ions_flied do
808         if v.is_passed[j] then
809             fout:write(sim2_data, " ",
810                       sim1_data, " ",
811                       j, " ",
812                       v.tof[j], " ",
813                       v.x_pos[j], " ",
814                       v.y_pos[j], " ",
815                       v.z_pos[j], " ",
816                       v.x_vel[j], " ",
817                       v.y_vel[j], " ",
818                       v.z_vel[j], " ",
819                       v.potential[j], " ",
820                       "\n")
821         end
822     end
823     fout:close()
824 end
825
826
827 -- Stop after current potential rises above end potential
828 if current_test_variable_1.value > test_variable_1_end then
829     -- Save data to file
830     local fout
831     if m.is_previously_opened then
832         fout = io.open("main_data.out", "a")

```

```

833     else
834         fout = io.open("main_data.out", "w")
835         m.is_previously_opened = true
836     end
837
838     print ("potential2 was ", current_test_variable_2_value)
839     local i = 1
840     while i <= sim_i do
841         fout:write(current_test_variable_2_value, " ", potentials1[i], " ")
842         for j,v in ipairs(flys_ions_in_plane) do
843             fout:write(v.count[i], " ")
844         end
845         fout:write("\n")
846         i = i+1
847     end
848     fout:close()
849     current_test_variable_1_value = test_variable_1_start
850     if current_test_variable_2_value >= test_variable_2_end then
851         sim_rerun_flym = 0 --No rerun
852     else
853         sim_i = 0
854         current_test_variable_2_value = current_test_variable_2_value + test_variable_2_step
855     end
856 end
857 end
858 end

```